PROTOTYPE DEVELOPMENT AND DYNAMIC CHARACTERIZATION OF DEPLOYABLE CUBESAT BOOMS

THESIS

Grant M. Thomas, 2nd Lt, USAF

AFIT/GA/ENY/10-M10

**DEPARTMENT OF THE AIR FORCE
AIR UNIVERSITY**

AIR FORCE INSTITUTE OF TECHNOLOGY

Wright-Patterson Air Force Base, Ohio

APPROVED FOR PUBLIC RELEASE; DISTRIBUTION UNLIMITED

AFIT/GA/ENY/10-M10

PROTOTYPE DEVELOPMENT AND DYNAMIC CHARACTERIZATION OF DEPLOYABLE CUBESAT BOOMS

THESIS

Presented to the Faculty

Department of Aeronautics and Astronautics

Graduate School of Engineering and Management

Air Force Institute of Technology

Air University

Air Education and Training Command

In Partial Fulfillment of the Requirements for the

Degree of Master of Science in Astronautical Engineering

Grant M. Thomas, BS

2nd Lt, USAF

March 2010

AFIT/GA/ENY/10-M10

PROTOTYPE DEVELOPMENT AND DYNAMIC CHARACTERIZATION OF DEPLOYABLE CUBESAT BOOMS

Grant M. Thomas, BS

2nd Lt, USAF

Approved:

_____   _____
Jonathan T. Black, PhD, (Chairman)   Date

_____   _____
Richard G. Cobb, PhD, (Member)   Date

_____   _____
Eric D. Swenson, Lt Col, USAF (Member)   Date

Abstract

The current barrier to CubeSat proliferation is their lack of utility depth. These small satellites are exceptionally well suited for specific space missions such as space weather observation and other scientific data gathering exploits; however, they are not suited for every mission. The 10cm-cube form factor that gives the CubeSat its unique advantage is also its greatest hindrance. A potential bridge over this gap is the successful integration of deployable booms onto the CubeSat structure. With this research, the Air Force Institute of Technology (AFIT) explored the parameters of deployable tapespring booms using the triangular retractable and collapsible (TRAC) cross- sectional geometry developed by Air Force Research Labs (AFRL) and used on NASA's CubeSat, Nanosail-D. These booms were augmented with reflective membranes and specifically designed to deploy on orbit for the purpose of ground observation; observations that could later be used to determine the deployed dynamics of the booms from optical data gained passively by solar illumination.

Initially, the boom behavior at multiple frequency excitations was characterized so as to develop an accurate finite element model where further predictions could be determined without the costly attempt to simulate the often irreproducible environment of space. Nine total modal frequencies were detected and modeled below 25 Hz, which was to be expected as the gossamer-like structure of the beams is particularly susceptible to low-frequency excitations. In addition to stationary testing, deployment concept testing was also conducted to determine the viability of a novel boom and membrane deployment scheme developed in house. In concurrence with the finite element model, this data provides the foundation for the future development of deployable appendages onto the CubeSat platform here at AFIT.

Acknowledgments

My family has borne the brunt of my extra time away from home and I am especially grateful for their patience. My thesis advisors Dr. Black, Dr. Cobb, and Lt Col Swenson, have all provided valuable leadership, without which, I would not have completed this project. Jeremy Banik at Kirtland AFRL has been a frequent consultant and technical advisor on all things boom related. Daniel Ryan and Brain Crabtree at the AFIT Machine Shop did a fantastic job fabricating the individual satellite components. Jay Anderson, Sean Miller, Chris Zickefoose, John Hixenbaugh, Barry Page and Wilbur Lacy all supported in the bringing of this research to fruition. Additionally, my fellow classmates 2d Lt Steve Miller and 2d Lt Mike Trottier were both wellsprings of insight in times of desperate need. Thank you.

Grant M. Thomas

Table of Contents

List of Figures

xiv

List of Tables

PROTOTYPE DEVELOPMENT AND DYNAMIC CHARACTERIZATION OF DEPLOYABLE CUBESAT BOOMS

I. Introduction

1.1 Background

Advancement in spacecraft design has increased exponentially from its inception in the 1960's. Today's spacecraft are far more capable than those pioneering spacecraft of yesteryear, consolidating multiple missions into a single space platform. This evolving mission accommodation however, is not without a price. Current satellites are ever increasing in complexity, design times, and, perhaps most significantly, cost. Consequently, fewer satellite programs are going forward and those that do utilize dated technology due to the time lapse between technological development and on-orbit capability. Doing more with less is always desirable in satellite design. The "Smaller, Cheaper, Faster, Better" movement of the late nineties remodeled satellite design. The prevailing design strategy of that decade accomplished objectives in a similar manner but on a smaller scale to achieve the desired lower cost. While this methodology produced satellites at a lower monetary cost, the net result was not necessarily better; as evidenced by several of NASA's deep space mission failures. The prolonged development time, high cost, and questionable resilience of some of our modern space assets has cast doubt on the now-conventional satellite design rubric, evoking a new satellite design paradigm: small satellite design. Small satellites are generally single-purposed and inexpensive, providing merely "sufficient" capability. Rather than creating one large, complex, expensive satellite to handle every mission and possible contingency, small satellites

1

offer specificity to the user and increased mission flexibility; reducing costs and drastically abbreviating time from design to development provided in part by the emerging picosatellite technology (Heidt, Puig-Suari, Moore, Nakasuka, & Twiggs, August 2001). Picosatellites, and specifically CubeSats, are not merely a scaling of larger satellite design and capability, but a complete renovation of current satellite convention. If implemented on a large scale, the resulting picosatellite system would be quick and inexpensive to build while providing a robust space platform to launch the successful space missions of the future.

CubeSats are a subset within the greater body of small satellite designs; functioning as both the epitome of small satellite replicability and design functionality. In 1999, California Polytechnic State University along with Stanford University collaborated to develop the CubeSat: a one liter volume, one kilogram picosatellite utilizing commercial off-the-shelf electronics(Whorton, Heaton, Pinson, Laue, & Adams, 2008). Each CubeSat is developed to be fit directly into the Poly Picosat Orbital Deployer, or P-POD platform. This standard deployer ensures all CubeSat developers conform to a common form factor which reduces cost and development time. Thus creating small spacecraft that are both inexpensive to construct and launch. Today, between 10 and 20 University-Class CubeSats are launched successfully every year by universities as shown in Figure 1, creating a significant excitement among enthusiasts as to the usefulness of such a spacecraft platform beyond walls of academia.
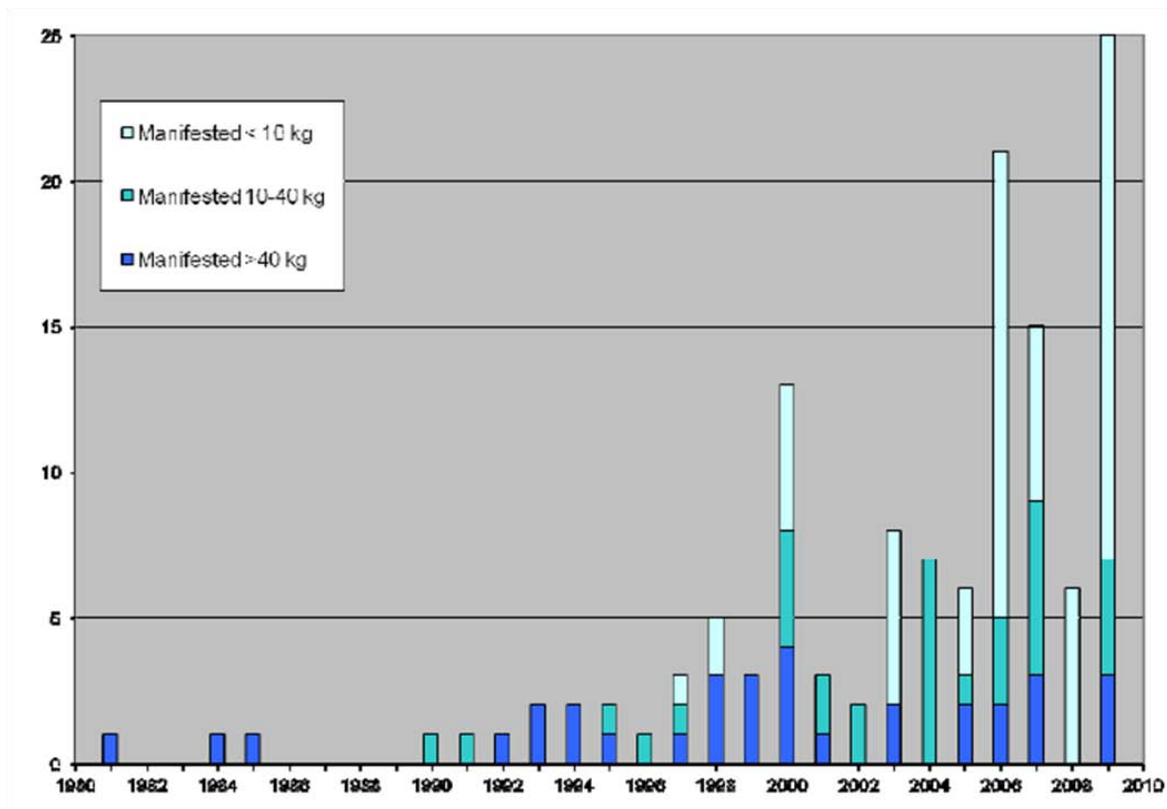
Figure 1. Current Trends in University-Class Satellites (Swartout, 2009)

The increased number of satellites in Figure 1 with manifested weights below 10

kg is representative of the current satellite trend towards smaller and lighter satellites

among universities; which is, not surprisingly, indicative of the present trends in industry

as well. One recent CubeSat designed by NASA, was Nanosail-D depicted in Figure 2,

designed to deploy a 9.3 m^2 sail from a 10 cm x 10 cm x 30 cm CubeSat. NASA had

hoped to demonstrate the feasibility of solar sailing and was able to successfully test the

sail's deployment and performance in the laboratory; but unfortunately, the satellite was

lost due to a launch vehicle failure (Whorton, Heaton, Pinson, Laue, & Adams, 2008).

3
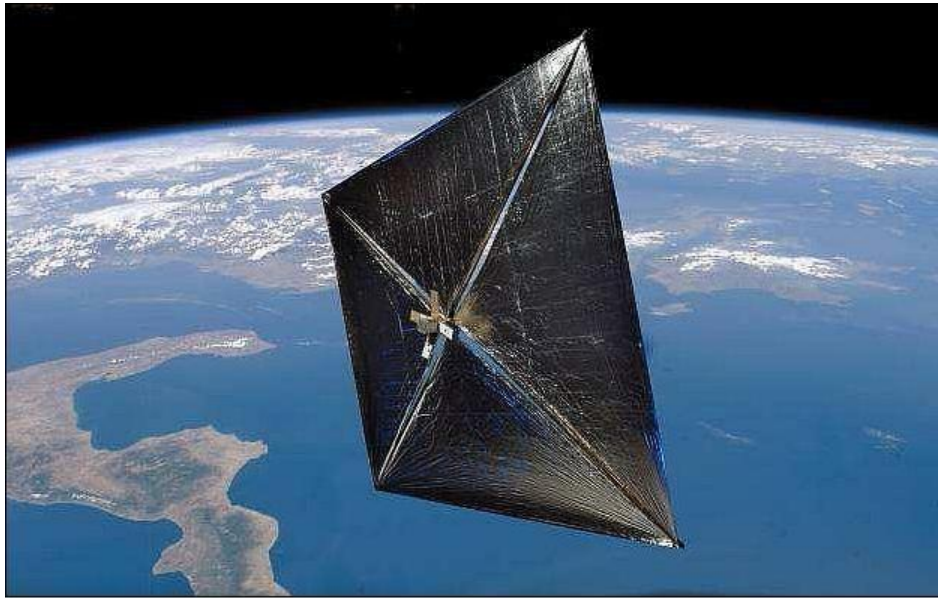
Figure 2. NASA's NanoSail-D in On-Orbit Deployed Configuration (Whorton, Heaton, Pinson, Laue, & Adams, 2008)

However, current development is now underway for another solar sail satellite, Lightsail-1, slated to launch late in 2010 (Friedman, 2009). The Planetary Society plans to launch three solar sailing spacecraft all based on the 3U- CubeSat platform. Lightsail-1 will possess four triangular sails mounted on 4m beams; giving a total reflective surface area of 32 square meters. The solar sails and beams will be entirely contained within 2U's of the CubeSat chassis. The rest of the CubeSat will be dedicated to the electronics bus and control module. The goal of the Lightsail-1 mission is a proof of concept mission to verify the hypothesis of sunlight as a means of propulsion. The second and third Lightsail missions will be similar to the first with the exception of larger sails and increased instrumentation and control. The Planetary Society is primarily interested in deep space exploration which, while profoundly fascinating, holds little promise for immediate military application. However, should light propulsion prove possible, an

4

application of eminent military relevance is that of space weather observation. With controllable sails, any point in space could become a possible Lagrangian point; balancing the spacecraft between the constant force of gravity and the constant force of photons impinging on the reflective Mylar surface of the craft. This could, in effect, provide a much more robust early warning system and allow us to place satellites closer to the sun than previously possible.

While small satellites proffer an especially promising venture in concept, the current limiting factor in small satellite design appears to be satellite operational capability; namely, what can these satellites really do? The decrease in electronic component size and weight, advancement in battery design, and vastly improved computer memory capability have all paved the way for satellites that are orders of magnitude smaller than previous generation's with ever increasing capability and very low power consumption. The decrease in satellite size directly contributes to both a lower mission and launch costs. In light of recent technological developments the necessities and benefits of large satellite designs must now be called into question. If small satellites can demonstrate some tangible large scale utility and we are found to be within the straits of sufficient necessity, then it is possible to conclude that we are indeed on the cusp of the next big development in space technology. Presently, CubeSats are perhaps the most cost effective independent means of delivering a payload into orbit; a wellspring of technological efficiency that remains largely untapped.

1.2 Research Objectives

The objective of this research is to design and test a lightweight structure that will be deployed from a passive CubeSat and be observed from the ground using a portable telescope. The research focus will be on the design and deployment of the reflectors deployed from the CubeSat and their subsequent testing. The proposed satellite design, termed SLiMSat (Slender Lenticular Integrated Mast Satellite), can be seen in Figure 3.
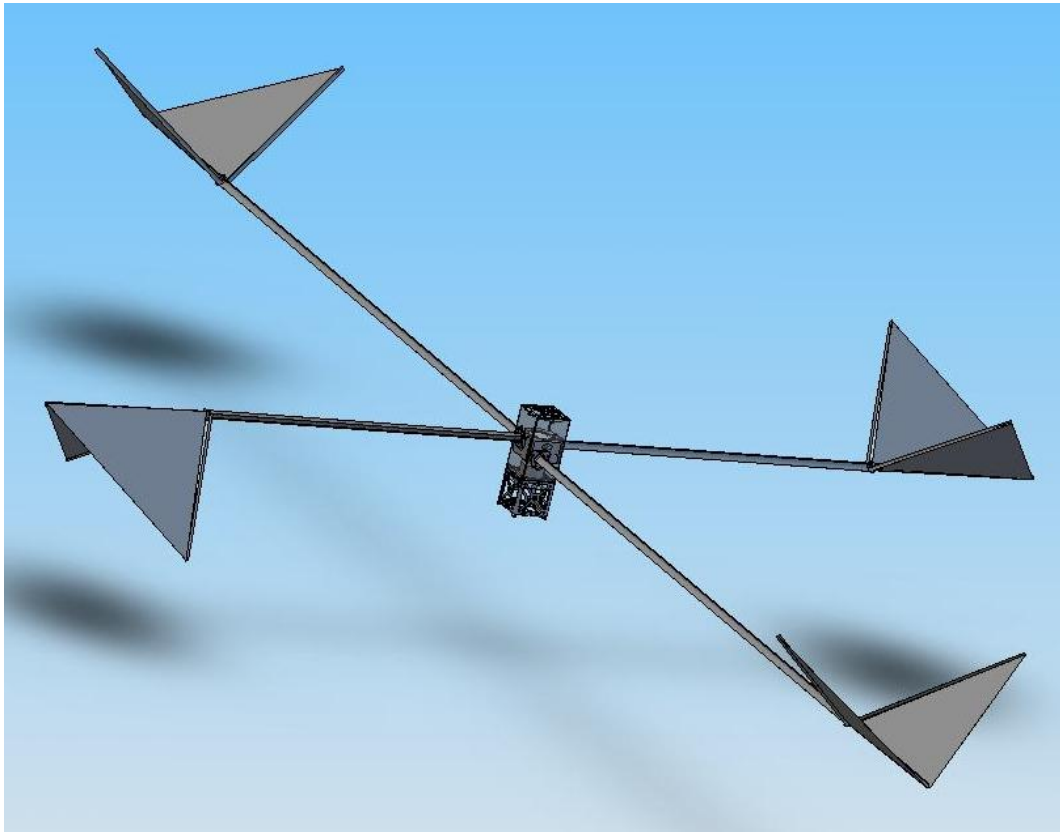
Figure 3. SLiMSat Design Concept

SLiMSat will utilize four deployable tapespring booms of similar design to Nanosail-D, as they have been well characterized and proven effective. However, SLiMSat will differ from Nanosail-D in that the sail material will be replaced with

reflectors mounted on the ends of each boom. Notably, the presence of large reflective masses at the end of each thin deployable boom will not only virtually guarantee the presence of highly non-linear in-flight dynamics; but also provide an excellent platform for the on-ground observation and verification of the predicted satellite behavior. From the specifications of a typical telescope potentially used to detect and track SLiMSat, the reflectors are required to be as large as possible at a baseline separation distance of at least one meter from one another.

To accurately predict the satellite behavior in both pre- and post-deployment configurations will require extensive knowledge of the satellite behavior on ground in a closely simulated space environment. The ultimate measure of our mission success will not only be the development of a CubeSat possessing deployable structures with ground-based observability but whether the observed satellite behavior actually matches that of our predictions. That knowledge will be a direct reflection of both the foresight and faculty of our specified testing rubric.

We want our satellite to be seen, and our best designs will do just that. In order to determine the satellite attitude from a ground-based telescope, our on orbit deployed configuration needs to resolve into a multiple pixel image. Only a multiple pixel image will allow us to determine from the ground the structural dynamics of the reflector surfaces and allow us to accurately predict the behavior of the booms. Two distinct baseline and correlated boom lengths will permit the basic identification of satellite orientation and provide two distinct dynamic boom behaviors as related to their length.

The design process involving the selection and fabrication of one of four preliminary reflector design concepts discussed in detail the companion paper. This paper will focus primarily on the testing and quantitative differentiation of the reflectors themselves.

Our final reflector design should function reliably and meet our needed specifications. However objectifying the subjective notional concepts of design is no trivial matter. With that in mind, our developed testing paradigm fundamentally seeks to quantify the answers of two basic questions: Is this reflector design concept viable? And, what will the deployed behavior of a given concept look like?

Concept viability testing focuses on three facets of design functionality, namely: deployment reliability, stowed spatial accommodation within the satellite, and baseline extension for observable resolution from a ground-based telescope. The analysis of this dynamic testing will attempt to resolve the potential observability and on-orbit performance of the satellite while in its deployed configuration. The summation of the dynamic and deployment tests will yield insight into which of our designs holds the most promise; providing a wealth of data and a basis for a more objective opinion.

The boom reflector geometry tests will determine whether our design is plausible as well as whether it meets the functional requirements of our mission. Our boom reflectors themselves are required to be at least one meter in diameter, and provide a baseline of at least four meters to be seen in multiple pixels thereby allowing attitude determination from the ground. We anticipate certain design concepts to have a higher

packagability ratio, an inherently favorable design characteristic. It would seem the most appropriate method of testing these particular characteristics is modeling and direct prototype manufacture. Through our models we will be able to observe the structural dynamics of the satellite and produce initial estimations which will be either confirmed or discarded based on the actual physical evidence of the prototype behavior.

Additionally, we must also consider not merely whether the boom reflector can meet the desired design specifications, but also, to what degree. The reliability of the boom and reflector deployment will be tested via repeated tests whereupon both the reliability and repeatability of the boom reflectors will be scrutinized. The latter will focus on both boom and reflector degradation after each subsequent deployment; giving quantitative value to the overall robustness of the specified boom reflector design. Gravity off-load testing will also be necessary to predict the behavior of the boom reflectors in orbit. Most likely, this will involve hanging the boom reflector vertically and performing vibrational tests with the gravitational force vector aligned coaxially with that of the boom so as to minimize its effect.

The results of all the aforementioned tests will be compiled into a design matrix to facilitate concept performance parameterization and comparison. These tests, while rather basic in concept and execution, will provide invaluable information about the satellite performance and particular design concept favorability.

As has already been mentioned, the focus of the research is on the development and manufacture of deployable reflectors attached to the ends of the booms themselves.

CubeSats in their current form, while of eminent and obvious value within the walls of academia, are of limited potential use without the successive advent and development of deployable appendages. The booms, such as those used on Nanosail-D and our satellite, are clearly the harbingers in the new ensuing wave of CubeSat utility. Later, we anticipate these reflectors could be readily adapted to more active uses such as that of deployable dishes, antennas, or even solar sails. Additionally, an antenna made to fit along the deployable boom structure itself opens an additional venue for CubeSats to supplant traditional space architecture; accomplishing still more with less.

While small satellite design development is widely regarded as the future of space technology, their advance is not merely as simple as scaling or stripping down current satellite developments. Successful large scale CubeSat satellite development hinges on the resolution of several non-trivial issues, one of which is the structural functionality and development of boom technologies for small satellite use. Research will hopefully cast some light into this arena paving the way towards fully realized CubeSat utility.

1.3 Research Focus

In order to develop a functioning CubeSat with deployable booms at AFIT, the research and development workload was divided into two primary focus areas. The systems engineering design will be covered in a companion thesis(Swenson, 2010); while this thesis will look specifically at the booms themselves and their integration into the standardized CubeSat form factor. Through the dynamic characterization of the booms,

the viability and limitations of this particular deployable technology and its subsequent

implementation should be readily apparent.

1.4 Document Preview

       This document is organized in the following manner. Chapter I serves as an

introduction wherein both the motivation and focus of the research are explored. Chapter

II provides a context for the research, giving the necessary background from which our

research can build. Chapter III presents the theoretical justification for the design and

describes the testing setup explicitly. The discussion of the testing results and design

analysis comprise the content of Chapter IV; while Chapter V concludes by summarizing

the conclusions of that analysis as well as making further recommendations for those who

are to follow.

II. Literature Review

2.1 Chapter Overview

This chapter discusses the preliminary work that preceded this research and development; serving as both a context and a foundation. The outline of the following sections includes a history of the development of CubeSats, the implementation of deployable booms into satellites in general, the development history and applications of AFRL's TRAC boom, as well as a discussion of gossamer membranes in small satellites while primarily focusing on reflective surfaces in space applications.

2.2 CubeSat Development

CubeSats, like that depicted in Figure 4, are a special sect of picosatellites distinguished by their adherence to a standardized form factor developed by California Polytechnic State University, San Luis Obispo (Cal Poly) and the Space Systems Development Laboratory (SSDL) at Stanford University in 1999 (Nugent, Munakata, Chin, Coelho, & Puig-Suari, 2008). The CubeSat concept was initially presented and proposed by Twiggs at the USSS (University Space Systems Symposium), Kauai Beach Hotel, Kauai, Hawaii, Nov. 6-8, 1999. Twiggs' initial proposal was met with considerable skepticism as inexpensive, miniature satellites we not envisioned to posses much useful potential. However, CubeSats have since demonstrated their merit to various industries and academic institutions as a valuable space asset primarily for two factors: their inexpensive cost and, as an indirect consequence, their unprecedented ability for risk. The inexpensive cost of the CubeSats opened the door of space to many

who might otherwise have been financially prohibited from participation. The low cost was facilitated by the CubeSat size and standardization.

Figure 4. CP-1 CalPoly's First CubeSat (Nugent, Munakata, Chin, Coelho, & Puig-Suari, 2008)

2.3 CubeSat Standardization

The CubeSat standard developed by CalPoly and shown in Figure 5, states that a single CubeSat should be a 10-cm cube and having a total mass of no more than 1 kg. This standard was derived from a careful consideration of factors, namely the size of available commercial off-the-shelf (COTS) components (i.e. solar cells, batteries, transceivers, etc), the P-POD's dimensions and features, the launch vehicle environmental and operational requirements and additional self-imposed safety standards (Heidt, Puig-Suari, Moore, & Twiggs, 2001).
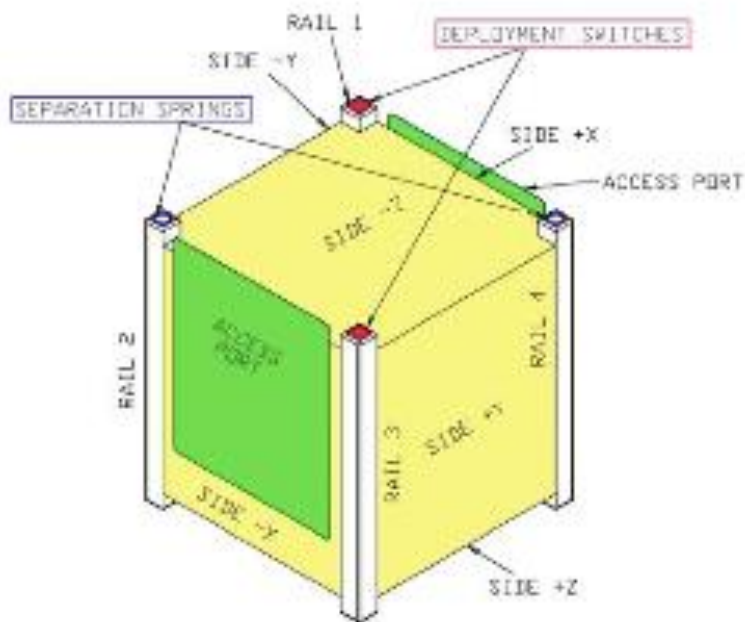
Figure 5. Schematic of the CubeSat Standard (Nugent, Munakata, Chin, Coelho, & Puig-Suari, 2008)

The primary COTS components which drove dimensional requirements for the

CubeSat Standard were the solar cells and batteries. The market offering of the day

provided a number of solar cells approximately 30 mm x 70 mm in size. It was presumed

that CubeSats should be able to body mount at least two solar cells per face to generate

enough voltage to support common microcontrollers (3 to 5 volts). Additionally, a

various assortment of cylindrical and prismatic cell batteries of various chemistries were

available in sizes that would be compatible with the standard CubeSat form factor

(Toorian, Blundell, Puig-Suari, & Twiggs, 2005)

The P-POD interface as pictured in Figure 6 and Figure 7 was also a crucial driver

in the standardization of a viable design identifying the following criteria as critical:

14

- The center of mass of a CubeSat must be within 2 cm of its geometric center to minimize tumble and spin rates during deployment from the P-POD

- The location of the access ports on the P-POD determines where CubeSats should have diagnostic ports and remove before flight (RBF) pins

- Rails on CubeSats must be smooth, flat, and hard anodized to prevent cold welding from the launch environment and minimize friction during deployment

- Thermal expansion of the CubeSats should be similar to that of the P-POD material, Aluminum 7075-T73

- CubeSat design tolerances are intrinsically correlated to P-POD tolerances and specifications

Figure 6. P-POD Mk. III(Nugent, Munakata, Chin, Coelho, & Puig-Suari, 2008)
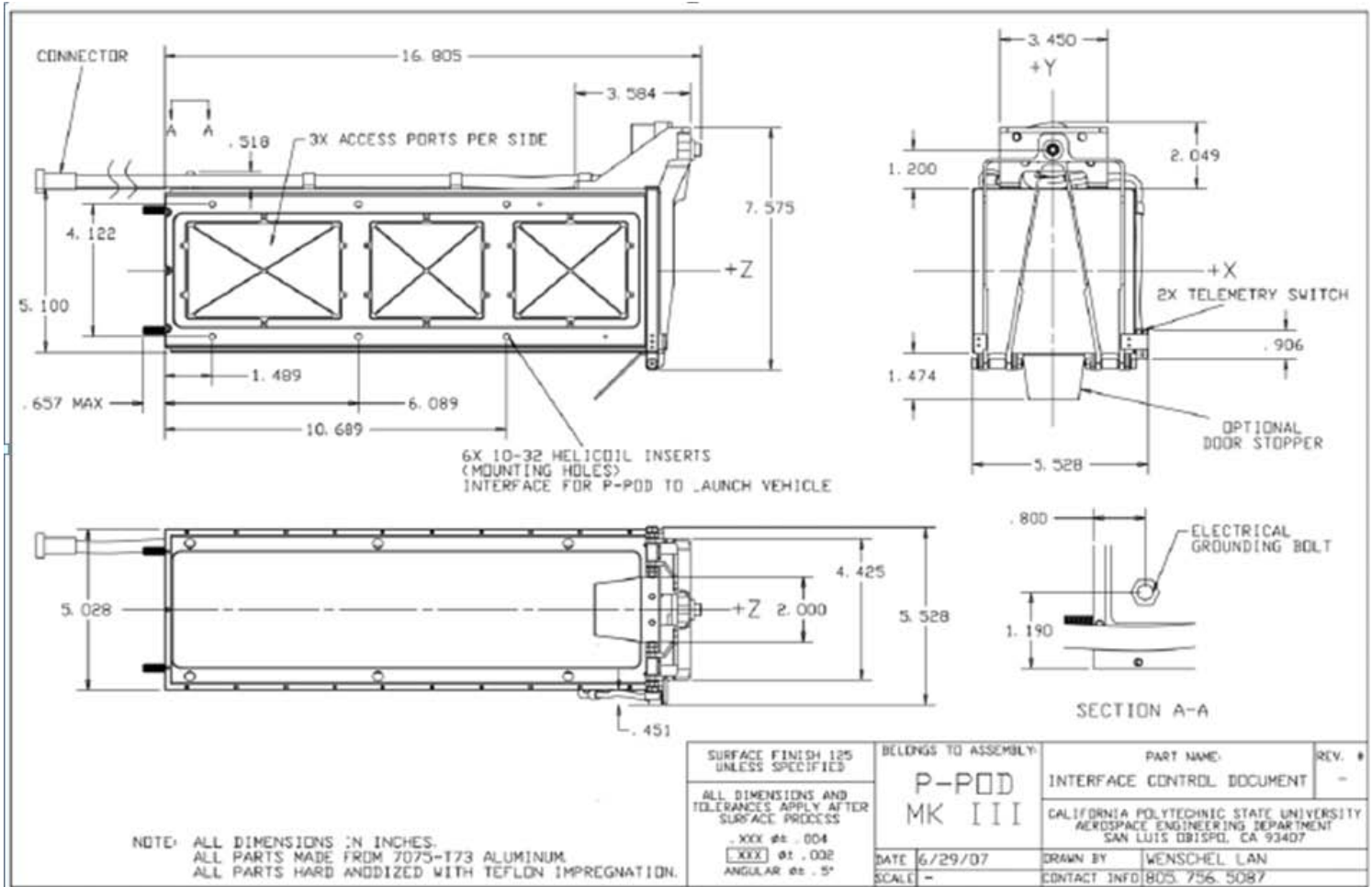
Figure 7. Poly Picosatellite Orbital Deployer Mk III ICD (Lan, 2007)

In addition to these P-POD constraints, the self-imposed constraints of the CubeSat

Design Specification (CDS) incorporated several key safety features to mitigate the risks

to other CubeSats (Nugent, Munakata, Chin, Coelho, & Puig-Suari, 2008). These include:

- An RBF pin is required to keep the CubeSats inactive during integration

- At least one deployment switch must physically disable the electronic systems
of the CubeSat when inside the integrated P-POD

16

- Separation springs to allow adequate separation between CubeSats after deployment from the P-POD

- A specified time delay between deployment and activation of any antennas, booms, or transmitters to ensure safety of other CubeSats

In light of the aforementioned criteria we can conclude that the specification of a 1 kg, 10 cm by 10 cm cube, while appearing on the surface rather arbitrary, was actually determined directly from multiple competing design considerations.

Conforming to the CubeSat standard is more difficult in some respects than designing a comparable satellite without that burden of adherence; however, the benefits far surpass the cost. A standardized CubeSat/P-POD system assures the launch providers that each satellite will meet the necessary requirements. This standardization greatly simplifies the communication path for the launch provider since they only need to be concerned with the mechanical and electrical interfaces of the P-POD to their launch vehicle. CubeSat developers need only concern themselves with conforming to the CDS specifications to fit within the P-POD. Additionally, the P-PODS themselves have been successfully integrated into multiple launch platforms often within months of launch as shown in Figure 8, Figure 9, and Figure 10.

Figure 8. P-PODs Mounted on Rockot Launch Vehicle 2003(Chin, Coelho, Brooks, Nugent, & Suari, 2008)

Figure 9. P-PODs Mounted on Dnepr Launch Vehicle, 14 CubeSats from 10 universities (Chin, Coelho, Brooks, Nugent, & Suari, 2008)
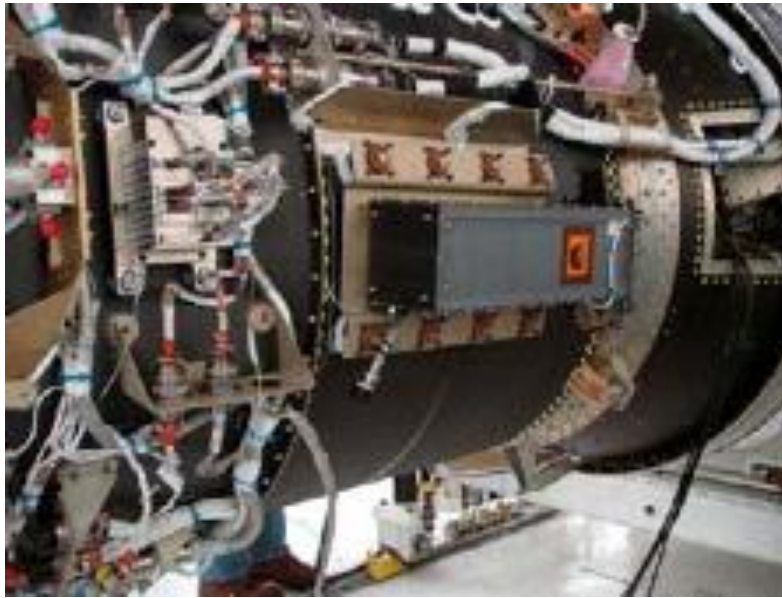
Figure 10. P-POD Mounted on Minotaur Launch Vehicle (Chin, Coelho, Brooks, Nugent, & Suari, 2008)

2.4 CubeSat Capability

Small satellites are widely heralded as the future of space technology; however, their advance is not merely as simple as scaling or stripping down current satellite developments. Successful large scale satellite development hinges on the resolution of several non-trivial issues: responsive launch, ground station availability, CONOPS of individual satellites and constellations, command/control/communications, and TPED (Tasking, Processing, Exploitation, and Dissemination). As of yet, many of these issues remain unresolved and virtually unconsidered, not the least of which is the focus of our proposed avenue of research: the structural functionality and development of boom technologies for small satellite use, specifically that of CubeSats.

The successful integration of boom technology will allow CubeSats to perform missions commonly reserved for larger, more complex space platforms. These booms will allow sensor placement and communication packages that mimic the behavior of larger satellites without the associated costs. And presumably, as modern electronic capability continues to increase according to Moore's law[1], CubeSat capability will advance from notional fantasy to pragmatic reality. However, if small satellites, however promising, cannot sufficiently accomplish a meaningful mission then their continued development resolves to be nothing more than a diffuse misappropriation of resources. Successful boom implementation stands a compelling link between the present utility of CubeSats today and the anticipated application of the CubeSats of the future (Swenson, 2010).

2.5 Notable CubeSat Missions

From 2003 to the present there have been nearly 80 different CubeSat missions (Swartout, 2009). These missions have had varying degrees of success as most are primarily funded by universities, but there have been CubeSat missions by Boeing and NASA as well. It would not be prudent or instructive to delineate each individual mission and its success or failure here; however, there are several CubeSat missions wherein the particular lessons learned are specifically applicable to the SLiMSat mission and understanding.

---

[1] **Moore's law,** named after Intel co-founder Gordon E. Moore, describes a long-term trend in the history of computing hardware, in which the number of transistors that can be placed inexpensively on an integrated circuit has doubled approximately every two years (Moore, 1965).

2.5.1 QuakeSat.   Arguably the most successful CubeSat to date has been

Stanford University's QuakeSat providing data shown in Figure 11 for the early detection

of earthquakes. In the early 1990's satellites Cosmos 1809 and Aureol-3 detected

extremely low frequency (ELF) magnetic field signals prior to and just after large

earthquakes. Consequently, a hypothesis developed that these ELF signals might be a

precursor to large earthquakes and could be used to indicate their imminence. However,

the exact parameters of these ELF signals were still largely unknown, making it difficult

to specify the exact characteristics of a larger science satellite to thoroughly test the

theory. An inexpensive CubeSat (QuakeSat) was built, launched in June 2003, and flown

to help determine the design parameters and values needed to build a research satellite for

this mission (Flagg, et al., 2004). From June 30th, 2003 to 2004 QuakeSat downloaded

over a gigabyte of data, collecting over some 1700 payload collections. Effectively

demonstrating that, while CubeSats are unlikely to function as replacements for

multimillion dollar research satellites, they clearly have some tangible utility as readily

deployable, inexpensive "guinea pigs" that perform particular missions quite well.

Our structural development of an AFIT CubeSat could also benefit from some

specific lessons learned from the retrospective analysis of the QuakeSat mission. For

instance, QuakeSat itself did not have very stringent cleanliness requirements, but the

requirements of the surrounding spacecraft necessitated a "bake-out" process to force

solvents to outgas before it was ready for launch (Bleier, et al., 2004). The facility

requirement for the right type of oven must be considered in the overall cost of the

satellite. It is also beneficial to examine the QuakeSat solar panel design which is similar

to the one we will be using on our CubeSat. The wing-type solar panels were noted to be

particularly fragile, and while providing ample power on orbit, were damaged

significantly during assembly, and testing. The lack of time and funding forced

QuakeSat to fly with damaged panels which fortunately did not significantly impact their

mission success. However, a suggested modification of the solar panel rigid backplate

might have been a "hogged out area for the array in a thicker sheet (much like the body

panels that were mounted) or simpler, a hogged out "I" beam section that the panels sat

in. This would have provided extra protection to the arrays and wires during the vibration

of launch and would have eliminated the panel bending that occurred during handling and

P-Pod prep (Bleier, et al., 2004)." The implementation of solar panels into SLiMSat

should bear this advice in mind. Additionally, the QuakeSat designers also iterated the

need for an even greater dependence on 3-D modeling programs such as SolidWorks to

ensure that the individually constructed parts would fit within the satellite; additionally,

clearance issues can be resolved for the deployable structures avoiding costly

reengineering later. Ultimately, early reference to CAD models would ensure a faster

design to prototype time.
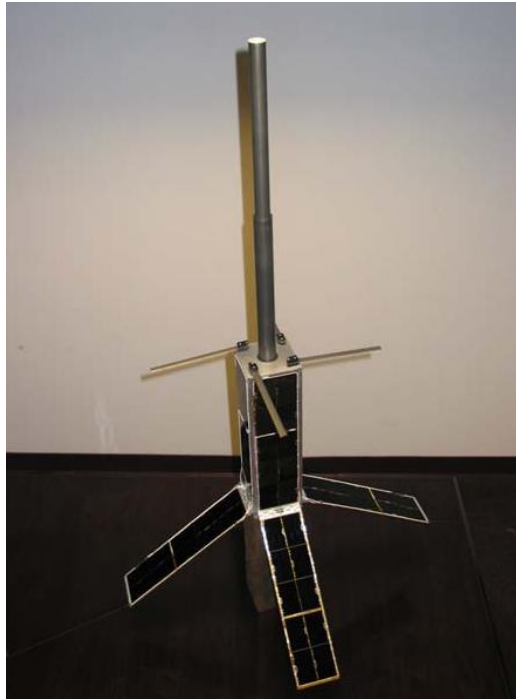
Figure 11. QuakeSat on display before shipping for launch (Flagg, et al., 2004)

    2.5.2 CubeSat Testbed 1.   Boeing first began its exploration of the potentials

of picosatellites with the successful launch and development of CSTB1 on April 17th,

2007 by an ISC Kosmotras Dnepr rocket from the Baikonur Cosmodrome in Kazakhstan

(Villaneuva, 2007). The explicit purpose of CSTB1 was to verify in house the actual

capabilities of such a satellite. CSTB1 depicted in Figure 12 was equipped with a

redundant communications system with two independent radios, two high-capacity

batteries, a deployable antenna, sun and magnetic field sensors, a simple attitude control

system that used embedded magnetic torque coils and a multifunctional board on the side

panels that contained the variety of sensors and electronics (Caday-Eames, 2006). In

addition to meeting the design and operational goals of the satellite itself, Boeing was

able to successfully integrate commercially available radios and software to establish a

simple ground station to communicate with the spacecraft; further demonstrating the

Lean manufacturing methods inherent in the small satellite system paradigm.
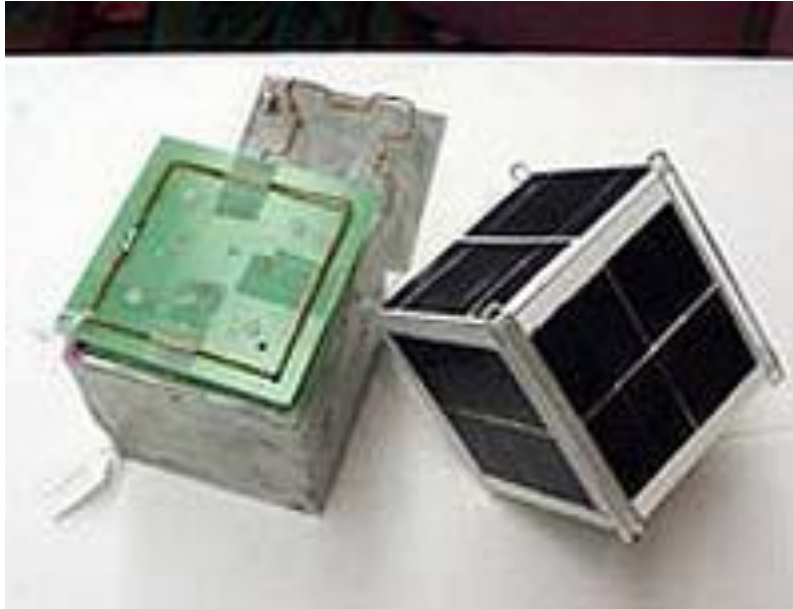
Figure 12. CSTB1 Boeing's first Nanosatellite (Boeing Completes CubeSat Mission to Advance Nano-Satellite Technology, 2007)

2.5.3 Nanosail-D.   Boeing, however, has not been the only non-academic

entity interested in the potential of CubeSats. In 2008, NASA picked up the gauntlet with

the development of its own picosatellite possessing thin membranes connected by

deployable appendages as shown in Figure 13 and Figure 14 with hopes of being the first

solar sail successfully deployed in space. While unfortunately NASA's NanoSail-D

mission ended on Aug. 2, 2008, about two minutes after launch, when the SpaceX Falcon

1 launch vehicle experienced a problem during stage separation and was unable to

achieve an Earth orbit, many aspects of the satellite design are still applicable to our

current rendering. Nanosail-D's flight had two primary objectives: firstly, to successfully

stow and deploy the sail and secondly, to demonstrate de-orbit functionality (Wharton,

Heaton, Pinson, Laue, & Adams, 2008). Solar sails work on the theoretically possible

but as of yet experimentally unverified principle of utilizing solar radiation pressure

exerted by the momentum transfer of reflected photons of light for spacecraft propulsion.

As acceleration is inversely proportional to the mass for a constant thrust, this method of

locomotion requires that the mass of the spacecraft to be as minimal as possible. Solar

sailing in and of itself is far from a novel concept with ideas of navigating the cosmos via

sails captivating the imaginations of such luminaries as Galileo Galilei and Johannes

Kepler. As Kepler once stated in letter to Galileo, "Let us create vessels and sails

adjusted to the heavenly ether, and there will be plenty of people unafraid of the empty

wastes." However, heretofore the realization of this picture of grace has belonged closer

to the realms of science fiction than to that of scientific reality. Nanosail-D, with its

deployable TRAC booms deployed from a CubeSat platform, hoped to change that.

Figure 13. Nanosail-D on the deployment testing table (NASA to Attempt Solar Sail Deployment, 2008)
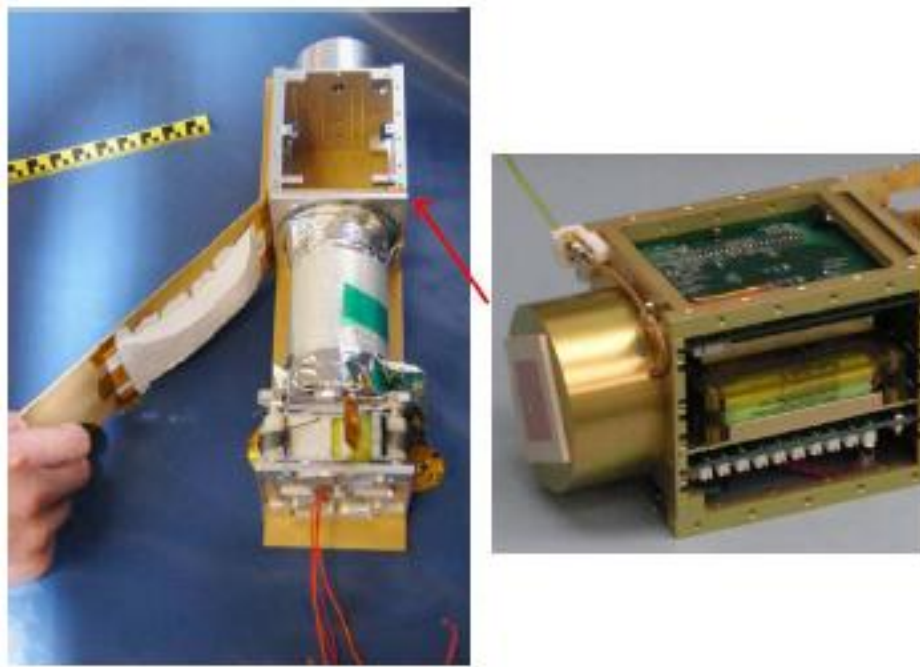
Figure 14. Nanosail-D with Close Up on the Bus (Photos Courtesy of Jeremy Banik, AFRL)

The satellite consisted of a 3u CubeSat chassis with the bottom 1/3 dedicated to the bus and 2U dedicated to the sail subsystem. The z-folded sail membranes were made from aluminized CP-1 material and rolled onto a spool. The booms themselves, called TRAC booms, were designed by AFRL to be stored with strain energy to aid in both boom deployment and sail unfurlment (Wharton, Heaton, Pinson, Laue, & Adams, 2008). Attitude stabilization will be accomplished passively via magnets imbedded in the spacecraft bus to detumble and orient the body of the craft along magnetic field lines. The SLiMSat will also utilize the TRAC booms, and is currently investigating the applicability of permanent bus magnets for passive control.

2.5.4 LightSail. Although Nanosail-D pioneered the solar sail concept, solar sailing as an interplanetary propulsion method has yet to be fully explored as the sails on

Nanosail-D were designed only to demonstrate to efficacy of de-orbiting a satellite using the atmospheric drag on deployable membranes (Friedman, 2009). The Planetary Society is currently working on a project, slated to be launched in mid 2010, which will not only support the preliminary work attempted by Nanosail-D, but verify the concept of interstellar solar sailing in its entirety called LightSail shown in Figure 15.
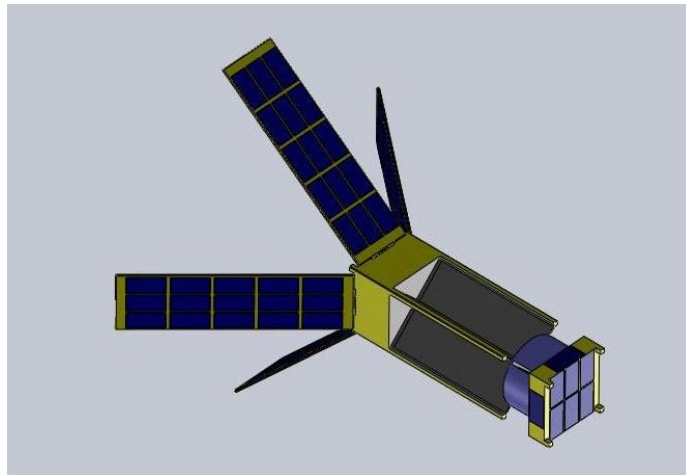
Figure 15. LightSail-1 Prior to Sail Deployment(Boeing Completes CubeSat Mission to Advance Nano-Satellite Technology, 2007)

The structure of the satellite is virtually identical to NanoSail-D with a sail subsystem contained within 2U's of the total 3U body. LightSail-1 will deploy four sails approximately 5.5 meters on a side made of aluminized Mylar 4.6 micrometers thick. Consistent with, but not strictly adhering to the CDS standard, the mass of the spacecraft mass will be minimized. Current estimates place the spacecraft mass at approximately 4.5 kilograms; which implies a mass-to-area ratio of approximately 140 grams per square meter. This mass to area ratio will provide a characteristic acceleration, that is the acceleration from sunlight at the distance of Earth, of 6.5 micro-g or 5.7×10^{-5} meters per

second squared. This acceleration is obviously miniscule, but it is constant and in the space environment could theoretically lead to faster velocities than nearly other propulsion method given enough time (Friedman, 2009). The mission of LightSail-1 is to explicitly demonstrate the increase in orbital energy caused by sunlight reflecting off the sails by monitoring the acceleration of the spacecraft with onboard accelerometers and observing the changes in spacecraft position and velocity using GPS.

The Planetary Society has plans for two subsequent LightSail missions should LightSail-1 prove successful. LightSail-2 will increase the duration of the spaceflight from days to months, while simultaneously adding more instrumentation to increase the amount of information that can be determined from its flight. LightSail-3, which will be launched after LightSail-2, will attempt to navigate to a stable orbital location other than the Lagragian points already known to exist. However stabilization will only be possible if the solar sail propulsion method proves viable and the spacecraft attitude can be controlled sufficiently to control the amount of acceleration needed to counteract the acceleration due to the large planetary bodies of the Earth and Sun. Nevertheless, instrumentation with the ability to monitor space weather significantly closer to the sun than previously possible would be of tremendous value to governments, industry and scientist alike. Hopefully, the research conducted on SLiMSat will only serve to buttress and exemplify the large potential of these picosatellites; making ambitious missions like this possible.

2.6 Tapespring Booms

While many CubeSats have been developed with a multitude of uses, the crux of this CubeSat design is the implementation and use of the TRAC booms themselves. Specifically in regards to their deployment performance and as a functional static structure once deployed. The reflectors themselves, while equally mission critical, have not been specifically utilized in previous missions and will therefore not be discussed within this section. However, there has been considerable research dedicated to the on orbit reflectivity of particular materials and therefore some explorative discussion will be entertained to this end. The CubeSats themselves have been employed in various successful missions for nearly a decade, with those of most promise and relevance being those utilizing deployable appendages.

Tapesprings are not new in space applications; with verified performance ranging from various laboratories around the world to actual on-orbit utility (Seffen & Pellegrino, 1999). A tapespring consists of a long thin strip of material possessing an arced cross section. These springs are commonly utilized today in the form of a carpenter's tape measure first seen in the 1920's. The geometry of the spring allows for a large length of spring to be wound and stowed around a circular spool in an elastically-strained configuration. The spring can later be deployed into a nearly strain-free extended position for utility.
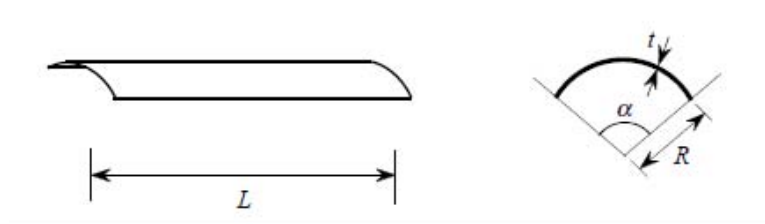
Figure 16. Tapespring Geometry(Seffen & Pellegrino, 1999)

In Figure 16, the tapespring is of length, L, uniform shell thickness t, transverse radius of curvature R, and angle α. Thus far, multiple tapesprings have been combined into at least three different configurations as shown in Figure 17 for additional stiffness and for use as booms in space applications.
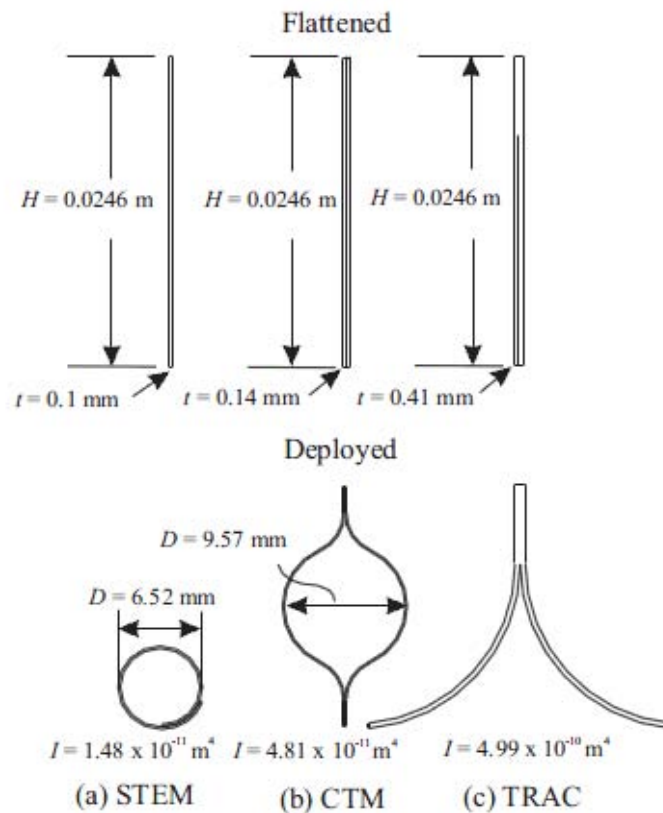
Figure 17. Cross Sectional View of Various Boom Structures(Seffen & Pellegrino, 1999)

The STEM (Storable Tubular Extendible Member) boom structure consists of a single tapespring with $\alpha > 2\pi$. A lengthwise split in the material allows for a small overlap region along an otherwise circular tube (Rimrott, September 1966). The STEM boom as pictured in Figure 17, like all tapespring booms, can be flattened and rolled in on itself in a similar manner to that of a single spring leading to the exceptionally high packagability ratios achieved by these structures. STEM booms have also been modified with $\alpha \approx 360°$ and interlocking tabs along its length to create a closed tubular structure with a higher characteristic torsional rigidity. Nested STEM booms have also been utilized toward the same end as deployable masts, low gain antennas, and to displace scientific apparatus away from the main body of the spacecraft (Pellegrino, 1994). Notably the coiling process is entirely elastic if the boom is sufficiently thin (Rimrott, 1965).

The maximum thickness of the boom is determined both by the material properties of the spring, its yield stress and modulus of elasticity, as well as the difference between its wrapped and unwrapped diameters. In principle, tapesprings, and consequently STEM booms, store elastic strain energy in their coiled configuration. If the boom was allowed to free deploy, it would eventually assume the lowest energy state of complete unfurlment. However, in the case of the STEM boom, frictional forces dissipate much of this energy and a motor is required to augment the deployment process. This motor can also retract the boom for stowage should the spacecraft utility warrant such practice. There is however, one case where the STEM boom is allowed to free deploy: the deployment of emergency beacons. The STEM is coiled inside a circular

housing and as the lid to the housing is opened, the boom extends from the center of the coil. As the boom is extending towards its unstressed state, a complex transition region develops between the flattened and fully-coiled shape and that of the tubular unfurled geometry. Remarkably, the STEM extension velocity from this configuration is approximately constant and the near free deployment itself is quite stable (Rimrott, 1965).

The lenticular boom or Collapsible Tubular Mast (CTM) boom consists of two symmetrical bell-shaped springs bonded together along both long edges. The resulting geometry forms a tubular structure which is more torsionally rigid than that of the STEM, while still benefiting from the high packagability ratio. Although not constructed from tapesprings, lenticular booms of similar geometry have frequently been implemented in larger structures such as that of the MARSIS project. The Mars Advanced Radar for Subsurface and Ionosphere Sounding (MARSIS) antenna is a lenticular boom that is part of an instrument payload onboard the European Space Agency's (ESA) Mars Express (MEX) spacecraft which launched on June 2, 2003. The satellite entered Mars orbit on December 25, 2003. MARSIS is a long wavelength radar sounder that will be used to perform measurements on the Martian ionosphere and to search for evidence of subsurface water utilizing a foldable flattenable tube boom (FFT) developed by Northrop-Gruman (Mobrem & Adams, 2006). This boom is unique among collapsible booms primarily because it is folded along specifically joints rather than coiled around a spool or drum. The resulting collapsed package is a considerably higher volume than that

of a coiled boom; working well for larger satellites, but evading further consideration on CubeSat platforms where volumetric space is limited.

The third tapespring boom structure is that of the TRAC boom. Developed by the Air Force Research Laboratory (AFRL) Space Vehicles Directorate, the TRAC boom successfully incorporates the highest cross-sectional inertia to packaged height ratio, when compared to the ratios offered by both the STEM and CTM booms. Buckling in the boom occurs along the most compliant axis and therefore the lowest quantitative moment of inertia for each respective cross-sectional geometry provides the valuable insight into the overall stiffness of the boom. According to tests performed by AFRL, the TRAC boom has 10 times more cross-sectional inertia for the same packaged height than the lenticular and 34 times more than the STEM (Roybal, Banik, & Murphey, 2007). The aforementioned property was the primary factor in our selection of the TRAC boom geometry rather than that of the CTM or STEM boom for the development of SLiMSat.
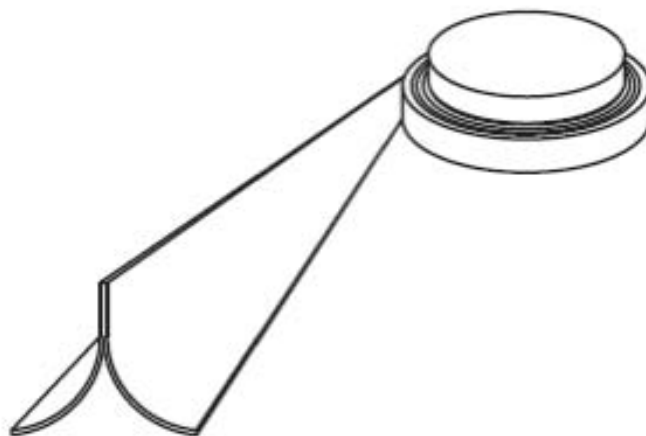
Figure 18. TRAC Boom Stowage Concept(Banik J. , 2008)

33

The TRAC developed by AFRL and shown in Figure 18 and used on NanoSail-D required a packaged height of no more than 3.5cm, a material thickness of 0.2mm, and a 6.25mm radius of curvature (Banik, 2008).

In view of the previous constraints, a list of material requirements was developed to select the design material. It was desired that the boom have high stiffness to increase the allowable natural frequencies and critical loading. For a safety factor of 1.0, the material must possess a maximum strain of $\varepsilon_{max} \geq 0.8\%$ as required by the 1 inch packaged inner diameter and a thickness of at least 0.1mm as required by the packaged volume constraint. In addition, the material had to be able to be processed into a nominally curved shape over 3m, and be joined at the ridge in some manner or formed around a knife edge in order to obtain the characteristic TRAC boom geometry. Finally the mass density of one boom must be less than or equal to $4.25 g/cm^3$ which equates to an individual boom mass of $\leq$ 200g. To meet these requirements AFRL chose a High Performance Stainless Steel called Elgiloy which possesses the following characteristics: E = 190 GPa, ε_{max} = 1.0%, ρ = 8.3 g/cm^3; all of which fit within the material selection parameters. After the booms were fabricated the startup self deployment force at each boom tip was determined to be ~1.4N. This necessitated the use of a motor for deployment which will likely be the case of SLiMSat as well.

Although the TRAC boom geometry has been fully analyzed, the deployment dynamics of this geometry has never been explicitly analyzed. However, single tapespring deployment dynamics have also been thoroughly outlined by Seffen and

Pellegrino with an emphasis on the applicably of such structures in spacecraft design (Seffen & Pellegrino, 1999). We will use the single tapespring deployment dynamics as a baseline for our experimentation and trust that many of the principles holding true for the single spring can be readily extrapolated for application into that of the TRAC boom geometry.

Seffen and Pellegrino consider the two dimensional deployment of tapesprings coiled on a free turning circular spool of radius approximately equal to that of the transverse radius of curvature of the tapespring. Here they noted that a spool with a much smaller radius will cause the tapespring to expand on the drum as soon as the deployment begins; additionally a spool with a significantly larger radius than that of the spring curvature will cause the tapespring to form a series of localized folds connected by straight pieces. Both cases, while not beyond the scope of analysis, are undesirable for our particular application and will therefore be avoided. By looking only at the case where the respective radii are equal, the boom consists of only two variable length sections: an extending straight section and an ever decreasing uniformly coiled section. Lagrange's Equations are then used to predict theoretical deployment times by analyzing the strain energy of the coiled spring and the kinetic energy with the dissipative effect of air drag on the system. This culminates in the following mathematical relationship between the boom deployment parameters:

$$\lambda = \sqrt[4]{\frac{6\mu R r^2 \alpha}{\rho L^4}} \sqrt{2t}.$$

(1)

Where, R, is the transverse radius of curvature of the spring, r, is radius of the spool, α, subtended angle of transversely curved strip, ρ, is the density of the steel tapespring, μ, is the bending strain per unit area of a thin shell, L, is the length of the boom, and, λ, is percentage of the 500mm boom that is extended off the spool.

The resulting deployment time, t, of their actual experiments plotted against the theoretical values listed below in Figure 19:
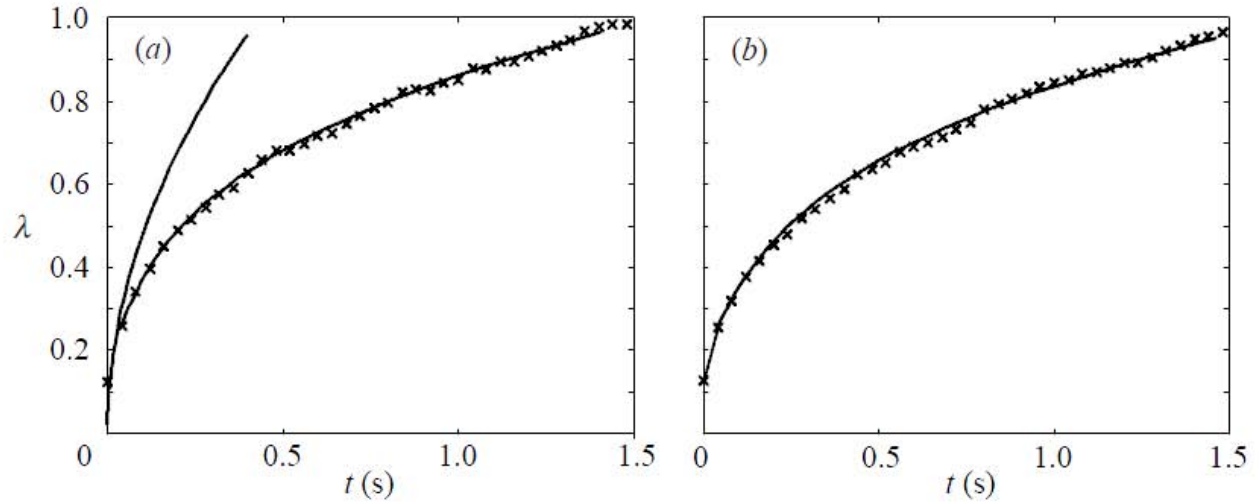
Figure 19. Deployment of coiled tapespring on a spool a) opposite sense bending with solid line obtained assuming no air drag b) equal sense bending (Seffen & Pellegrino, 1999)

The solid line in the left figure was determined by neglecting air drag effects; which correlates to the anticipated deployment behavior space. Although no tapespring deployments were conducted in a vacuum, it is clear that the assumptions made in the theoretical derivation of the tapespring behavior are justified. Presumably, using similar suppositions, the deployment behavior of the tapespring in space would also correlate

with the theoretical predictions; a useful result that can be exploited in the development

of SLiMSat as well.

2.7 Flexible Membranes in Space

Deployable membranes in space applications are far from novel. Large apertures

are used in space for communication, radioastronomy, earth-observation, and potentially

even propulsion purposes; however, in space applications, where payload volume and

weight are at a premium, it is not feasible to transport large structures intact. Deployable

structures are a potential solution providing the advantages of large structures while

working within the volume and mass constraints. Inevitably, there is a tradeoff of system

complexity. Deployment processes are inherently risky and open the potential for

malfunction before the actual spacecraft mission even begins. To date, however, there

have been many spacecraft missions that have successfully deployed reflective

membranes with significant testing undertaken for potential CubeSat applications. The

quality of deployable reflector designs are determined based on the satisfaction of at least

three distinct criteria: their compactability for launch, deployment reliability, and the

precision of deployed geometry. With the advent of CubeSats and small satellite

technology, the question of large-scale CubeSat utility depends largely on whether

deployable structures can be successfully integrated (Swartout, May 2009).

2.7.1 CRTS (Collapsible Rib-Tensioned Surface) Reflector. The

CRTS reflector is a multi-purpose deployable membrane reflector designed by Sergio

Pellegrino and the University of Cambridge (Pellegrino, 2002).
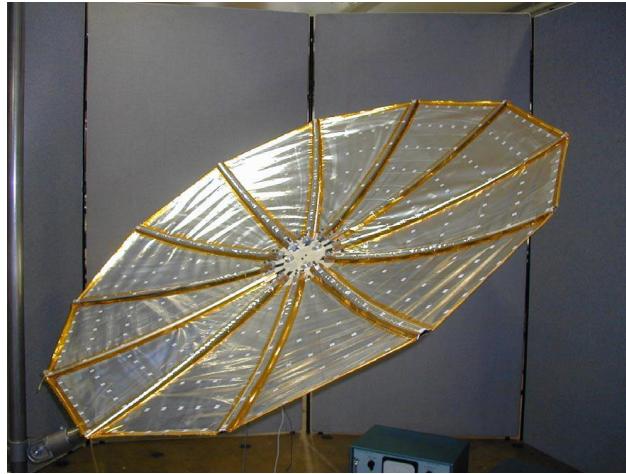
Figure 20. CRTS Reflector Small Scale Prototype (Pellegrino, Deployable Membrane Reflectors)

The reflector consists of three parts: a central hub, many foldable ribs connected radially to the hub, and a precision shaped membrane supported in tension between the ribs shown in Figure 20.

Notably, the shape of the reflector is best usable as a perfect paraboloid which, while theoretically possible, is never achieved in practice. Here Pellegrino and others used the deviation of the surface from to a best fit paraboloid as an overall root mean square to predict the accuracy of any given reflector. They found this value to depend on both the number of ribs and the shape of the membrane between those ribs. In addition, a significant area of interest in reflector design is offset, which is the measure of how far the focal axis of the paraboloid occurs away from the center of the hub. Pellegrino successfully demonstrated that specific offsets can be achieved via a circular configuration of the reflector ribs with slightly different lengths and judicious choices in pre-set rib geometry. The ribs themselves were similar to a steel tapespring with the addition of a slight longitudinal curve as well shown in Figure 21. They were composed

38

of Copper Beryllium as they can be heat-treated at a lower temperature to maintain their

shape.
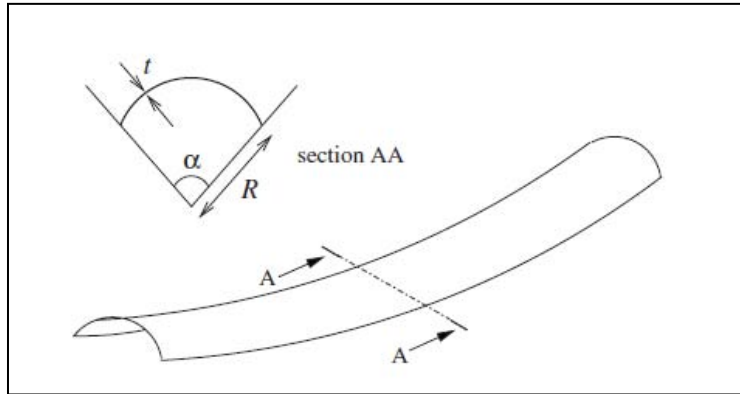
Figure 21. Doubly Curved Tapespring (Pellegrino, Deployable Membrane Reflectors)

During deployment, it was noted the ribs themselves acted as a constant moment

hinge as in Figure 22 (You & Pellegrino, 1994), which is similar behavior to what we can

expect of the tapespring booms utilized on SLiMSat.
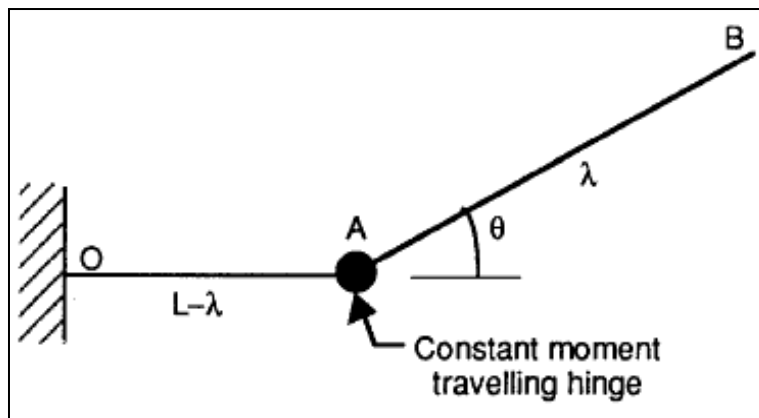
**Figure 22. Depiction of CRTS rib deployment (Pellegrino, Large retractable Appendages in
Spacecraft, 1994)**

However, the CRTS assembly is far too complex and bulky to be used in a

CubeSat application as shown in Figure 23 and Figure 24.
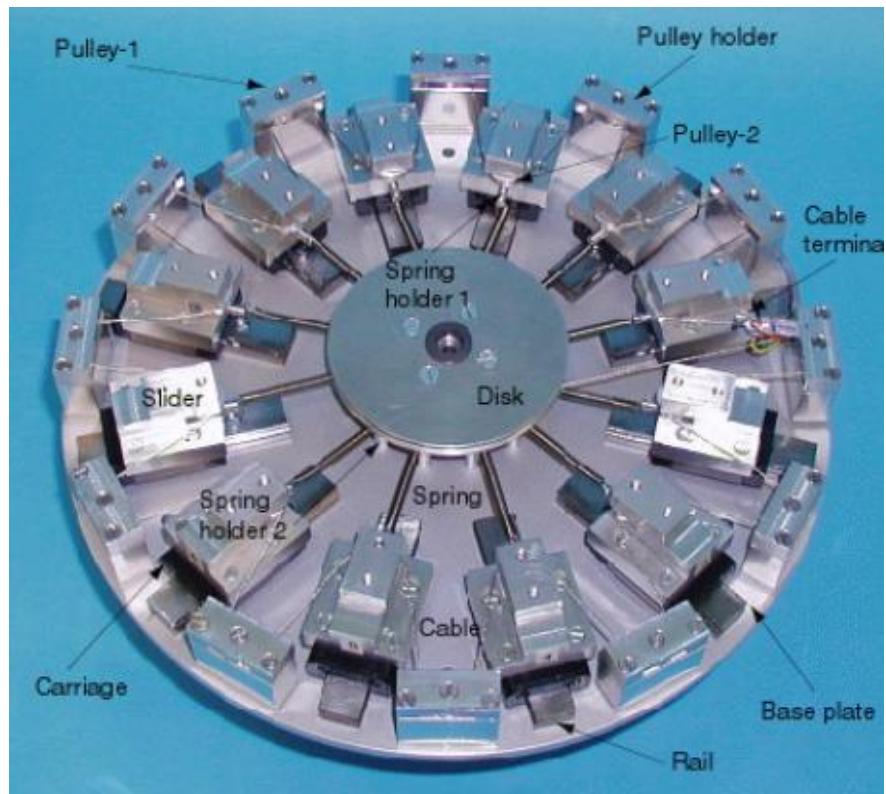
Figure 23. CRTS Hub Mechanism (Pellegrino, Deployable Membrane Reflectors)

Figure 24. CRTS Reflector in Stowed Configuration(Pellegrino, Deployable Membrane Reflectors)

40

Clearly a direct scaled-down extrapolation of the CRTS reflector could hold some potential for later CubeSats, but more likely the lessons learned from this particular reflector design will prove more valuable than the design itself for CubeSats.

Membranes like the ones proposed on SLiMSat, unfurled at the end of booms and not directly connected to the main satellite body, have never been deployed. Furthermore, the unique mission of SLiMSat presents a unique set of constraints, namely the reflective surfaces must be as large as possible at the greatest distance away from one another, providing enough resolution for lucky imaging[2] of Low Earth Orbit (LEO). In addition, knowledge of the exact boom-reflector vibrational behavior is desired as later analysis should reveal the boom motion from the detected "flashing" frequency of the satellite.

2.8 Summary

In summary, the CubeSat standardization within the P-POD assembly promotes design flexibility and reduces costs. Multiple successful CubeSat missions have been accomplished including some that include deployable structures such as QuakeSat and Nanosail-D. Tapespring booms, particularly the TRAC boom, possess remarkable potential for successful integration in SLiMSat and other AFIT CubeSats of the future. Flexible membranes have also been employed successfully in space with such structures

---

[2] Lucky imaging is a technique used for astronomical photography using a high-speed camera with exposure times short enough (100 ms or less) so that the changes in the Earth's atmosphere during the exposure are minimal. With lucky imaging, those exposures least affected by the atmosphere (typically around 10%) are chosen and combined into a single image, yielding much higher resolution than would be possible with a single, longer exposure which would include all the frames.

as the CRTS deployable membrane structure. The necessary background research for

SLiMSat viability clearly indicates that the integration of the CubeSat, boom, and

membrane components into a functional satellite is feasible.

III. Theory and Methodology

3.1 Theory Overview

The purpose of the Theory portion of this chapter is to outline the theoretical justification for the prototype development and experimental testing of SLiMSat.

3.2 Finite Element Analysis

Finite Element Analysis or FEA is a numerical technique for finding approximate answers to differential or integral equations for a model of an actual physical structure, or field problem (Cook, Malkus, Plesha, & Witt, 2002). FE analysis only finds the solution to the governing equation at distinct points called nodes. Each node is connected to other nodes via interpolated lines creating elements. These elements can assume any two dimensional line or three dimensional solid shape. The elements in total are summarily compiled resulting in a mesh that represents the actual physical structure. The power of the FE method involves the simplifying assumptions made at the nodal points themselves. Notably, the differential equations themselves are only solved at the nodal points and, by implication, provide a solution that is only valid in and around those points. More nodes and consequently more elements will provide a more accurate solution while incurring considerable of computational cost. The analyst must also remember that the FE model while appearing accurate is at best two steps away from reality. FE analysis removes the geometric complexity of the structure itself by modeling only the most fundamental features. Holes, complex chamfers, or aesthetic features are traditionally neglected as the contribute little to the global behavior of the structure itself.

Occasionally these features do affect the global behavior of the structure significantly wherein a careful analyst will include them for analysis with the knowledge that the inclusion of such complicating features will negatively impact the computational time of the result; a situation that is sometimes unavoidable. The assumptions made in the construction of the finite element model of this project are thus:

- Homogeneous materials – same properties throughout the material

- Isotropic materials – same properties in every direction

- Constant material properties over time – neglect fatigue

- Small displacements and rotations during excitation

- Fixed loads and boundary conditions

- Linear material properties, geometry, and loads.

Fundamentally, FE analysis involves preprocessing, numerical analysis, and post-processing. Pre-processing is where the analyst selects the element types, material properties, loads, boundary conditions, and mesh density. The FE model is then created and traditionally handed to a numerical solver to compute the solutions at each of the nodes. In this case the numerical solver evaluates the Eigen Value Problem for a predetermined number of Eigenpairs or a set of Eigenpairs possessing natural frequencies between particularly requested frequencies. Lastly, post-processing establishes a graphical interface wherein the analyst can view the mode shapes at each of the natural frequencies.

3.3 Modal Analysis

The procedure for solving the system of differential equations of motion for a dynamic system by transforming them into a set of linearly independent equations using the modal matrix as a transformation matrix is referred to as modal analysis (Mierovitch, 2001). Notably, coupling is not an inherent characteristic property of the system but rather of the coordinates used to describe the motion of the system. For a coordinate transformation to justify the effort, it must remove both the elastic and dynamic coupling simultaneously; which is equivalent mathematically to diagonalizing the mass and stiffness matrices at the same time. A system has many sets of orthogonal vectors, but by definition only the modal vectors are orthogonal to both the mass and stiffness matrices. As a result, a coordinate transformation based on the modal vectors is capable of diagonalizing both the mass and stiffness matrices of interest. Indeed for modal analysis to work a coordinate transformation is applied to the equations of motion using the modal vectors compiled into a matrix called the modal matrix. The result is a decoupling of the equations of motion. This allows multi-degree-of-freedom problems to be solved as a set of uncoupled single-degree-of-freedom problems. The natural frequencies of a system are those particular frequencies at which the system resonates. These are inherent or natural to the system parameters and can only be altered by changing the mass, stiffness or damping of the system. Damping is classified as any mechanism that removes energy from the system and is present in all real systems. However, in the case of the tapespring beams structural damping is minimal and will be approximated by a viscous damper in a later stage of the analysis. This should not hinder our understanding of the beam

45

dynamics nor prove to be a significant modeling hurdle later. Mode shapes are the

normalized shapes that the system assumes when resonating at that particular modal or

natural frequency.

The following is in reference to (Mierovitch, 2001). The displacement vector

containing the displacements of each node for every degree of freedom is represented by

the displacement vector $\bar{x}(t) \in \mathbb{R}^{n \times 1}$; and the corresponding acceleration vector

$\ddot{\bar{x}}(t) \in \mathbb{R}^{n \times 1}$ is the response to loads $F(t)$ as a function of time.

For complex structures the discretized EOM can be written in the time domain as

$$M\ddot{\bar{x}}(t) + (1 + i\gamma)K\bar{x}(t) = F(t) \tag{2}$$

Where γ represents the structural damping usually pulled from an appropriate

table. In our case, where the structural damping is minimal this equation simplifies to the

undamped free vibration case,

$$M\ddot{\bar{x}}(t) + K\bar{x}(t) = 0 \tag{3}$$

Here we assume that all the coordinates assume the same motion traditionally

denoted a synchronous motion solution.

$$\bar{x}(t) = \bar{\phi}e^{i\omega t} \tag{4}$$

Where ω is the radian frequency and $\bar{\phi}$ is a constant real vector of dimension n x

1. Substituting this expression for $\bar{x}(t)$ into the previous equation and letting $\lambda = \omega^2$

results in the eigenvalue problem (EVP):

$$K\bar{\phi} = \lambda M\bar{\phi} \tag{5}$$

The above equation has non-trivial solutions where the characteristic determinant is equal to zero stated symbolically

$$\det[K - \lambda M] = 0 \tag{6}$$

Solving the EVP for λ or Eigenvalues resolves *n* non-trivial orthogonal solutions of $\bar{\phi}$ called eigenvectors. These Eigenvalues are typically distinct, but only a subset of the total number of Eigenpairs is retained. Each Eigenpair consists of the Eigenvalue and its associated eigenvector. The modal matrix Φ consisting of the *l* eigenvectors of interest can now be compiled

$$\Phi = [\bar{\phi}_1, \bar{\phi}_2, \dots \bar{\phi}_l] \tag{7}$$

Mass normalizing each eigenvector in Φ, the mass and stiffness matrices are diagonalized into the modal mass and stiffness matrices where *I* and Λ are of size *l* x 1 respectively

$$I = \Phi^T M \Phi \tag{8}$$

$$\Lambda = \Phi^T K \Phi \tag{9}$$

The modal mass matrix is identically equal to the identity matrix *I* as it was mass normalized while the modal stiffness matrix is a diagonal matrix with Eigenvalues along the diagonal. The modal mass and stiffness matrices are then used to calculate the modal frequency response of the structure to an input force $F(\omega)$

47

$$X(i\omega) = \Phi(-\omega^2 I + (1 + i\gamma)\Lambda)^{-1}\Phi^T F(\omega) \qquad (10)$$

With the magnitude $|X(i\omega)|$ and phase angle $\rho(\omega)$ calculated from the real Re and imaginary Im values of $X(i\omega)$

$$|X(i\omega)| = \sqrt{[ReX(i\omega)]^2 + [ImX(i\omega)]^2} \qquad (11)$$

$$\rho(\omega) = \tan^{-1}\frac{-ImX(i\omega)}{ReX(i\omega)} \qquad (12)$$

Notably, peaks in the magnitude occur at the natural frequencies and the mode shape at those frequencies can be determined by examining the magnitude and phase information at different nodes. This research hopes to build an FE model that closely matches that of the measured beam performance to better predict the on-orbit post deployed behavior of the beams. With the insight provided by an accurate model we can inexpensively analyze the behavior of the beams themselves in environments that are beyond the scope of practical testing but still well within the bounds of operational application. First, however, we must match the Eigenvalues and eigenvectors of the model to that of measured data with known inputs and outputs before we can hope to extrapolate its uses.

3.4 Polytech Laser Vibrometer

The Polytech Laser Vibrometer provides a non-contact method of obtaining the characteristic vibration information from a mechanically vibrating system. This method of non-contact data collection is ideally suited to our application which involves the detection of the natural modes of thin flexible structures, such as the tapespring booms.

The laser uses the principles of a heterodyne interferometer which generates a high frequency carrier signal on the photo detector with the aid of an acousto-optic modulator (AOM), or Bragg cell(Polytec, 2007). The beam of a helium neon laser is pointed at a vibrating object and scattered back from it to create the velocity measurement. The velocity or displacement amplitude of the vibrating object generates a frequency or phase modulation of the laser light respectively due to the Doppler Effect. The signal processing unit, with the aid of appropriate demodulators or decoders, recovers the modulated signal. The simplified laser path is shown in block-diagram-like form in Figure 25 for reference. For the purposes of the SLiMSat boom testing, the frequency modulation of the Doppler signal is used to recover the velocity information of the vibrating beam.
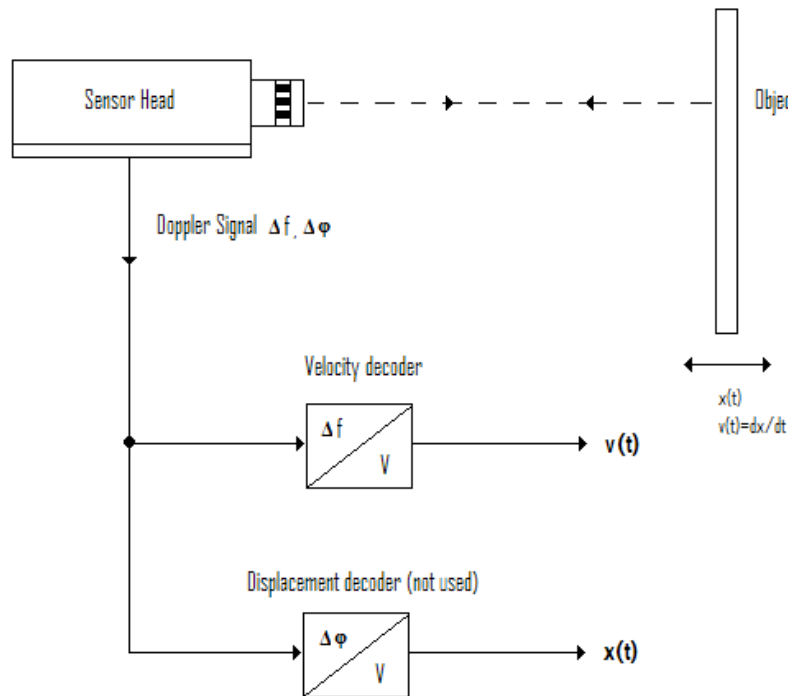
Figure 25. Signals in the Vibrometer (Polytech, 2007)

The Doppler equation and subsequent wavelength relationships are seen clearly

from this equation (Rees, 2001):

$$\frac{\lambda_d}{\lambda_t} = \frac{\sqrt{1-\frac{v^2}{c^2}}}{1-\frac{v\cos\theta}{c}} \qquad (13)$$

Where λ_d is the detected frequency, λ_t is the transmitted frequency, c is the speed of

light, θ is the angle of the detector in relation to the source, and v is the velocity of the

particular laser point. With the single head laser the angle from the detector to the source

is fixed but care must be taken to ensure that the laser head itself is within +/- $10°$ of

parallel with the scan point to stay within a small angle approximation window.

Once the velocity of the scan point is known, one can either solve time domain

differential equations of the previous section or more commonly transform the data into

the frequency domain where information can easily be extracted from plots of $X(\omega)$

versus ω and $\phi(\omega)$ versus ω than from $x(t)$ versus t. The Polytech Laser Vibrometer

software utilizes a computationally efficient method, the fast Fourier Transform (FFT), to

convert the time domain signal into the complex frequency domain. The fast Fourier

Transform uses a precursor of the ordinary Fourier Transform:

$$F(\omega) = \int_{-\infty}^{+\infty} f(t)e^{-i\omega t}\,dt \qquad (14)$$

Where $F(\omega)$ is the frequency domain signal, $f(t)$ is the time domain signal, and ω is the

frequency. However, the sampling of the signal creates a set of finite points from the

continuous signal so the discrete Fourier Transform must be used to convert the

discretized data into the frequency domain for N number of samples:

$$F_n = \sum_{k=0}^{N-1} f(t_k) e^{-int_k} \qquad (15)$$

However, for a discrete sequence $\{X_r\}$ containing N points the direct calculation provided by the discrete Fourier Transform (DFT) would require N^2 operations. The FFT is a computer algorithm that works by portioning the sequence $\{X_r\}$ into a number of shortened sequences, computing the DFT of those shorter sequences, and then recombining them to yield the full sequence. The resulting Fourier Transform requires $N \log_2 N$ operations, or 341 fewer operations to convert to the frequency domain as compared to the DFT (Cobb, 2009). However it is worth noting that only the first 0,1,…,N/2 components of the discrete sequence $\{X_r\}$ are unique; the last N/2 components represent negative frequency components and therefore constitute redundant values (Cobb, 2009). The N real time record is mapped to N/2 complex values where the particular N/2 value is referred to as the Nyquist frequency. By implication, sampling must take place at a minimum of twice the frequency of interest to accurately represent it with the FFT.

In theory, the vibrometer software could utilize the respective FFT's of the input and output to calculate the FRF from the following relationship:

$$FRF = \frac{output\ FFT}{input\ FFT} \qquad (16)$$

In practice, however, the FRFs are actually estimates based on the spectral densities of the sampled data. By taking the FFTs of the correlation functions of the input and output

data we obtain the spectral content of the time signal $x(t)$. The spectral densities as

related to an input FFT, x, and an output FFT, y, are:

$$S_{yy}(\omega) = y(\omega) \cdot \bar{y}(\omega) \tag{17}$$

$$S_{xx}(\omega) = x(\omega) \cdot \bar{x}(\omega) \tag{18}$$

$$S_{xy}(\omega) = x(\omega) \cdot \bar{y}(\omega) \tag{19}$$

$$S_{yx}(\omega) = y(\omega) \cdot \bar{x}(\omega) \tag{20}$$

From the spectral density functions two estimates of the FRF emerge, namely $H_1(\omega)$ and

$H_2(\omega)$

$$H_1(\omega) = \frac{S_{xy}(\omega)}{S_{xx}(\omega)} \tag{21}$$

$$H_2(\omega) = \frac{S_{yy}(\omega)}{S_{yx}(\omega)} \tag{22}$$

Where $H_1(\omega)$ is sensitive to the input noise of the signal and provides a lower bound

estimate for the actual FRF; and $H_2(\omega)$ is sensitive to the output noise of the signal and

provides an upper bound to the actual FRF. Neither $H_1(\omega)$ nor $H_2(\omega)$ represent the

actual relationship between the input excitation and the output response, but they provide

both an upper and lower bound for the response based on the realistic presence of signal

noise. For the laser vibrometer measurements the output noise is generally larger than

the input noise and thus $H_1(\omega)$ was used as an estimate for the FRF. To further mitigate

the effects of noisy data, averaging was used for each laser point.

Coherence measurements were also used to distinguish credible data from suspect data. Coherence is a ratio of input noise to output noise specifically of how well the data is linearly related to the input

$$Coherence = \frac{H_1(\omega)}{H_2(\omega)} \tag{23}$$

Data can have poor coherence for a number of reasons including: nonlinear structures, digital filter leakage, time delays and uncorrelated noise in the measurements of the input and output data-stream. The tapespring booms in particular, while assumed to behave linearly for all excitations, required large amplitude excitations in order to overcome the ambient low frequency ever-present in the lab testing environment. These large magnitudes made the work of collecting data with good coherence at all frequencies exceptionally difficult.

3.5 SLiMSat Design and Development

The overarching goal in AFIT's production of SLiMSat is to increase CubeSat utility. Current CubeSat capability has plateaued where usage beyond the walls of academia appears compelling in concept but is still beyond reach. It is, however, assumed that the demonstration of deployable structure viability, both in terms of functionality and repeatability will be the touchstone for future, more capable satellites. Towards that end, SLiMSat's design will further characterize the TRAC boom's design and functional limitations, explore the possibilities of deployment monitoring and on-orbit tracking from ground stations, and establish a solid analysis of the exact requirements needed for the development of this and future satellites.

SLiMSat's design holds distinction among CubeSats as the only platform to incorporate unfurling flexible membranes located at the end of flexible booms. The selected design was the result of iterative analysis following the outline laid out by NASA's Engineering Design Process. The process, depicted below in Figure 26 will serve as a context for future discussion as well as to reinforce the iterative nature of the design process so as to help others who choose to follow.
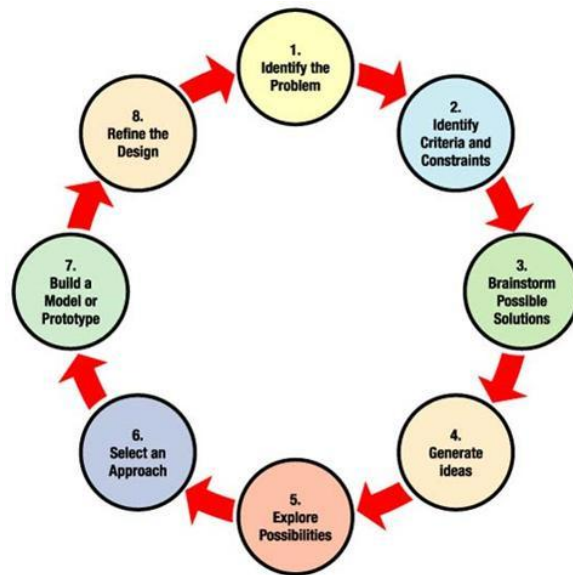
Figure 26. NASA's Engineering Design Process(NASA Engineering Design Challenge)

In order to select the best quality design to accomplish the SLiMSat mission multiple design alternatives were examined quantitatively against our design criteria. The most challenging and novel engineering aspect of SLiMSat's design is that of the membrane deployment. Deployable boom end reflectors are a precursor to future designs such as that of a parabolic dish which, if implemented successfully, could significantly expand the scope of current CubeSat capability. As SLiMSat's most challenging and

potentially exciting design aspect, the deployable reflective membranes are inevitably the most critical design component.

3.6 Summary of Theory

SLiMSat was designed in consideration of the multiple advantages and limitations of the TRAC boom geometry. In order to deploy these booms from a CubeSat, the more knowledge we have of their exact performance characteristics, the better our resultant design will be. The theoretical tools provided by finite element and modal analysis combined with the data gathered though laser vibrometer signal processing, will provide more than sufficient data to determine the baseline characteristics of the TRAC booms used on SLiMSat and ensure a quality satellite design.

3.7 Methodology Overview

Clearly the development of deployable booms on a CubeSat platform will increase the operational utility of the CubeSat. However, in order to fully integrate deployable booms into the CubeSat form factor, the TRAC booms themselves need to be well characterized in the exact orientation they would experience in space. Space, however, is a difficult environment to replicate. Furthermore, the booms themselves resonate at exceptionally low frequencies; which makes isolation from ambient vibrations particularly difficult. In this case, an accurate computer model of the booms would be optimal. Simulations without gravitational or aerodynamic effects could be conducted quite easily without the time or expense of conducting the same experiments in the lab. It should be noted however that even accurate computer models are, at best, only close

approximations of the actual structural behavior, not exact depicters of structural performance. In the case of CubeSats, where detailed information is often not desired, a close estimate is often good enough. Hence if a computer model of the boom is developed, and that model is determined to be a close approximation of the actual boom vibrational behavior, a great deal more about those booms can be learned from the model without the time or monetary expense of conventional laboratory testing. Notably, it is to this end that the extent of testing was geared.

The testing for SLiMSat occurred in three development stages in order to verify its viability as a design and future development. The first was the development of a finite element model. After the components were modeled in SolidWorks, their geometry was loaded into FEMAP for finite element analysis. The goal of the finite element model was to develop an accurate representation that could be used to predict the behavior of the satellite on-orbit. The model data would then supplant, or at least augment, the need for future deployed configuration testing which would be exceptionally time intensive and expensive to conduct. The second development stage was that of model verification. Here the Polytech Laser Vibrometer was used to measure the input-output relationship to a known input at various points along the beam for future comparison to those same points in the model. If those points were shown to exhibit similar motion at many frequencies of interest, one could speculate that the model is a close approximation of the actual beam behavior at those particular points. The last stage of development testing involved the deployment of the booms and membranes themselves; notionally, do the booms and membranes successfully and repeatedly deploy

from the satellite. A secondary test was also conducted on the deployed satellite with the objective of discovering whether the deployment of the booms would be detectable at the CubeSat chassis.

Each test was necessarily focused such that the results from any given test will drive our design constructively or destructively towards a better end state. The determination of test success or failure should be viewed as whether that particular test qualitatively accomplishes the objective; whether the data gleaned from a particular experiment or model elucidates a conclusive answer. By establishing a baseline objective for each test, both the common pitfall of testing for the sake of testing and the "paralysis of analysis" are avoided. This section will outline a modeling and testing method which, while far from inclusive, will provide a proper heuristic for the boom deployment from a CubeSat and provide a proper footing for those individuals who follow.

3.8 SLiMSat Design and Downselect

Notionally, the design of SLiMSat should produce a satellite with deployable reflective surfaces at a maximum distance from one another; the greater the distance between the membranes, the greater the likelihood of optical resolution from ground-based imagers. In addition, satellites with larger deployable structures have a greater potential to expand the overall utility of all CubeSats as they more closely mimic the performance of their larger satellite cousins. With this single design objective, and the self- imposed constraint of utilizing the deployable TRAC booms, several potential designs were considered. From inspection, the TRAC booms themselves have two

57

distinct methods of stowage when aboard the satellite: folded and stored, or wrapped around a spool. Although folding the booms would seem an acceptable stowage method for short section of boom, the wrapped stowage method was clearly superior for the stowage of large beams. For example, Nanosail-D was able to store four 2.25m booms, equating to 9m of total boom length around a single reel. A 3U CubeSat using four folded booms could potentially deploy a mere meter of total boom is the boom was folded 8 times along each 30cm side of the satellite. Additionally, with so much boom essentially stuffed within a small cavity, binding and entanglement issues are a near certainty.

After the determination to wrap the booms was made, the next major design choice was to use four booms of two different lengths to provide the maximum potential of passive on-orbit dynamic characterization. Satellites with fewer booms are decidedly less complex; however, the passive design of SLiMSat required that the on-orbit satellite behavior be resolvable independent of orientation. More booms would increase the satellite visibility from the ground, while simultaneously increasing the deployment risk. Hence, a satellite possessing four booms of two lengths provided an optimum balance between the potential for optical detection and the satellite level of complexity. The specific orientation of the satellite could be passively determined from the frequency identification of the flashes of reflected light at the varied boom lengths. However, a planar four boom design also necessitated some out-of-the plane dimension of the reflectors themselves in order to detect the projected on-orbit dynamics for a satellite rotating about either the intermediate or minor axis.

It was clear, even from an early stage, that the best design for SLiMSat would be

the design solved the problem of membrane deployment and stowage most gracefully.

As preliminary design concepts were explored several possible boom end designs

emerged, aptly named: the 'Origami', the 'Sunshade', the 'Balloon', and the 'Frogleg'

boom ends depicted in Figure 27.
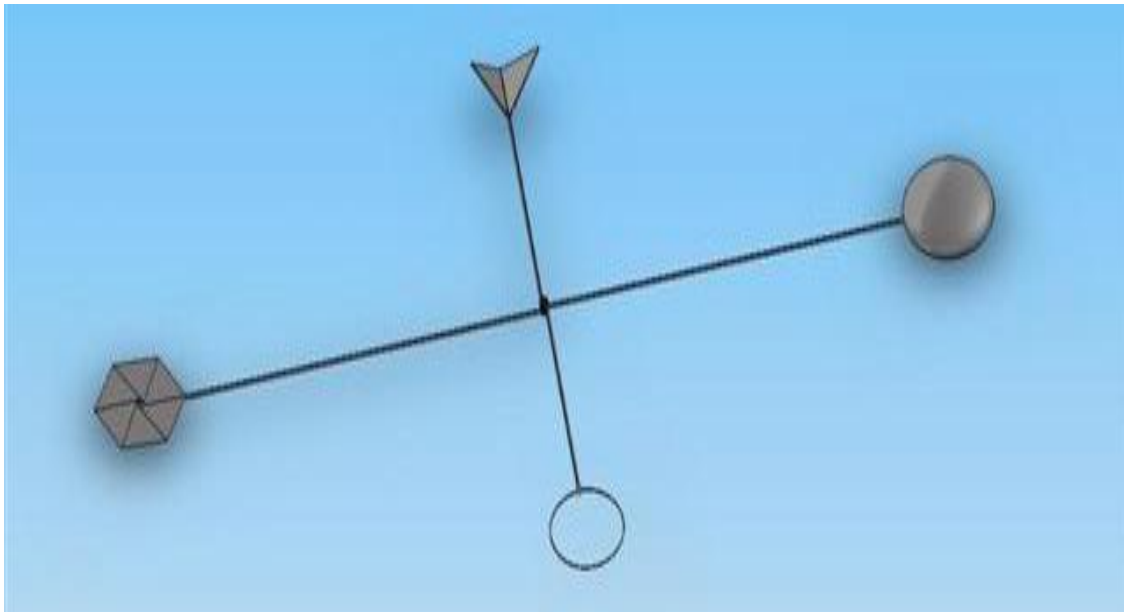
Figure 27. Boom End Design Alternatives (clockwise from top: 'Frogleg', 'Balloon', 'Sunshade', 'Origami')

Initially a triangle end design existed as well, created by removing the laser weld

along the last portion of the beam weld and connecting the two halves of tapespring at the

tips to form a triangular frame. However, it was clear that this design was inferior to the

rest.

For example, the Triangle design provided approximately one fifth the reflective

surface area as that of the 'Frogleg' or 'Balloon' for the same amount of dedicated TRAC

boom. Also of note, the Triangle design ends preferred a particular orientation upon

deployment. If deployed in space, this uncommanded flop would create a large

unbalanced torque, possibly rotating the satellite into an unknown or undesired

orientation.
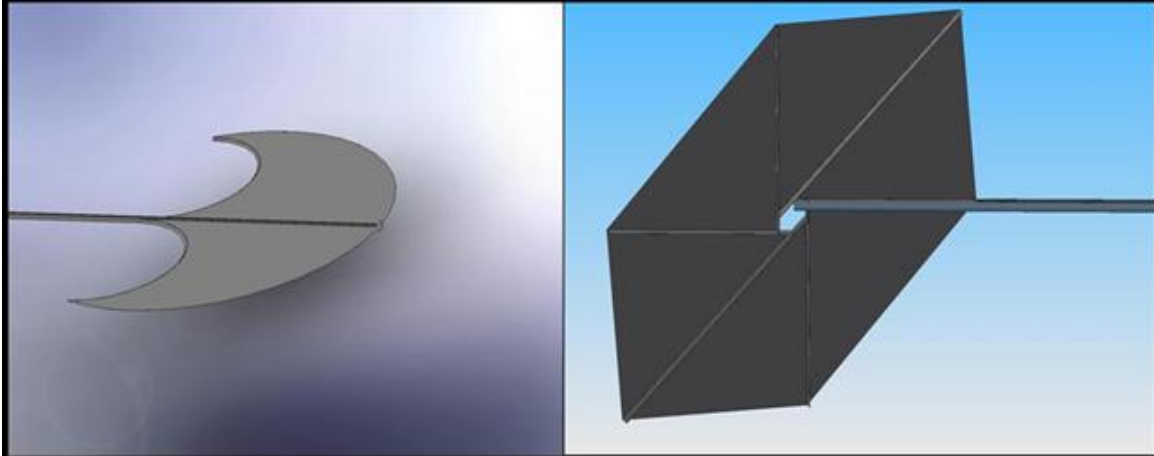
Figure 28. Early 'Frogleg' boom end design (Left), 'Origami' end design close-up (Right)
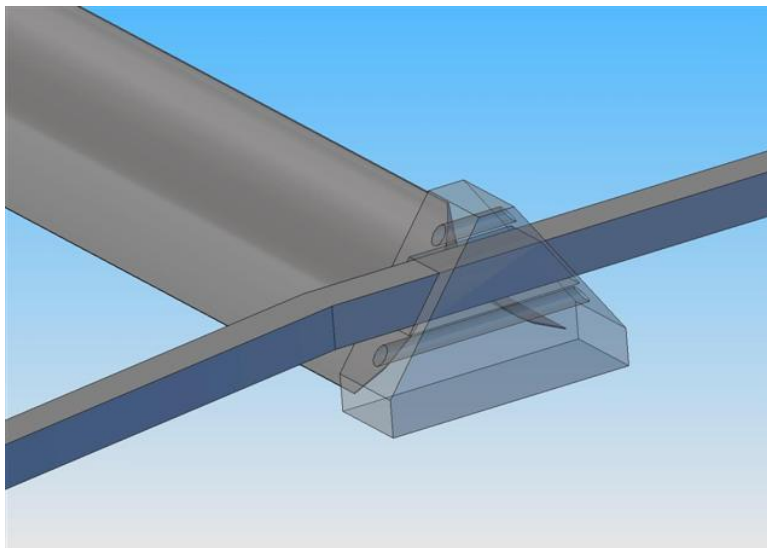
Figure 29. 'Sunshade' End Design Connection to Main Boom

Figure 28 provides a closer view of both an early notional 'Frogleg' and

'Origami' boom-end designs where the flat surfaces represent the reflective membrane

placement. SolidWorks modeling was an invaluable preliminary design tool, providing a

canvas where ideas could be more fully explored without the time and expense of

physical modeling. In addition, drawings were frequently used to explain the specifics of

each design to other members of the committee. Through the use of SolidWorks the

particular flaws of each design were also readily apparent.   The 'Sunshade' design idea

used a flexible wire within a reflective membrane much like the circular sunshade used in

the automobiles. Although an apparently viable concept, it became clear from the design

interfaces that its implementation would be far from trivial. Indeed, how to connect the

reflective surface end to the main boom as in Figure 29, as well as how to store the

undeployed membranes were the greatest design challenges.
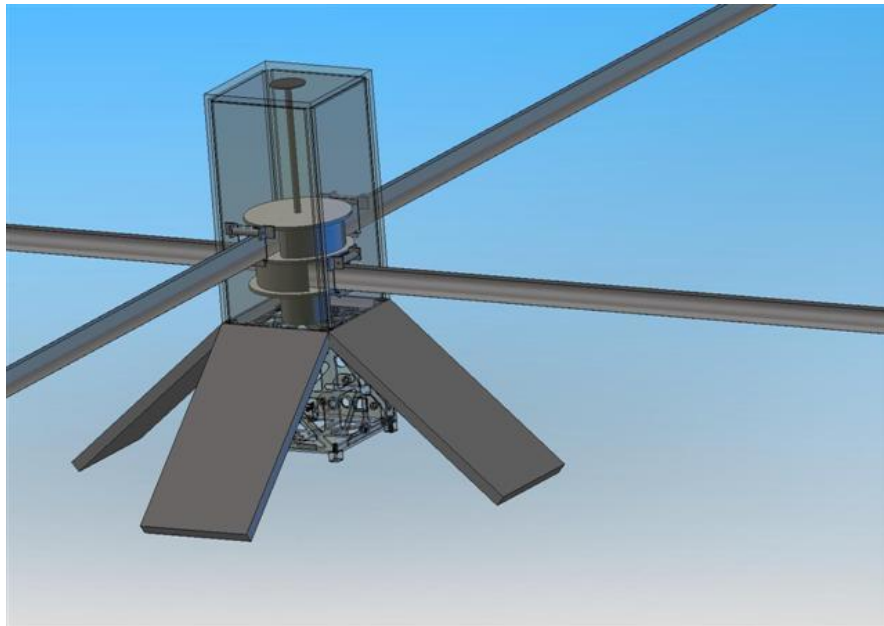
Figure 30. Envisioned Membrane Stowage Cavity developed for 'Sunshade' Boom-end Design

Figure 30 depicts the stowage cavity for the 'Sunshade'-end design along the wall

of the CubeSat beneath the solar panels. This design was later abandoned as the

increased complexity was overshadowed by the simplicity and presumed increased reliability demonstrated by the 'Frogleg' design.

The 'Origami' boom end depicted in Figure 28, was also discredited as the final design for similar reasons. The increased complexity and added bulk of the membrane spars was difficult to stow alongside the satellite body. It was also thought that an evacuated balloon could be folded and stowed within the CubeSat body. Once on orbit, the balloon would deploy and an extremely small volume of pressurized gas could be used to inflate the balloon to exceptionally large dimension. However, the increased potential for deployment malfunctions exempted this design from further consideration.

Connecting the membrane to the boom itself was also a significant design problem. Through considerable trial-and-error and consultation with Jeremy Banik at Kirtland AFRL, the best method of attaching the membrane to the booms appears to be the indirect attachment with string. Multiple epoxies were tried unsuccessfully in order to discover the optimum method of adherence, including: N-bond, Gorilla Glue, and Super Glue, with the best results, coming surprisingly, from tape. Tape, while inexpensive and easy to manipulate, has its own issues with outgassing and thermal cycling, and is generally not preferred in space applications. Kapton tape remains the exception, but would not be ideal in this instance where the membrane-adhesive-boom interface is likely to be strained in multiple directions at various times. Another suggestion involved sewing the membrane to the boom rather than gluing it down. The benefit of stitching is that membrane would be allowed to flex enough so that the

shearing of the material is less likely while retaining the close interface distance of the epoxy. The close interface distance provided by the stitching method would be less likely to entangle and allow multiple attachment points to lessen the overall stress of the reflective fabric.

However, for the 'Frogleg' and other boom end designs it was increasingly clear that an indirect method of attachment might be of some benefit. The indirect method of attachment is nearly identical to the one ingeniously devised by Mr. Banik and others at AFRL, essentially utilizing a string and grommets put into both the membrane and the boom on Nanosail-D as in Figure 31. The beauty of this design method is that it allows for the booms to be stored on the hub and the membranes to be stored in a nearby location with only the string having to pass through the interface.
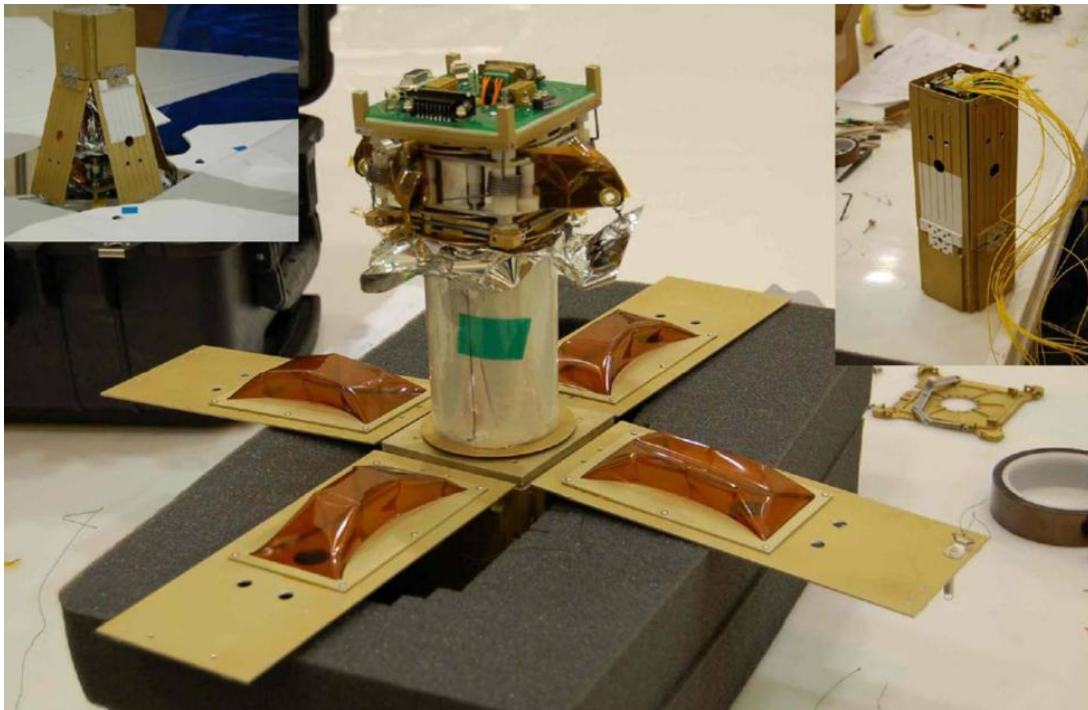
Figure 31. Nanosail-D Membrane Attachment (Photo Courtesy of Jeremy Banik, AFRL)

Clearly, many reflector designs would facilitate passive on-orbit detection and dynamic characterization from ground-based telescopes; hence, quantifiable measures of design quality were developed to distinguish proposed designs from one another.

Table 1. Design Quality Ranking Matrix

Design Quality Matrix (Design rankings in comparison to one another)	Origami	Sunshade	Balloon	Frogleg
Available Membrane Stowage Volume	1	2	4	3
Boom End Rigid Structure Stowage	2	2	4	3
Post Deployment Stability	4	4	1	3
Deployment Complexity	1	3	1	4
Reflector Surface Area*	2	2	4	3
Totals	10	13	14	16

4: Most Desirable Performance
1: Least Desirable Performance

The ranked measures of quality were: available membrane stowage volume, boom end rigid structure stowage, post-deployment stability, deployment complexity, and the square meters of reflective surface, noting the orientational dependence of the satellite dynamics. However numerous correlated factors were also considered for each design: the reflectivity of multiple surface materials; the available baseline length, assuming boom ends infringement on payload capacity; packagability ratios; the overall mass of the respective boom-end designs; the assumed potential of reliable deployment; the boom end design effect on boom deployment degradation; and the presumed deployment shock

to the satellite (Swenson, 2010). Each design was ranked against the other prospective

designs with higher rankings indicating more favorable design performance.

For SLiMSat's final boom end design selection it was ultimately the lack of clean

solutions to the problems of membrane stowage and main boom connection that led to

high ranking and subsequent selection of the 'Frogleg' boom end as the design of choice.

3.9 Finite Element Modeling

Once the decision was made to utilize the TRAC boom geometry as opposed to

either the lenticular CTM boom or STEM boom, a finite element model of a boom

section was developed. A prototype of the TRAC boom geometry was constructed by

adhering two sections of tape measure spring along a single edge with packaging tape.

The resulting TRAC geometry was then fixed inside of two short sections of 8020

Aluminum to serve as end masses and retain the tapesprings in the desired shape as

depicted in Figure 32. The resulting structure was then bolted to a steel plate vertically to

minimize the effect of gravity on the boom's motion and excited by an impulse hammer

while measurements were taken with the Polytech laser vibrometer as depicted in Figure

33. For preliminary modeling considerations only a single laser point was needed as the

model sought to match only the natural frequencies themselves and not the mode shapes.

The natural frequencies will be evident at every point along the beam as long as the

measurement point selected is not a nodal coordinate for a particular natural frequency.

In addition, the modal motion was significantly gross and the frequencies low enough

that modal shapes for the first three natural frequencies could be detected and loosely

verified and by visual inspection.

Figure 32. TRAC Boom Geometry Test Section
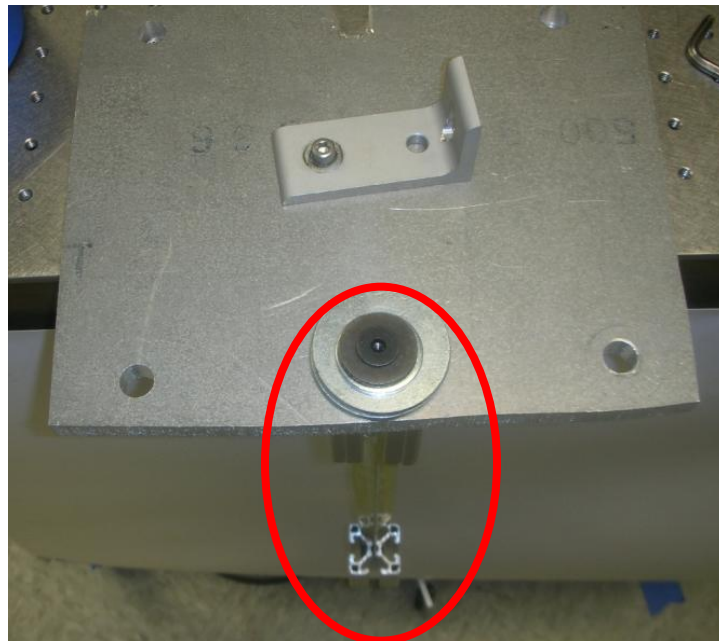
Figure 33. TRAC Boom Test Section Fixed End (Top View)

66

Preliminary testing indicated natural frequencies at 7, 15, and 23 Hz. Several

models were then constructed of the test section from a variety of elements, namely:

simple plate elements with no curvature making a "v" cross section as in

Figure 34, beam elements with the same "v" cross section, beam elements with a

realistic TRAC cross section, and plate elements along a realistic TRAC cross section.

The results of these different models and their respective errors are shown in Table 2.

Notably, no particular element type was able to capture the first natural frequency value

very closely. This could be due to aerodynamic drag effects that were omitted in the

model, and incorrectly assumed to have negligible effects on the measured data.

However, from this cursory analysis it is clear that a realistic plate element model of the

beam itself will generate the best approximation; potentially generating some insight into

the behavior of the actual deployed boom structure while matching several frequencies of

the most dominant modes.
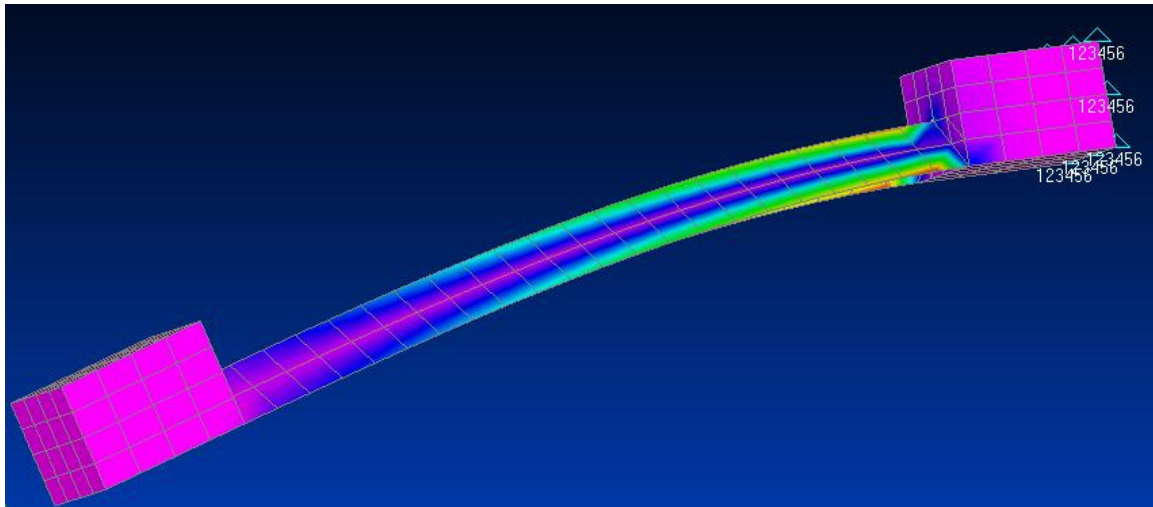
Figure 34. Finite Element Model of Test Section with Simple Plates

Table 2. Measured and Modeled Natural frequencies for section of TRAC Boom

	Natural Freq 1	% Error	Natural Freq 2	% Error	Natural Freq 3	% Error
Measured (Hz)	7		15		23	
Simple Plates (Hz)	2.5	64%	24.5	61%	28.2	18%
Plates with Beam (Hz)	4.2	40%	41.2	175%	22.75	1%
Realistic Beams (Hz)	N/A	N/A	53.6	257%	78.85	243%
Realistic Plates (Hz)	3	57%	18	17%	22.2	3%

3.9.1   Modeling the Four Meter Boom.   Using the results from Table 2 another model was created of the full 4m boom without any reflective surfaces attached as in Figure 35.
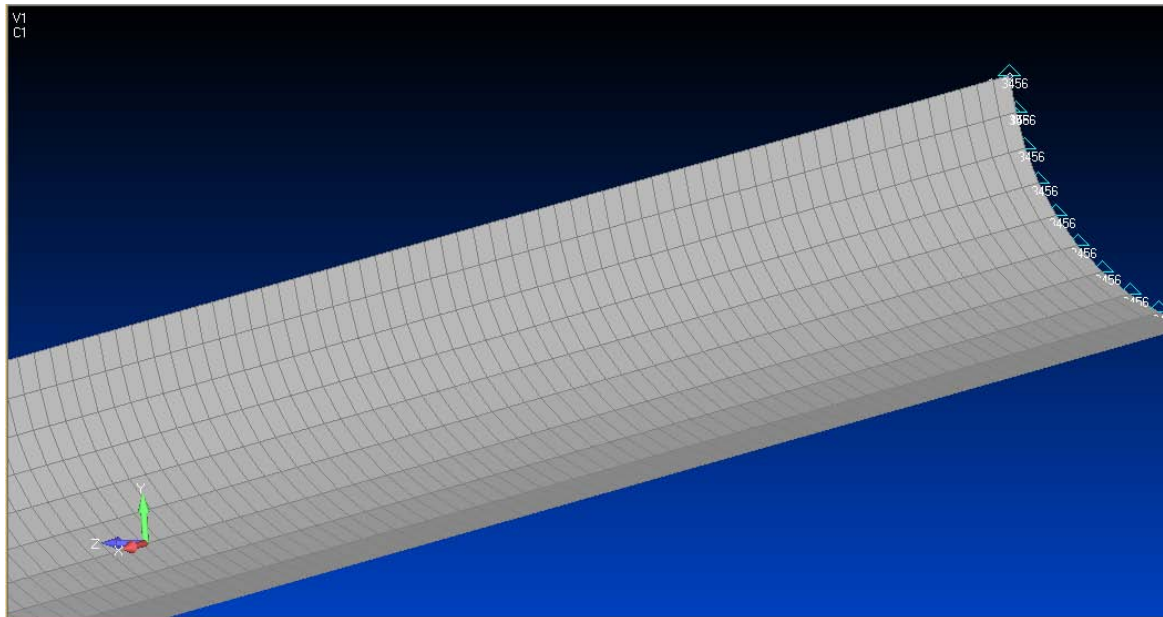
Figure 35. 4m Boom without Reflectors Model Close-Up

It was clear that any reflective membrane or support structure would have highly non-linear dynamics, and would thus be very difficult to model accurately for multiple modal frequencies. By accurately modeling a simple boom structure without any end mass, later models could be developed with end structures and would ensure any errors present in future models would be due to the inaccurate modeling of the reflective membrane support structure or the membrane itself, not the boom.

The modeled boom was constrained at one end by fixing the displacements and rotations of the all the nodes on one end of the beam. This constraint is somewhat unrealistic as the actual fixation of the physical boom utilizes friction fit blocks inside a hub cavity which, while closely approximating a perfectly rigid constraint, can never completely restrain the motion of the boom. Additionally, the tapespring was modeled as one completely uniform piece as in Figure 36, when in actuality the boom was fabricated by laser welding two pieces of tapespring together along a single long edge.
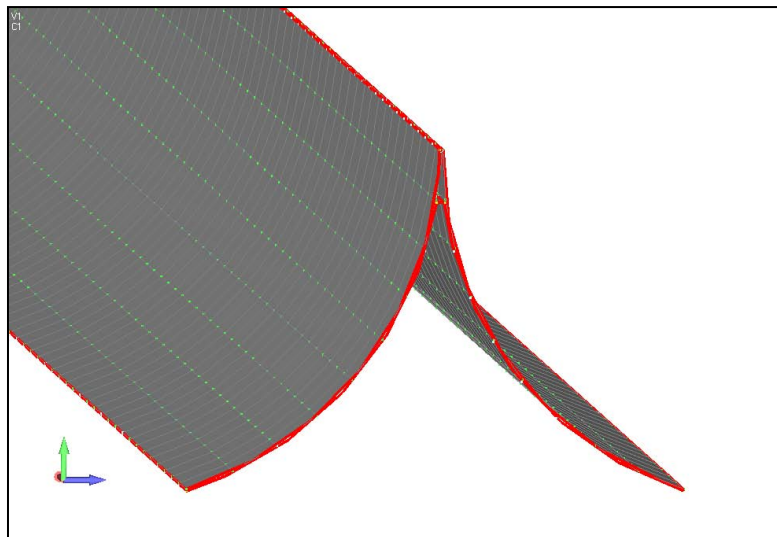
Figure 36. Finite Element Model Cross Section

69

These potential differences between the physical and analytical models will contribute to margin of error between measured and modeled.

3.10 Laser Vibrometer Testing Setup and Data Acquisition

The frequency testing conducted on the TRAC boom geometry sought to explore and quantify the behavior of the booms at multiple frequencies as designed. If the input-output behavior of the boom were known at all frequencies, problematic frequencies could be avoided, compensated for, or exploited as needed.

In order to minimize the effect of gravity the beams were mounted vertically. Clearly, even in this orientation the constant gravitational force is still present as a restorative force. However, the benefit to this orientation resides in the symmetric nature of its application as opposed to the asymmetric loading that would be present in a horizontal beam testing orientation. With a moment arm of zero, the torque applied to the beam in the vertical testing orientation due to the force of gravity is zero. As the boom displaces and oscillates about its central axis, gravity applies a moment to restore the beam to a neutral orientation on both sides of the central axis equally depending on the boom position with effects that are neglected. In a horizontal orientation however, the beam would sag statically unlike the actual deployed orientation in space, where the effective gravity is minimal. In addition, air drag effects were also assumed to be minimal. Vacuum testing of such a large structure was impractical with the promise of little additional insight into the gross modal dynamics, frequencies, or order of their occurrence.

The test stand itself needed to hold the boom rigidly in place at a vertical distance of slightly higher than 4m from the ground. Aluminum 8020, being both in plentiful supply close at hand and sufficiently rigid for our application, was used to construct an apparatus to hold the beam vertically as in

Figure 37. The resultant structure was then anchored to the top of the cinder block lab wall with eight large lag screws providing a rigid base as depicted in Figure 38 and Figure 39.
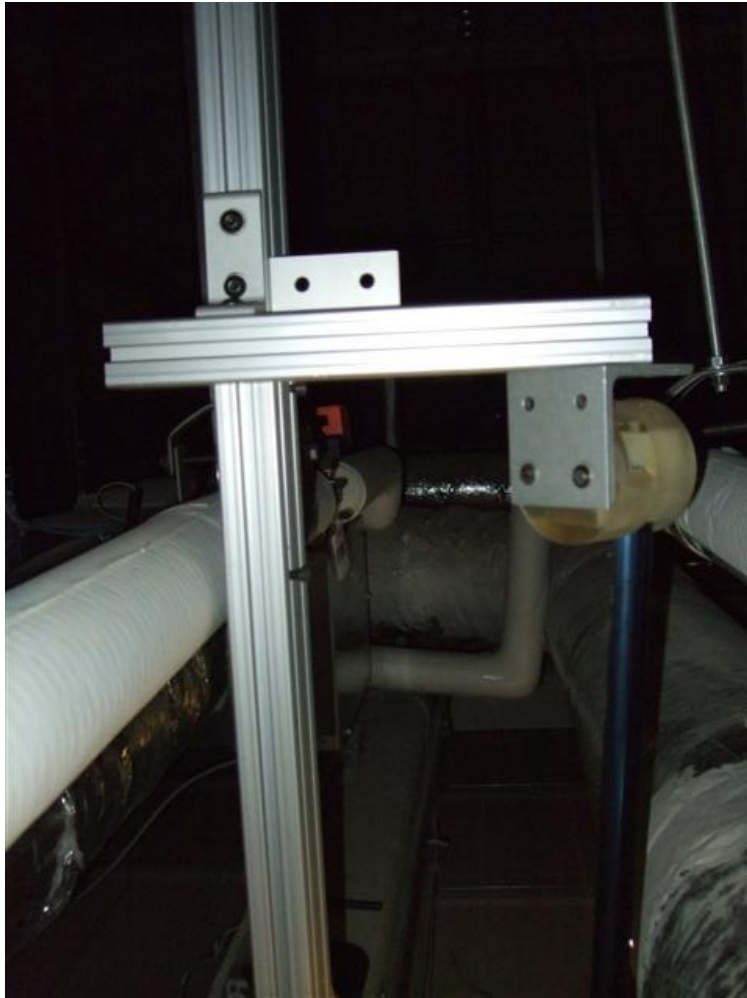
Figure 37. Laser Vibrometer Test Stand

Figure 38. Test Stand Wall Attachment

Figure 39. Test Stand Wall Attachment Alternate View

Rapid prototype material was used to fabricate blocks which would hold the boom

in place within the hub assembly as shown in Figure 40.   Friction alone proved sufficient

to hold the boom rigidly in place.   The boom was then inserted into an early prototype of

the hub as shown in Figure 41. The entire hub assembly with the boom attached was

connected to an L-bracket with screws and fixed to the test stand as in Figure 42.

Notably the beam was turned 45 degrees to face a single tapespring towards the laser

where the greatest chance of favorable laser signal return was anticipated.

Figure 40. Friction Fit Block on Boom
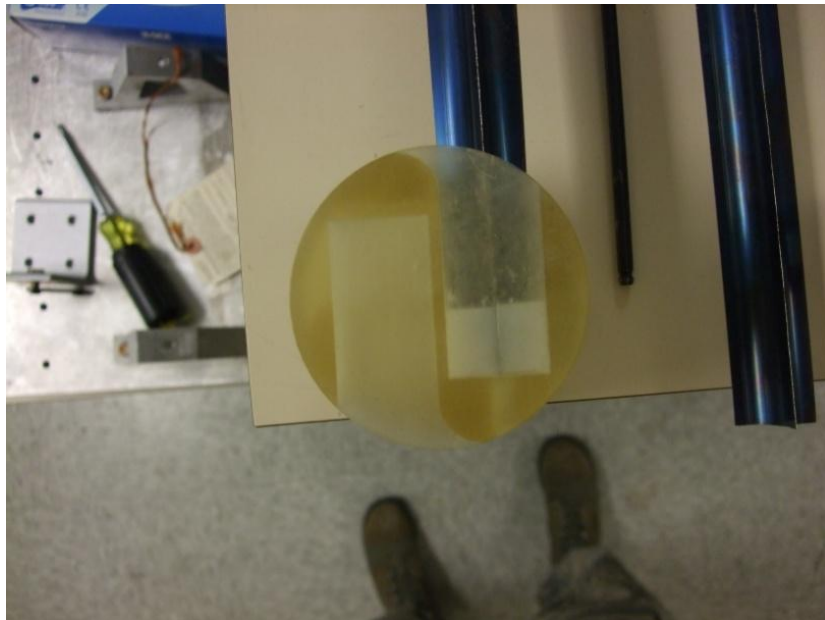
Figure 41. Boom Friction Fit within the Hub

Figure 42. Hub Attachment to Test Stand

Since mode shapes, not merely modal frequencies, were desired, the Polytech

Scanning Laser Vibrometer was assumed to be the optimal tool for analysis. The

automated scanning function of the vibrometer allows the user to scan a grid-like array of

points across the structure. Additionally, the 3-laser heads facilitate measurements in all

three dimensions. The deflection shapes gathered by the Polytech software are then

processed by the MEScope Software developed by Vibetech to generate the actual mode

shape shapes for modal analysis. However, the shape of the booms and the specific goals

of this experiment demonstrated that the multi-head scanning laser vibrometer and

software package approach effectively employed in other conventional vibration analysis

problems were, in this case, counterproductive.

The crux of the testing difficulties lay in two unique aspects of the booms

themselves, namely: their structural shape and the frequencies of interest.   The beam is

exceptionally long along the y-direction, relatively thin in the x-direction, with the

springs themselves being unusually shallow in the z-direction. In order to orient the beam vertically it was necessary to remove ceiling tiles and attach the beam high above the apparent ceiling. This placement effectively prevented measurements over the entire length of the beam. Had more ceiling tiles and ductwork been rerouted, the entire beam would still not have been able to be measured with the triple-head laser. The laser velocity measurements are only valid to within 10 degree of the sensor head itself (Polytec, 2007). In order to capture the velocities of the entire beam from tip to fixed end at a fixed head position, the sensor head would have to be placed 11.6m (38.1 ft) away, which was not possible with the available laboratory setup as shown in Figure 43. Otherwise the beam motion could be obtained in multiple measurements sections and later stitched together to obtain the capture the full beam; however time intensive calibrations would have to be taken at each new position of the three laser heads.
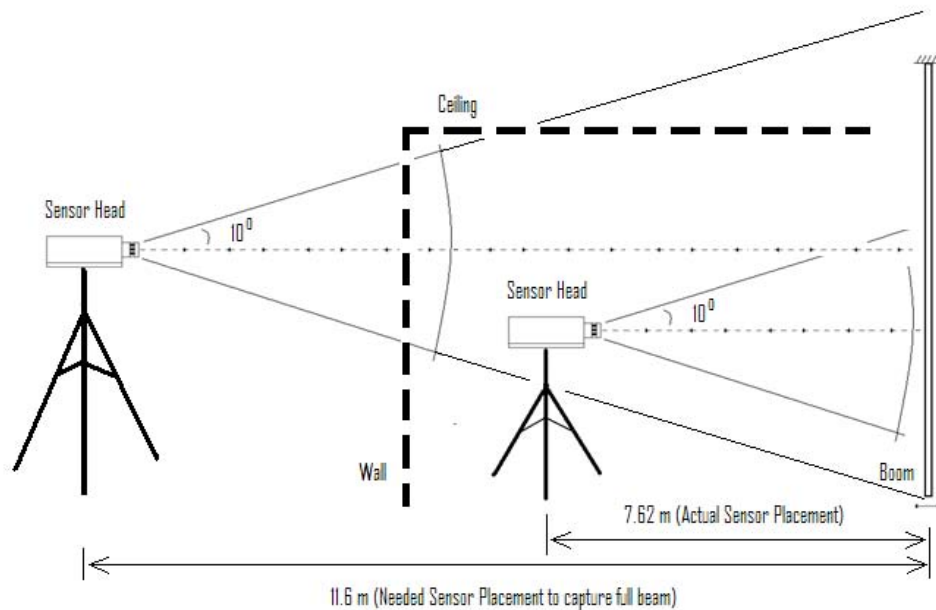
Figure 43. Depiction of Laser Vibrometer Measurement Scope Limitation

Consequently, placing the laser vibrometer at the back wall allowed a scan of the bottom 2/3 of the beam with nearly a quarter of the measurements being questionable taking place at or just exceeding the recommended extents of the Polytec System. The green calibration test article was positioned near the vertical center of the measureable boom as in Figure 44 to minimize the amount of laser points at the limits of the measurement system.

Figure 44. Polytec Laser Calibration Article Position

Although the moment of inertia along the most compliant axis of the TRAC boom is significantly higher relative to that of other collapsible boom cross sections, it is still quantitatively low compared to other conventional non-deployable booms. In practice this equates to exceptionally low frequency excitations which are difficult to capture with decent coherence. The thin flexible structure resonated at extremely low ambient frequencies meaning that normally inconsequential lab noise and air conditioning currents caused a larger denominator in the signal to noise ratio. Normally, such

vibrations, which are always present, are dominated by the signal input after excitation; however, as the beam was particularly susceptible to ambient vibrations, larger than normal excitation levels were required.

The single head laser was used to obtain the frequency response function for a total of 24 points along the beam located at position shown by the Matlab plot shown in Figure 45.
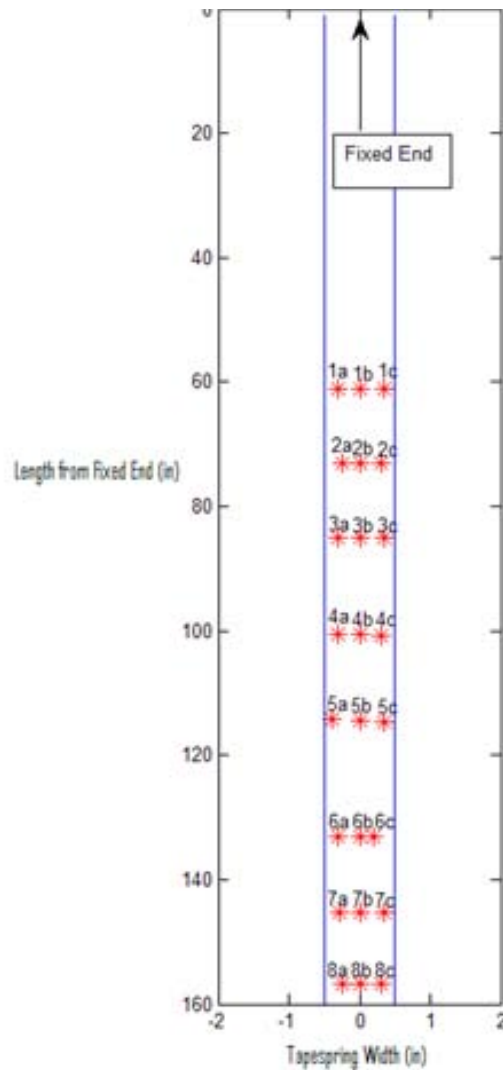

Figure 45. Laser Vibrometer Scan Points

The scanning laser provides three dimensional velocity measurements of each point, but is limited to a fixed height which is only valid for a section of the beam. In addition, calibration issues are of frequent concern. Conversely, the single head laser, while only providing a velocity measurement in a single dimension was easily moved from one location to the next without time consuming calibration. For this application, and level of analysis, the information gathered from the single head laser appears to be more than sufficient. Should three dimensional or entire beam measurement from tip to fixed end be desired using the same lab setup, the single head laser could be positioned in such a fashion as to obtain the results without much adaptation.

Notably, the large displacement levels are not without cost; significant excitations adversely effect all measurements as the linear small angle assumption breaks down. Short of hanging the beam in an evacuated chamber for testing, however, atmospheric drag effects were accepted as an unavoidable source of potential error. A total of five excitation sources were used to vibrate the beam, with all but one providing insufficient performance. Since the frequencies of interest were quite low, functional excitation levels limited the selection of vibrational input sources to piezoelectric shakers, piezoelectric patches, a large speaker, an input hammer, and an electromagnet depicted in Figure 46.
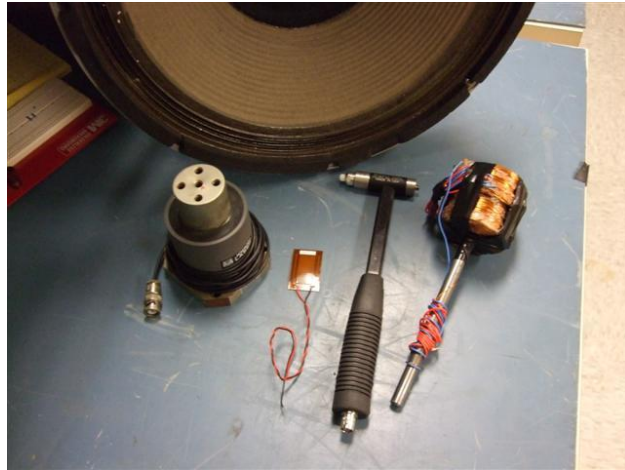
Figure 46. Excitation Sources (From Left to Right): Piezoelectric Shaker, Piezoelectric patch, Impulse hammer, Electromagnet, Speaker (background)

Initially it was thought that a piezoelectric shaker mounted transversely on the test stand would provide the necessary input, however, the input was imperceptible above noise levels with the introduction of a new potential problem with later model comparison. By shaking the beam indirectly, all measurements taken would be of the combined stand/boom system, not merely the boom itself. The difference could be negligible, but presented enough doubt that, when combined with the ineffective actuation of the shaker, made the pursuit of other possible alternatives necessary.
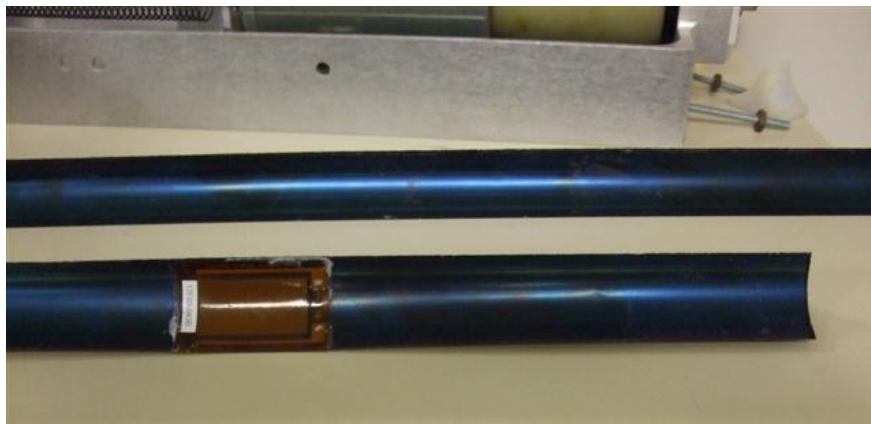
Figure 47. Piezo Patch Location and Orientation

Next, a piezoelectric patch was adhered near the end of the beam as in Figure 47 which was friction fit into the hub. The piezoelectric patch appeared to function sufficiently for a time providing acceptable coherence levels for the beam at frequencies at or above 25 Hz as in Figure 48. It was thought, the poor coherence levels at the lower frequencies would be the best that were attainable.
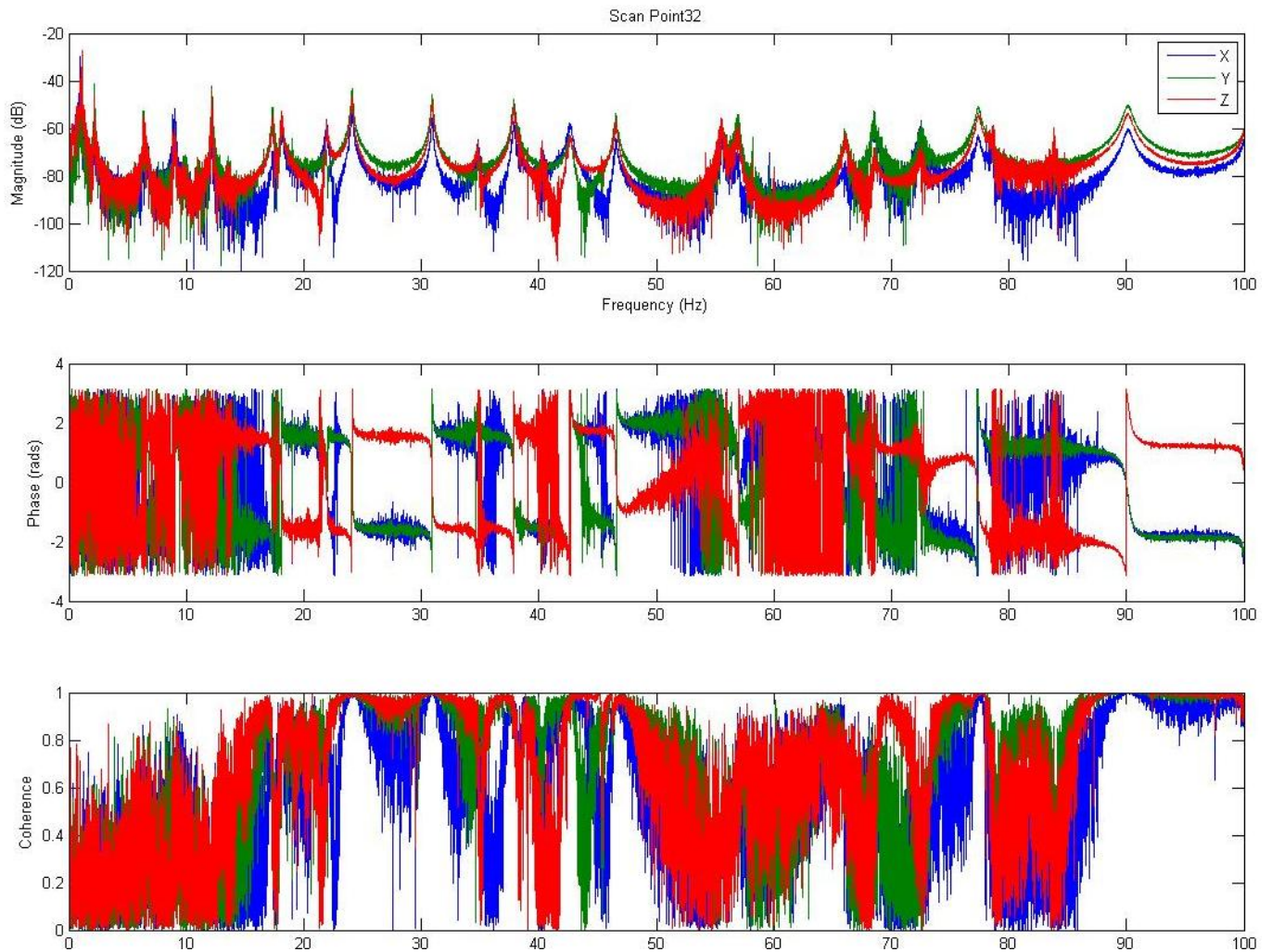
Figure 48. FRF Obtained Using a Piezo-Electric Patch

Additionally, the coherence levels will drop drastically at each natural frequency as the output to input ratio dramatically decreases; as such, even data with poor coherence can provide insight into the natural frequencies of the system. If mode shapes are required however, coherence levels above 0.8 are necessary to reasonably determine the phase of each measurement location. Therefore, in the search for better coherence at low frequencies the search for different input sources lead elsewhere. Both a speaker and modally-tuned impact hammer were used to provide similar results as that of the patch; failing to excite the beam at low frequencies with sufficient coherence to provide any relevant determination of the low frequency mode shapes. The speaker was unable to give the sub 1 Hz excitation necessary, while the hammer was difficult to strike consistently; even the best strikes still did not produce a desirable coherence at the frequencies of interest. Success was found, however, in the careful adaptation of an electromagnet positioned near enough to the beam so as to attract it without causing the beam to contact the magnet itself as in Figure 49.

Figure 49. Electromagnet Excitation Source

The electromagnet was simply a steel rod wrapped with copper wire placed near the beam approximately one meter from the free end. A chirp signal ranging from 0 to 25 Hz was generated and powered by an amplifier through the copper coils. The resultant pulsating magnetic field attracted the non-magnetized steel tapespring beam with a significant amount of beam excitation. The frequency response function was averaged over 10 excitation sequences and a Hanning window was applied to minimize aliasing. The resultant frequency response function had coherence levels still far from ideal but much better in the lower frequencies than those achieved thus far as shown in Figure 50.
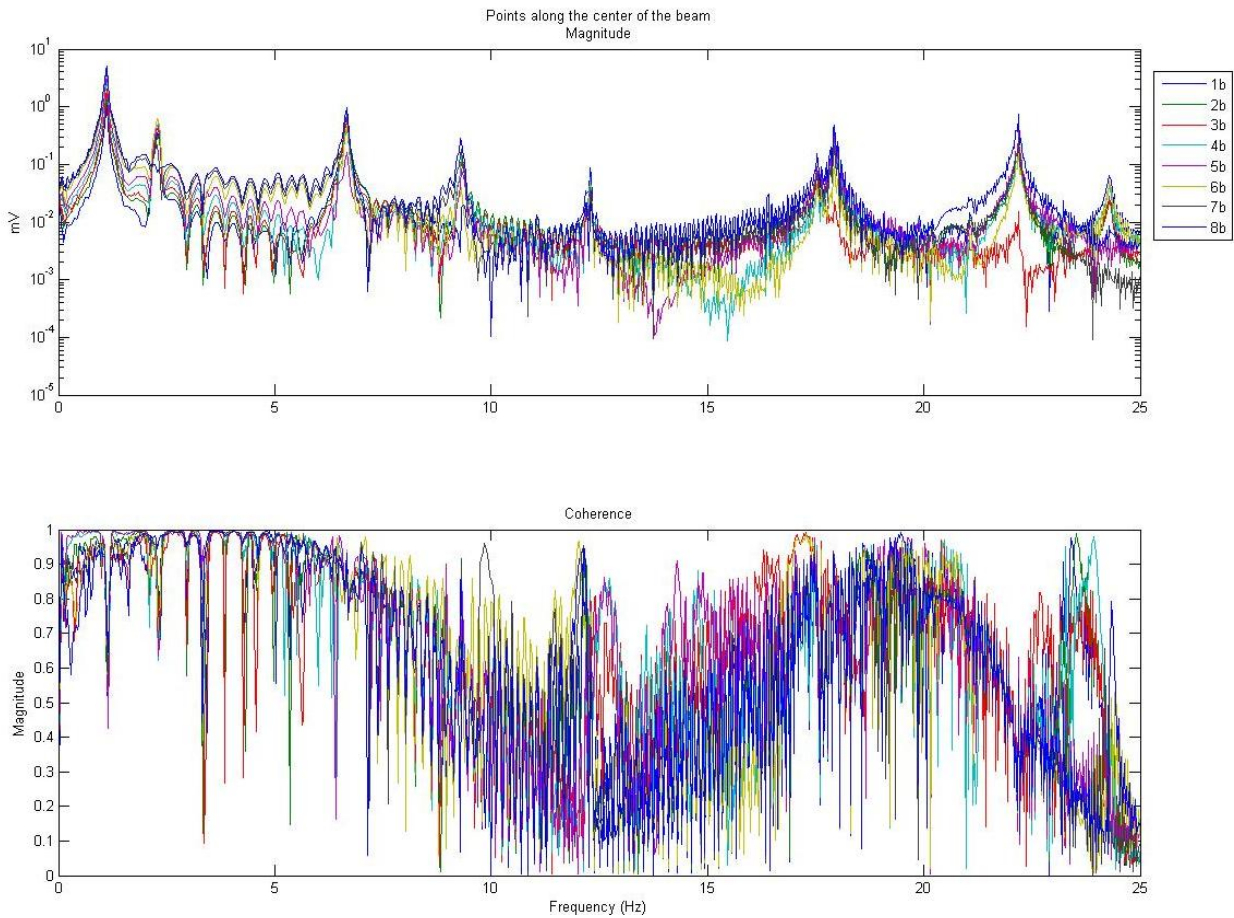
Figure 50. Electromagnet FRF Magnitude and Coherence data

Using the electromagnet as an excitation source, there was a distinct frequency band of acceptable coherence. Notably, the only region of acceptable coherence was from 0 to 7 Hz. However, due to the flexible nature of the beam and the low frequency modal dominance, these frequencies are of the most interest. Mode shapes were obtained from regions of more dubious coherence values such as mode 4 at 9 Hz; however, as will be acknowledged and discussed later in Chapter 5, this could be a potential source of error.

Another phenomenon that was only manifested when using the electromagnet as an excitation source was that of data scalloping between the natural frequencies as in Figure 51.

Figure 51. FRF for Scan Point 1b Excited with the Electromagnet

Scalloping could be the result of a time delay between excitation and the reference signal measurement, but more likely is an artifact of the somewhat nebulous excitation method of the magnetic field. The magnetic field itself was never measured quantitatively, and coherence was determined by comparing the input voltage to the laser-measured output vibrational response of the beam. Perhaps a magnetized beam would respond differently to the current directionality than the non-magnetized beam. The efficacy of the one-way excitation method of the beam due to the attraction of the magnetic field is an area that merits further investigation. However, as of yet, one can only speculate that the cause of the scalloping 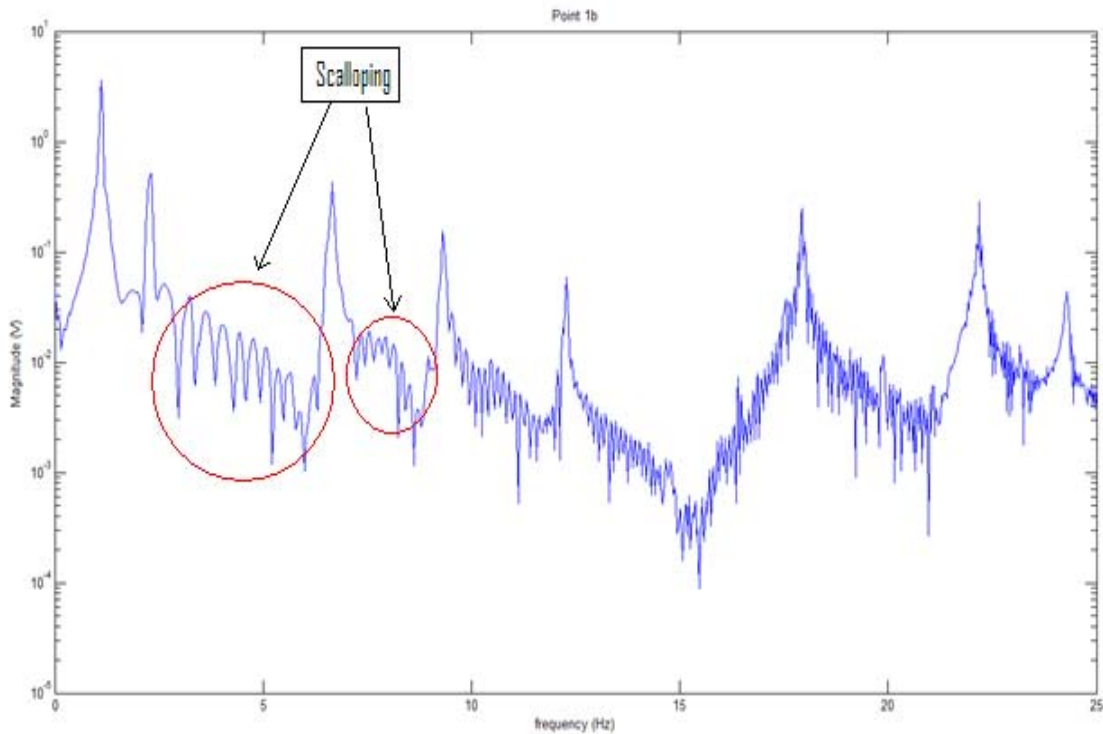must involve electromagnet excitation method as neither the shaker, nor hammer, nor the piezoelectric patch manifested any type of scalloping despite the poor coherence values obtained. The scalloping effect is a major factor in the overall untidy appearance of the data plots themselves particular that of the phase as in Figure 52. However, the magnitude scale is, in fact, logarithmic which implies that the scalloping effects, while appearing quite large, are nearly two orders of magnitude smaller than the magnitude of the natural frequency values. The net result is that while the frequency response data obtained from the electromagnet source excitation of the beam appears scalloped and ugly, it is still quite useful for SLiMSat beam analysis.

Clearly the phases at all points in Figure 52 are changing in unison, however the anti-resonances which are an artifact of the data scalloping causes an inordinate amount of phase swapping from +180° to -180° clearly seen below 5 Hz.

Although the data across all frequencies appears unruly, it is only necessary that the coherence approach an acceptable level in the bandwidth of interest. If the coherence is suitable, then the respective magnitude and phase data can be adapted to form an eigenvector, which can later be modeled as a mode shape.
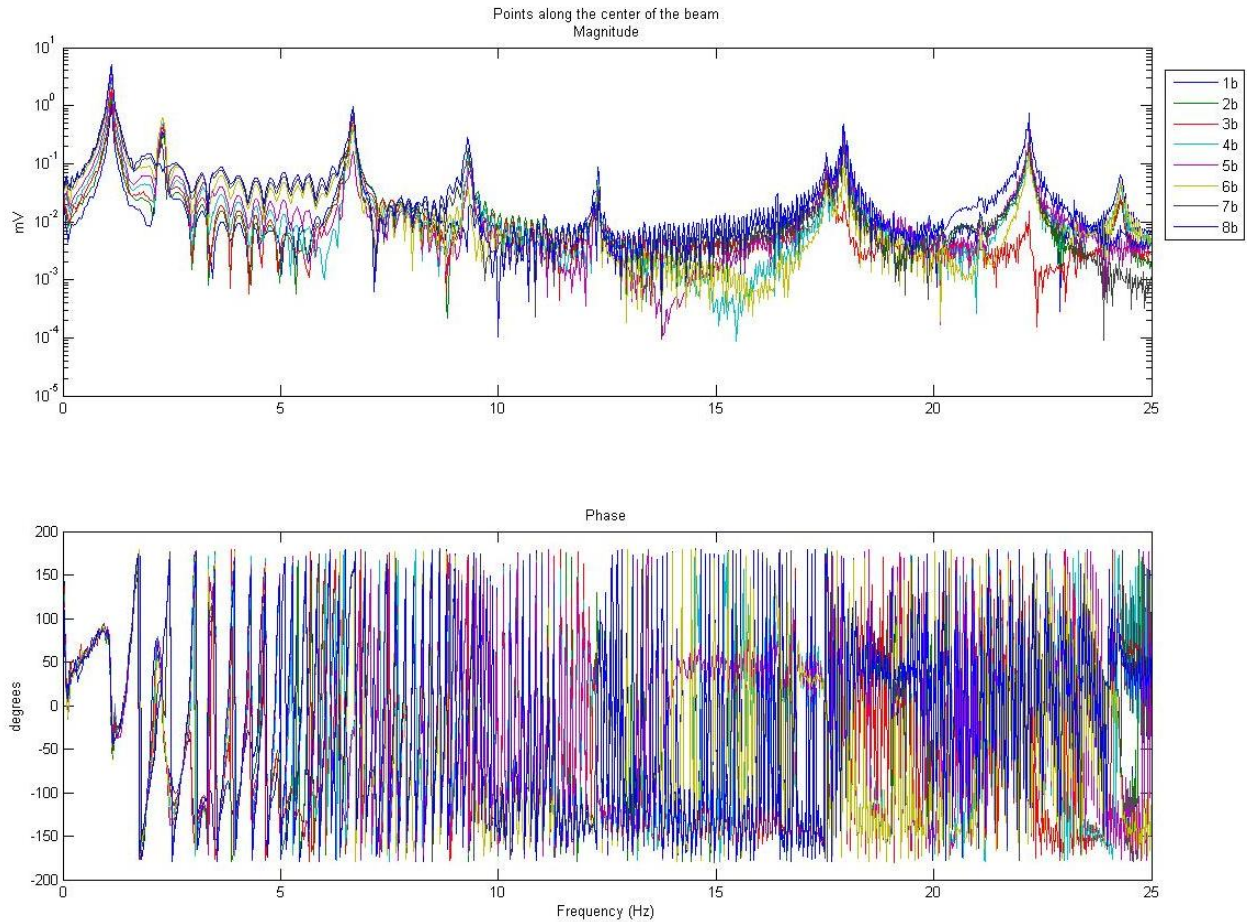

Figure 52. Data Scalloping Effects on FRF Phase Data

3.11 Summary of Methodology

The vibrational tests outlined in this chapter should provide an adequate foundation for future testing as well as give some insight into beam performance and the difficulties in obtaining acceptable data from such a unique structure.

85

IV. Analysis and Results

4.1 Chapter Overview

The ultimate goal of the testing conducted on the booms, the validation of the finite element models of the booms, and the deployment proof of concept demonstrations is to better understand the booms and their integration into the CubeSat space platform. As engineers, this knowledge contributes to better CubeSat designs in the future; as students, the design process achieves multiple objectives. First, the student learns first-hand the basic process of developing a design from an abstract design concept to a physical reality. Second, the basic foundation is laid for future CubeSat collaborators; but perhaps most significantly, the dynamic characterization of the TRAC booms themselves will shed some light on the ambiguous question of their viability and implementation into the AFIT SLiMSat mission.

As a physical structure the booms behaved differently at different excitation frequencies. Useful data was measured using the Modal Analysis theory of Chapter III along with the Vibrational Test Setup of Chapter IV. What was desired was the modal behavior of the boom at particular frequencies. That behavior could later then be exploited or circumvented through by stiffening the structure or applying some sort of damping to the beams themselves. However, not much was known quantitatively about the booms at this point and it is to this end that the extent of the experimental focus was directed. As has been previously mentioned, the FRFs utilizing the electromagnet as an excitation source provided data with the highest coherence at frequencies of below 5 Hz.

It was essential to capture the low frequency responses of the beam as these were the dominant frequencies of greatest interest and, as such, the most important mode shapes to accurately model. A model is, by definition, an approximation; wherein it is not feasible to match all modal frequencies exactly. However, by matching the first few modal frequencies and ensuring that the subsequent mode shapes occur in the same order at roughly the same frequency values, we can confirm that our model is of significant correlation in order to draw reasonable conclusions. In a sense, it is the job of the engineer to decide quantitatively when the model is good enough as well as to persuade others that they are right.

4.2 Boom Reciprocity Testing

In order to project and predict the performance of future beams from the current model and prototype it is necessary to establish that the individual beams do not vary from one another. There are, in fact, inherent anomalous defects within any material, much more so when that material is assembled by hand. The booms themselves were constructed from two one inch wide 0.001 in thick pieces of High Carbon Cold Rolled Stanley tape measure steel. The steel was obtained directly from Stanley heat treated but unpainted. The tape measure spring was then laser welded along single long edge to form two four meter boom sections. The laser welding process was understandably difficult as the ultra-thin steel required exceptionally low heat so as not to warp or distort the heat treatment and thus only two sections of beam were produced. Qualitatively, the beams were remarkably straight and uniform; however quantitative tests of those welds were required to determine a notional repeatability for the welds themselves.

87

Presumably, the steel obtained from Stanley was uniform without any major defects and thus any variances among the beams themselves were assumed to come from two distinct sources of error, namely: the fixture method of the beams, or the welds. For each beam, two tests were conducted by fixing one end of the beam in the test stand and conducting a vibrational test; later the same beam was removed from the stand, flipped around and fixed again using the opposite end for a second vibrational test. In this manner, two separate FRFs were generated from an identical beam; the results of which are compared in Table 3 in order to demonstrate baseline linearity among the TRAC beam test articles. With the excitation source position and relative beam position held constant, the only variance between the tests was the fixture method itself; which consisted of three friction fit blocks held together within a test hub as in Figure 41. The results of those frequency response tests are shown for both configurations of Booms 1 and 2 in Figure 53 and Figure 54 respectively. Each boom was 4 m in length and excited through the use of and electromagnet induced chirp cycled from 0 to 25 Hz with the configuration denoting which end was arbitrarily fixed within the test hub. Each test was averaged among ten tests so as to minimize ambient noise effects or anomalies. Ideally, the plots of each boom configuration would lie on top of one another, which would indicate that the friction fit blocks provide a perfectly fixed constraint for the beam to oscillate against.

In the case of Boom 2 in Figure 54, this appears to be a valid assumption; however while Boom 1, in Figure 53, exhibits nearly the same behavior between the configurations, there are clearly more variances than in Boom 2. Perhaps, this difference

88

could be accounted for in the fact that Boom 1 Configuration 1 test was conducted on the

beam after many days, and many failed excitation attempts.
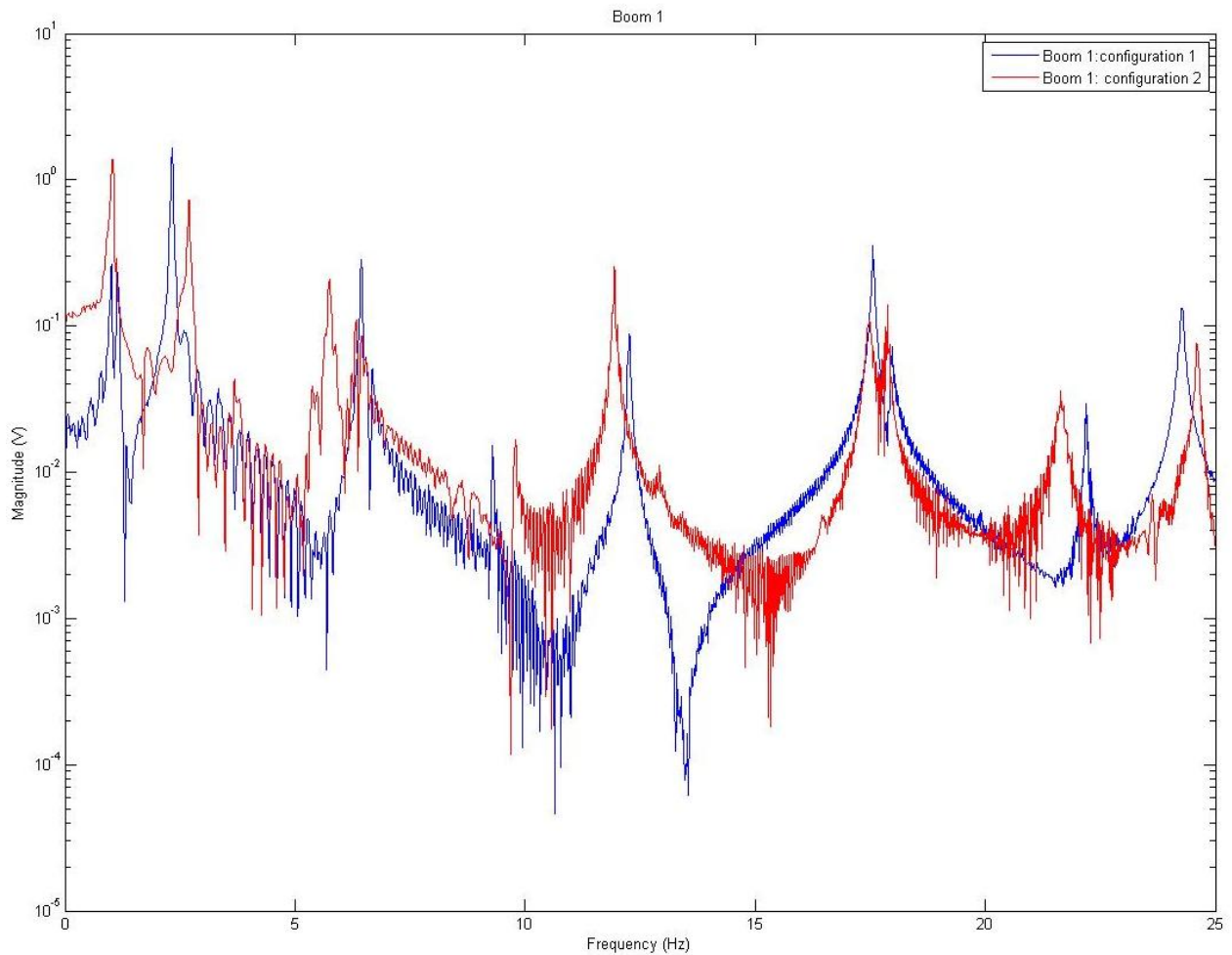
Figure 53. Boom 1 Reciprocity Testing

Perhaps this stress led to a slight loosening of the friction fit blocks and could

account for the pronounced difference. However, when both plots are viewed

simultaneously as in Figure 55, it is clear that the natural frequency do not shift much at

all as might be expected with such an inherently imprecise structure.
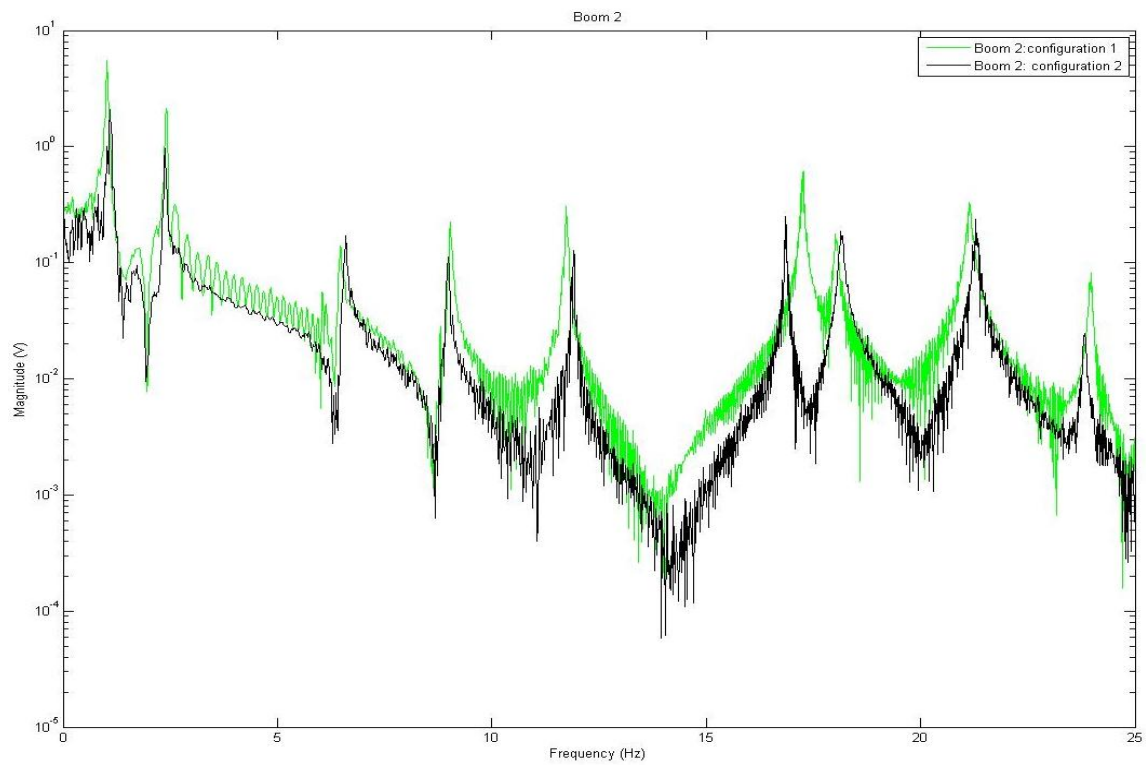
Figure 54. Boom 2 Reciprocity testing
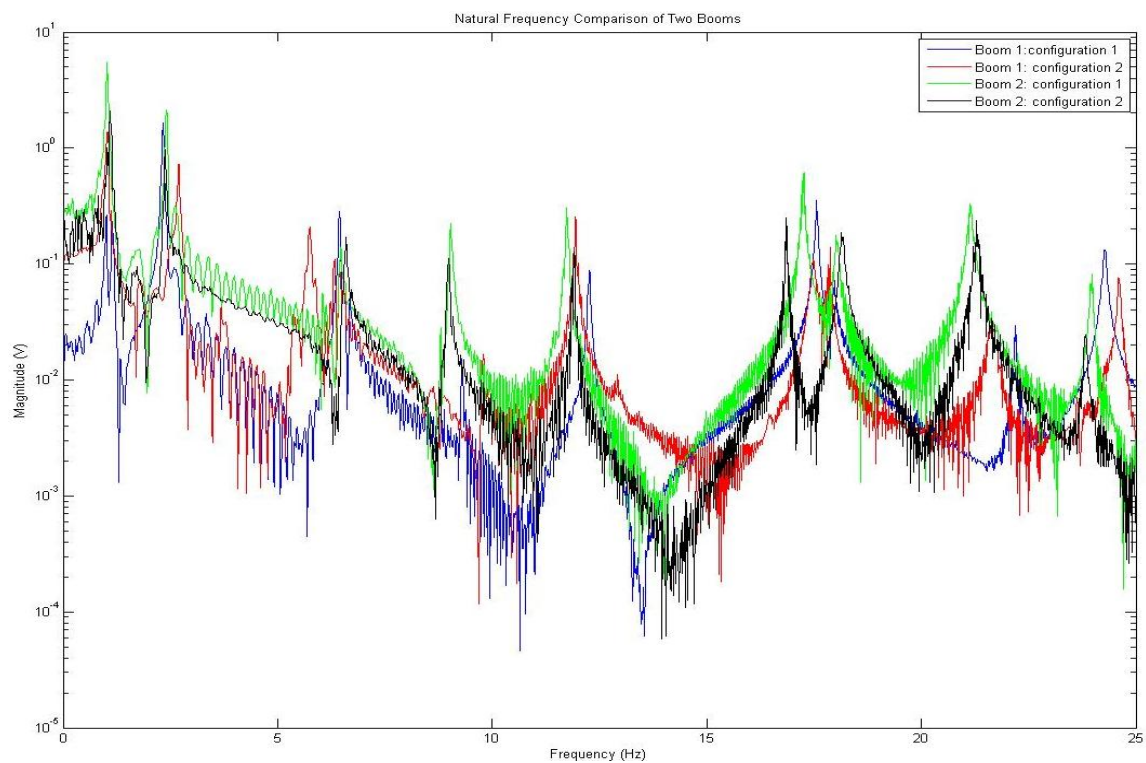
Figure 55. Natural Frequency Comparison of Two Tapespring Booms

Table 3 lists the natural frequency values for each boom and configuration. From those four natural frequency values, each corresponding to different boom and configuration, a standard deviation was calculated for each mode. In the rows labeled "Boom 1 (Config 1/ Config 2)" and "Boom 2 (Config 1/ Config 2)," both configurations for each boom are compared to one another to determine an error value between the configurations at each natural frequency.

Table 3. Boom Comparison for Reciprocity Analysis

| Natural Frequency (Hz)	1	2	3	4	5	6	7	8	9
Boom 1: Config 1	1.016	2.328	6.438	9.297	12.27	17.56	17.98	22.19	24.28
Boom 1: Config 2	1.047	2.703	5.75	9.797	11.94	17.48	17.88	21.64	24.59
Boom 2: Config 1	1.031	2.406	6.469	9.031	11.73	17.27	18.02	21.14	23.97
Boom 2: Config 2	1.094	2.375	6.594	8.984	11.91	16.86	18.17	21.28	23.81
Standard deviation	0.0338	0.1697	0.3812	0.3729	0.225	0.3132	0.1204	0.4684	0.3454
Boom 1 Average	1.0315	2.5155	6.094	9.547	12.105	17.52	17.93	21.915	24.435
Boom 2 Average	1.0625	2.3905	6.5315	9.0075	11.82	17.065	18.095	21.21	23.89
Error Difference for Fixture Method									
Boom 1(Config 1/Config 2)	2.96%	13.87%	10.69%	5.10%	2.69%	0.46%	0.56%	2.48%	1.26%
Boom 2 (Config 1/Config 2)	5.76%	1.29%	1.90%	0.52%	1.51%	2.37%	0.83%	0.66%	0.67%
Average	4.36%	7.58%	6.29%	2.81%	2.10%	1.41%	0.69%	1.57%	0.96%
Error difference between Booms									
Boom 1 vs. Boom 2	2.92%	4.97%	6.70%	5.65%	2.35%	2.60%	0.91%	3.22%	2.23%
Total Average Natural Frequency	1.047	2.453	6.31275	9.27725	11.9625	17.2925	18.0125	21.5625	24.1625

The ratios of the natural frequencies for each configuration of the same boom were subtracted from one another to determine the percent difference. These values

should correspond to the error inherent in the friction fit block method. For Boom 1, the error is between 0.5% and nearly 11% depending on the mode as shown in Table 3, "Boom 1 (Config 1/ Config 2)"; while Boom 2 is considerably lower, varying from 0.6% to 6% in the same table, "Boom 2 (Config 1/ Config 2)". The average error difference for the fixture method at each natural frequency was then calculated by taking the mean of the two preceding rows and listed in the row labeled "Average."

In order to determine whether the error associated with this particular fixture method is acceptable, it will be necessary for future groups to conduct tests utilizing a variety of fixture methods. However, for prototype development, this range of error is acceptable.

Next, average natural frequency values were obtained for each boom which considers both configurations of a single boom and incorporates the fixture method variance errors. With the assumption that the actual natural frequencies of each boom lies between the measured values in each configuration, these average values represent the average natural frequencies anticipated for each boom. These natural frequencies are listed for each mode in the rows labeled "Boom1 Average" and "Boom 2 Average".

From the natural frequency averages of each boom, an error difference was calculated by comparing the rows "Boom1 Average" and "Boom 2 Average"; representing the expected reciprocity error incurred from the welding and assembly process. Those errors, listed in the row labeled "Boom 1 vs. Boom 2" vary from 0.9% to 6% depending on the natural frequency of interest. The row labeled "Total Average Natural Frequency" was calculated by taking the average of the first four rows of Table 3.

The last row of Table 3 is also represented graphically in Figure 56 which accounts for both the fixture and fabrication error to produce anticipated natural frequency values for future beams.
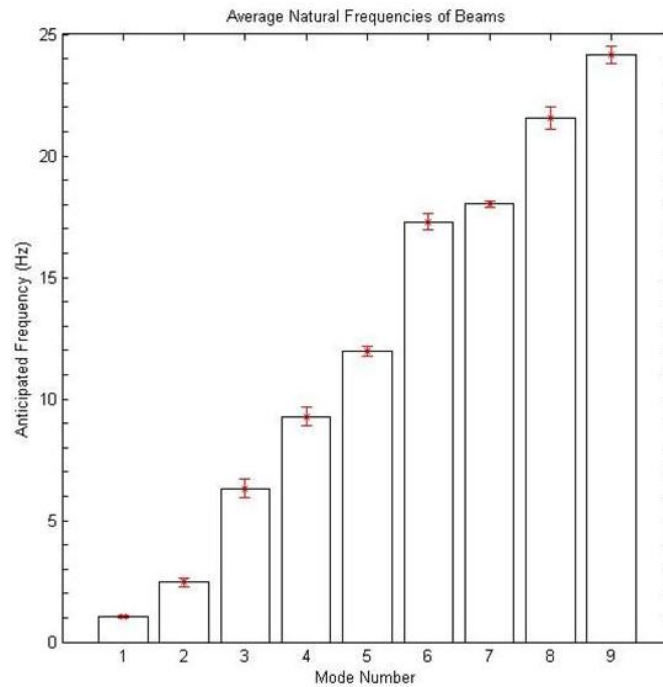

Figure 56. Anticipated Natural Frequencies of Future Beams

More data points would be required to determine conclusively, but it would appear the friction fit method of fixation and the laser welding process are both viable methods of repeatable TRAC beam manufacture for CubeSat applications.

4.3 Mode Shapes from Data

To determine the mode shapes from the gathered frequency data we must compare the relative magnitudes and phases of each scanned data point at the natural frequency of interest. In order to better visualize the frequency response of the beam itself it is helpful to view the response of multiple points along the vertical axis of the

93

beam along the center axis of a single tapespring.   There were a total of 24 scan points

located at the positions specified by Figure 45. Figure 57 represents the FRF plots of all

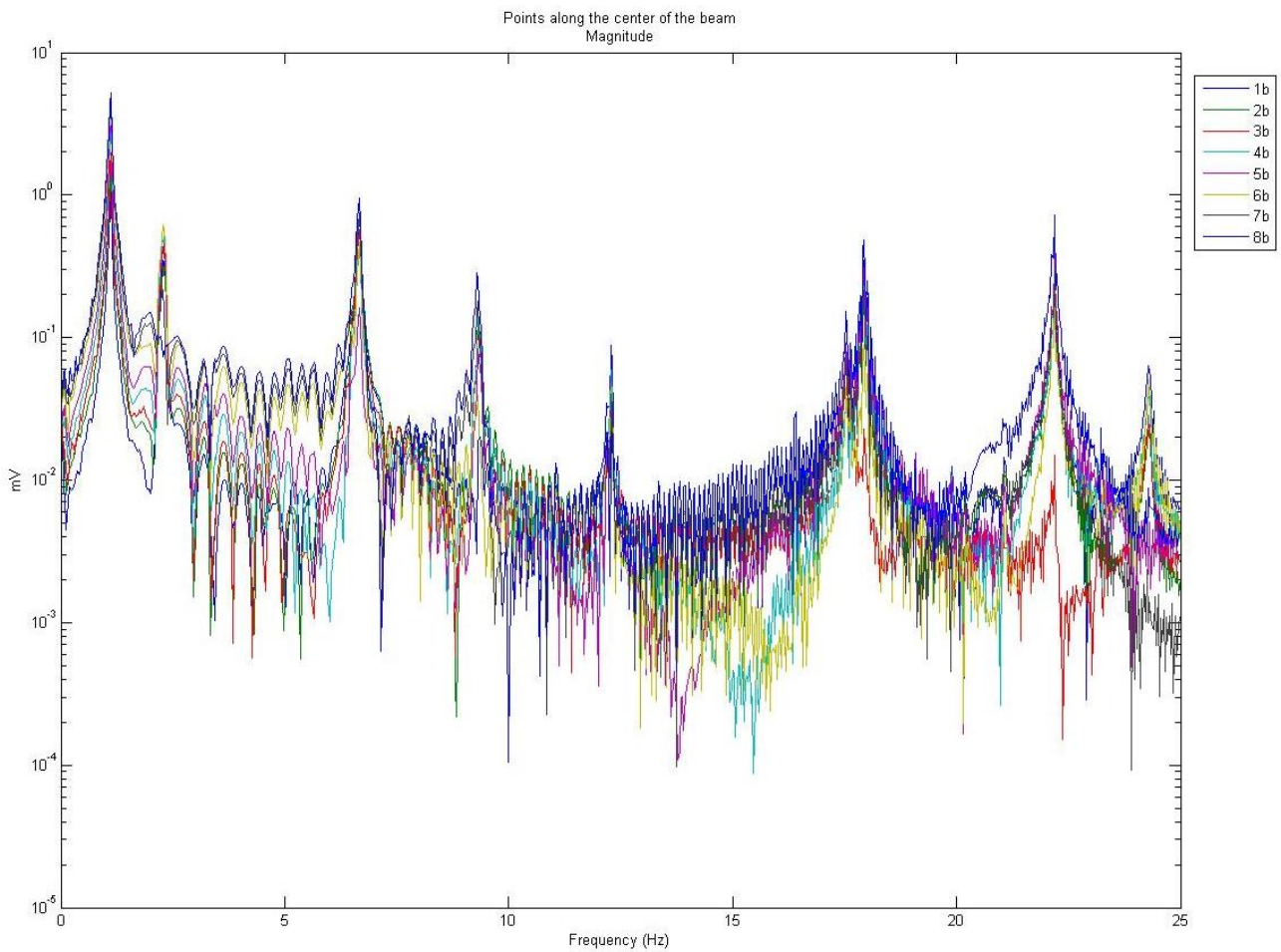the "b" points along the center of the beam.

Figure 57. FRF Magnitude Data from scan points along the center of the beam

The gathered data was grouped in multiple ways so as to facilitate understanding.

Figure 58 is an example of the frequency response magnitude and phase, as well as the
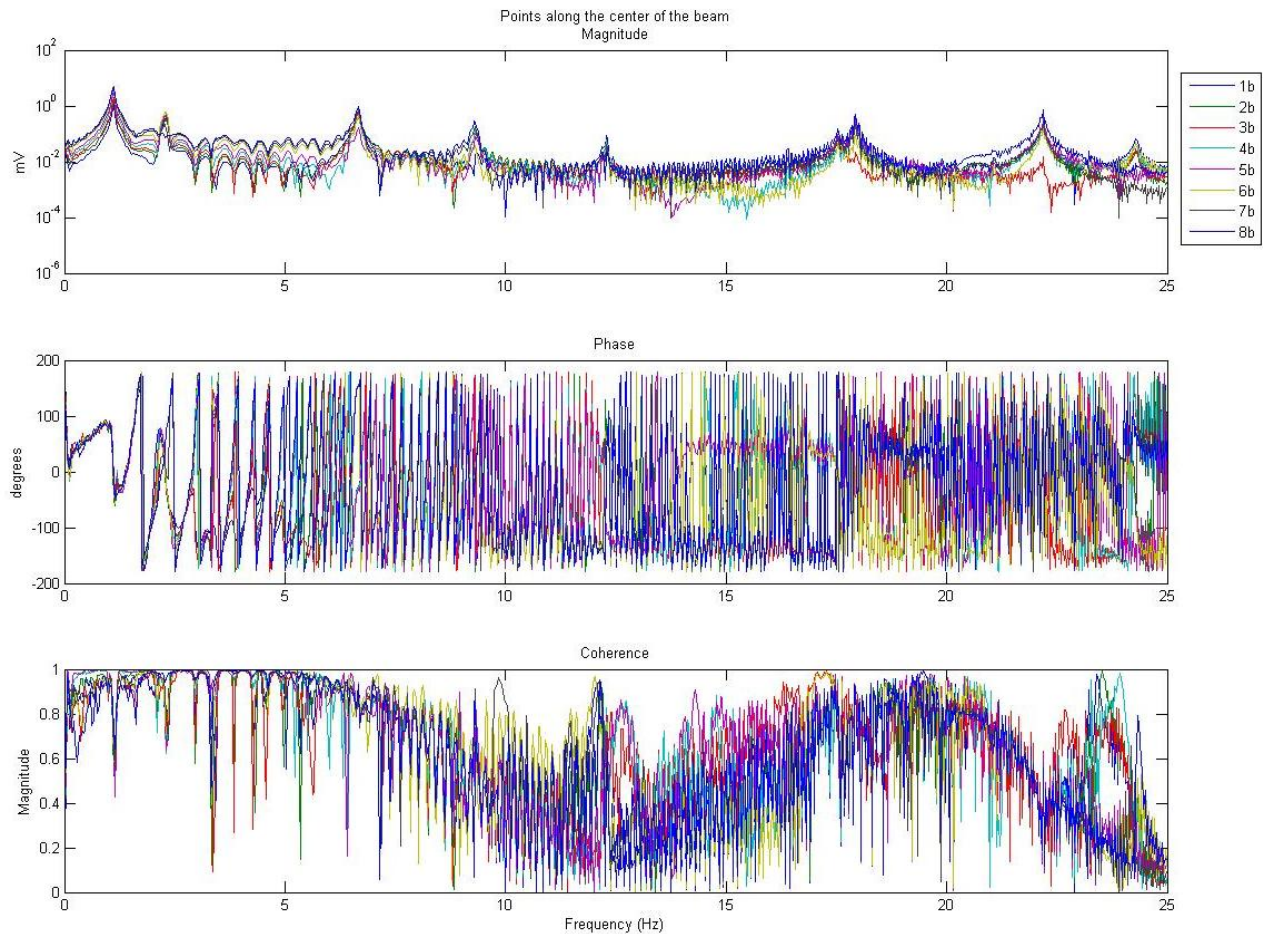
corresponding coherence.

Figure 58. FRF of Center Points along the Beam

The coherence and phase of Figure 58 exhibits the same characteristic scalloping

and phase alternation as has been previously discussed using the electromagnetic

excitation source. The coherence, while particularly noisy, does indicate that mode

shapes below 5 Hz might have been attainable; and is unfortunately, the best current

testing methods would allow. It is also worth noting that it is experimentally impossible

to excite only one mode shape or frequency, all modes are excited at each frequency

which is why the detected frequency response at any given point is called a deflection

shape and not an "eigenvector." However, at each natural frequency a particular

deflection shape is dominant which is loosely termed the "mode shape." For the

95

purposes of the beam analysis presented here, the "deflection shape" is considered for all practical purposes to be the "mode shape." For our rudimentary analysis, this appropriation is acceptable, however it should be noted that this is indeed a loose application of terms.

In order to determine an eigenvector at a particular modal frequency it is necessary to first determine the natural frequencies of interest and then relate the magnitudes of each scan point at that natural frequency. Relative magnitudes are easily determined as depicted in Figure 59. At 1.125 Hz the relative magnitude displacements of each scan point along the center of the beam is clearly seen.
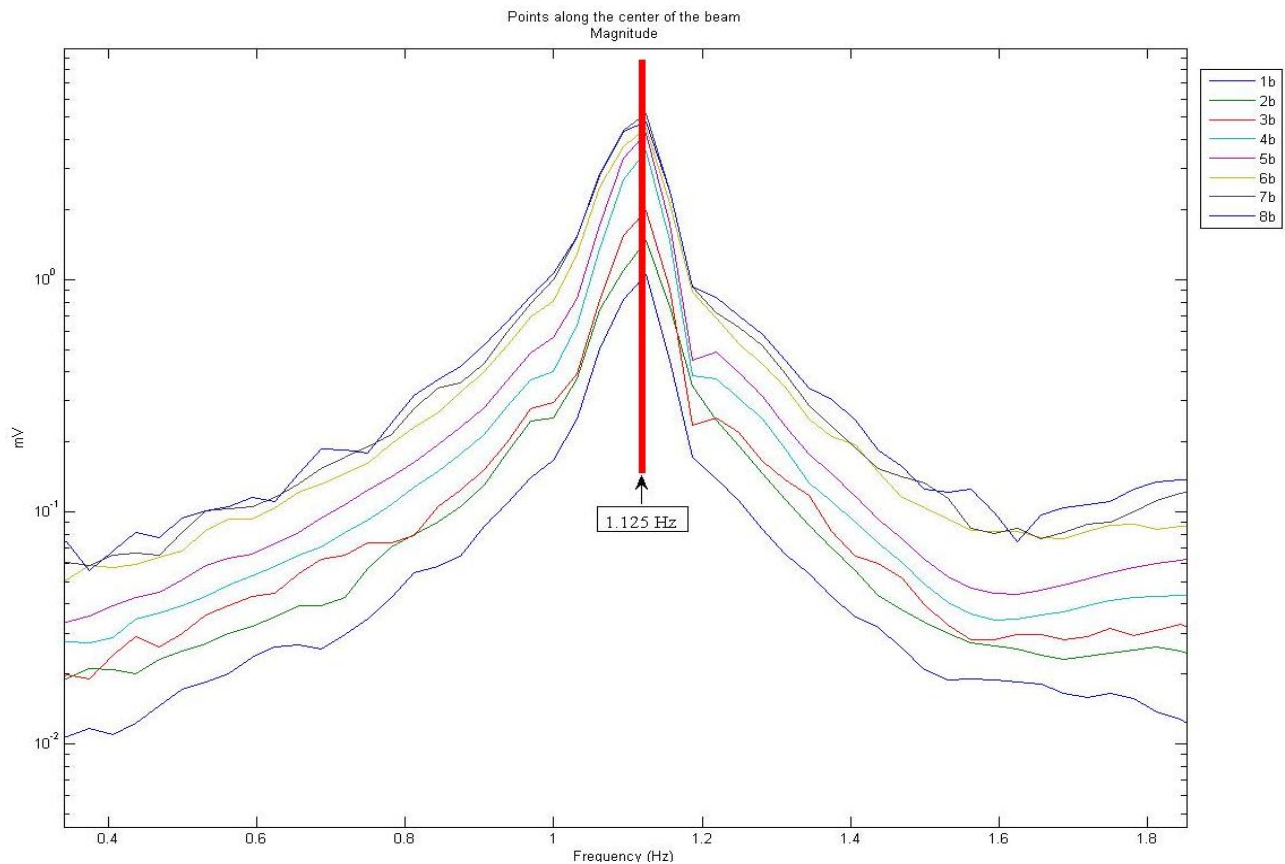

Figure 59. Relative Magnitudes of Scan points at the First Natural Frequency

96

In the interest of brevity, the data gathered for each scan point is not displayed here as all the modes of interest are adequately depicted. Nine modes of interest were measured below 25 Hz, which is characteristic of a thin flexible structure such as that of the booms. The FRF plot for each point is located in the Appendix however, should future analysis warrant more data. The phase data can then be used to determine the sign of the magnitude points in relationship with one another. This technique is only acceptable as eigenvectors are scaled by an arbitrary constant; hence the exact magnitude values of each scan point only matters in relationship to the others.

Ideally, when plotted in the complex plane the all the scanned data points of the eigenvector would appear along a straight line through the origin rotated about some arbitrary angle. The reason for this apparent happenstance lies in the nature of the eigenvector itself. Points along a single line in the complex plane represent points that all have exactly the same phase or antiphase of one another. The unison of these phase angles is precisely the cause of the natural frequency itself. Hence, as the real and imaginary portions of the response are plotted at a particular natural frequency, large deviations from that ideal eigenvector line would indicate a lack of data quality. Figure 60 is the complex plot of Mode 1, which, unfortunately, does not possess the desired tight data grouping.
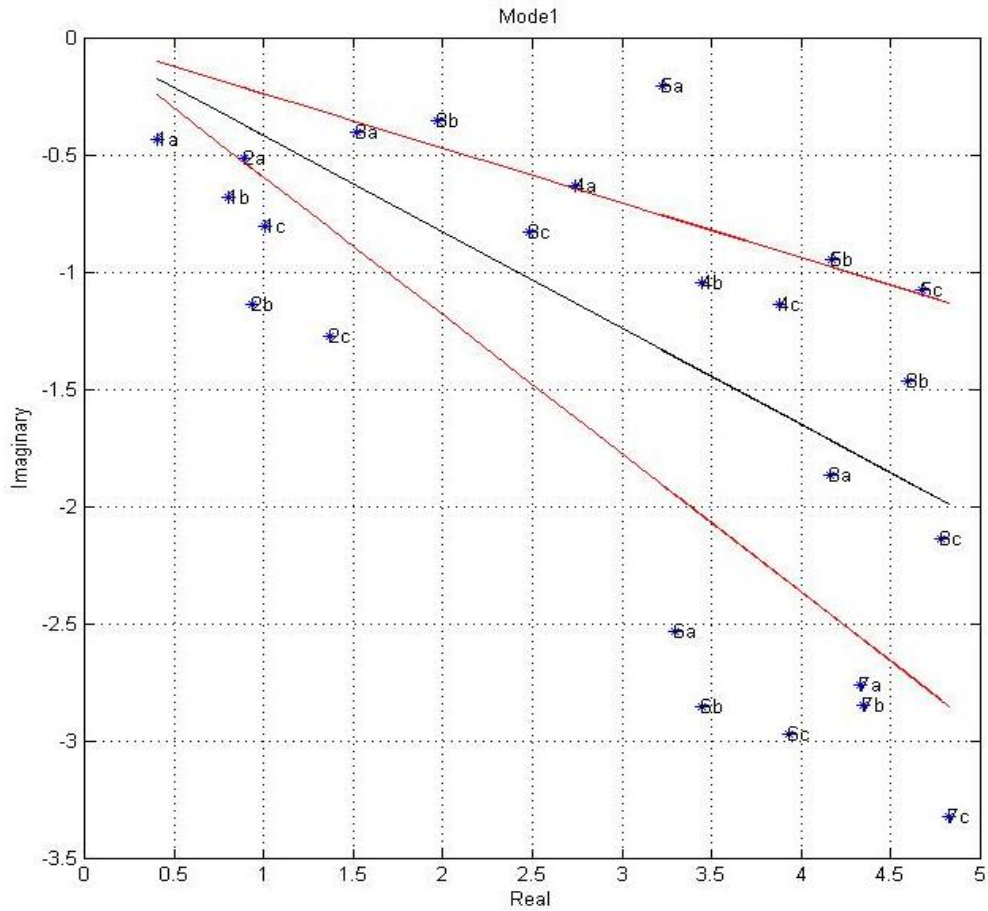
Figure 60. Mode 1 Eigenvector Complex Plane Plot

The eigenvector spread is due to the dominance of this particular mode in terms of

gross motion of the beam. Referring back to Figure 57, it is clear that the magnitude of

Mode 1 is an order of magnitude above all other natural frequencies of interest. In order

to excite the higher modes up to a detectable level, the linear motion assumption for

Mode 1 bordered on the acceptable limit. However, while the eigenvector plotted for

Mode 1 might not be ideal, the data is still usable as the majority of points lie within a

tolerable limit. The central black line is the ideal eigenvector line and the red lines

represent +1 and -1 the standard deviation of the mean phase of the data points

themselves. Inherent in this estimation of eigenvector deviation is that of the points of

98

the largest magnitude were ostensibly assumed to have the largest signal to noise ratio, and therefore be the highest quality of the bunch. In order not to skew the calculated deviation from the mean phase by these potential outliers, a weighted average algorithm was employed in order to preserve the phase dominance of the points with the largest velocities. Notably, accurate phase measurements become increasingly difficult as the magnitude of their displacements decreases. The points that lie farthest radially away from the origin represent points of the greatest magnitude; which agree with intuition and correspond to the scan points located farthest away from the fixed end of the beam, namely points 8a, 8b, and 8c.
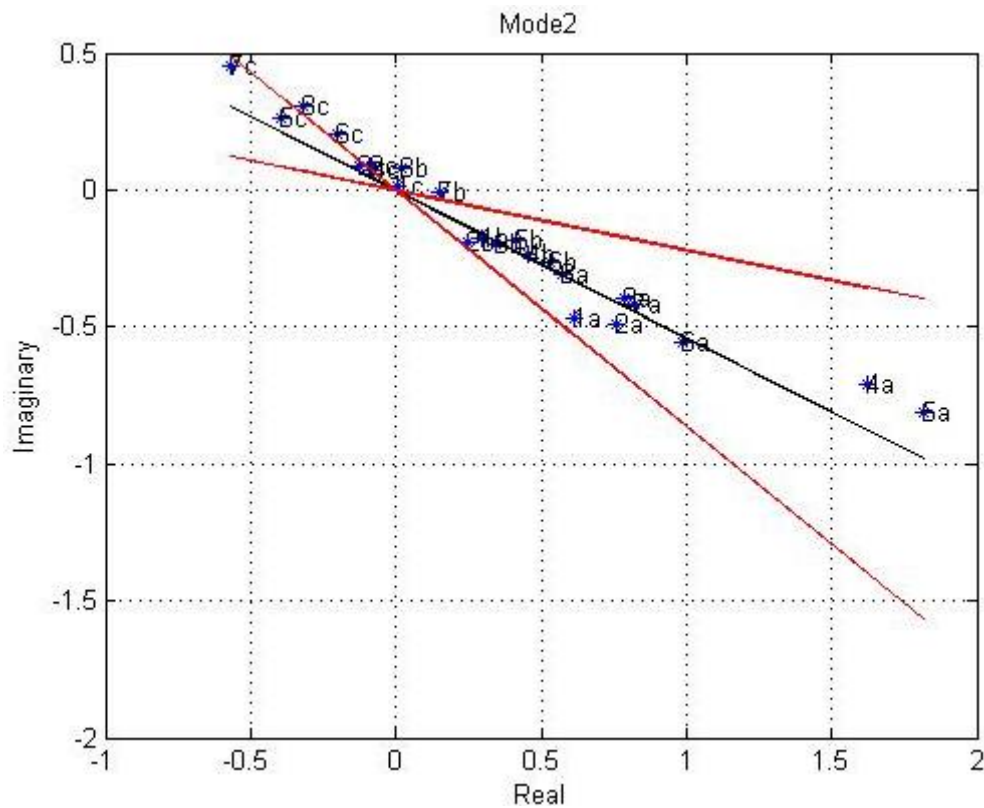

Figure 61. Mode 2 Eigenvector Complex Plane Plot

Mode 2 clearly has more desirable eigenvector data as nearly every scan point is bounded by the standard deviation bracketed lines indicating a definitive capture of that modal shape and frequency.
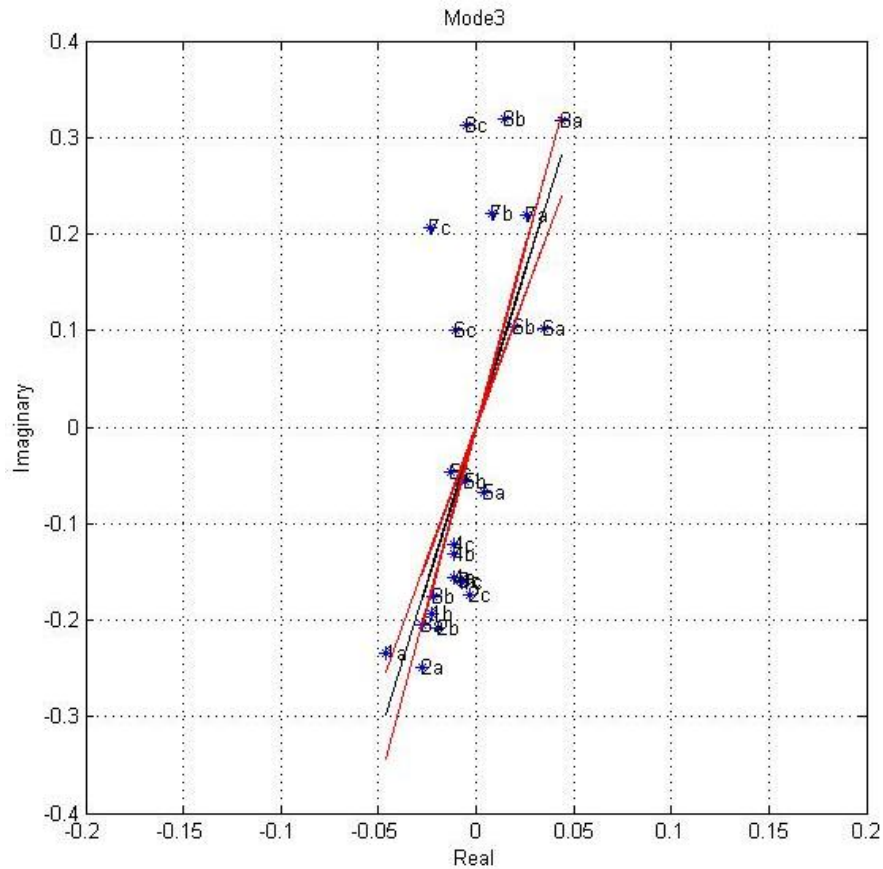
Figure 62. Mode 3 Complex Plane Eigenvector Plot

Mode 3 once again posses scan points moving in and out of phase with one another. One can also detect that the points farther away from the origin are located at the extents of the test section of the beam, with points 5 and 6 possessing the smallest magnitude relative velocities.

Determining the sign of the individual components of the eigenvector is not trivial, even for a mere 24 scan points as in this model of the tapespring beam. By

examining the complex plots of the magnitude and phase data as in Figure 60, it is apparent that every point is moving in phase with the others and consequently every component of the eigenvector should have the same sign. Taking a projection of the data points onto the real axis and applying a simple algorithm where positive values have would the opposite sign of the negative values, would produce correct eigenvector in this instance. However, examining Mode 3 in Figure 62 it is clear that a mere projection onto the real axis, would apply opposite signs to points that should be in phase with one another. In order to avoid this potential misapplication of signs, a simple algorithm was employed in Matlab. The entire eigenvector was rotated so that its magnitude components are on either side of the imaginary axis. To accomplish the rotation a "factor" was added to each phase magnitude component in order to rotate the arcs of the phases (of unit magnitude) to be centered on +1 and -1 on a polar plot. The factor is calculated in two parts: first the magnitude of rotation is determined, and second the direction of that rotation is applied so as to rotate the arcs as shown in Figure 63.
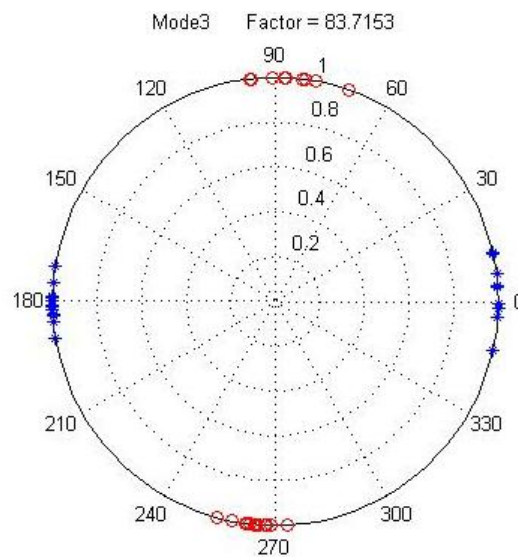

Figure 63. Mode 3 Polar Eigenvector Plot with Scan Points of Unit Magnitude

101

The red circles indicate the eigenvector scan points prior to the application of the phase magnitude factor; the blue asterisks represent those same points as they are rotated so that the average value resides on the real axis. Using the "factor" algorithm ensures that neither the phase arc spread nor the arbitrary rotation of the complex eigenvector line will adversely affect the sign applied to the FRF magnitude data.

4.4 Modal Assurance Criterion

The Modal Assurance Criterion (MAC) is an algorithm which can help determine which theoretical mode shapes correspond with which experimental ones (Vandawaker, Palazotto, & Cobb, April 2007). The full 4m boom was unfortunately not available for testing in its entirety within our lab, and therefore only a truncated section of boom was scanned. That section consisted of a single tapespring, or half of the boom sliced longitudinally, from roughly 1.5 m away from the fixed end at the test stand hub. The data obtained from these points was perfectly valid, however because the full dynamic response of the beam was merely obtained in one dimension and even then not of the entire beam, certain mode shapes were indistinguishable from others. In addition, several theoretical modes were also "missing" from the measured data as the one dimensional measurement was unable to determine a natural frequency for the beam along that particular axis.

Ideally, perfect analytical to theoretical correspond to the identity matrix; where the mode shapes for each mode were identical. However, in the case of truncated data, the ability to conclusively determine mode shapes from one another is lost mathematically; there is simply not enough information to exclusively distinguish the

102

modes from one another.   Thus the MAC matrix of Figure 64 should be the identity

matrix as the eigenvectors themselves are identical, however with the truncated

eigenvectors, there are some columns of the matrix that are not reduced to zero as there

are not enough nodal points to mathematically exclude certain mode shapes from

potentially correlated candidates. In addition, even the identical modes do not result

correlate as unity, but rather at some value indicating a high likelihood of correlation.
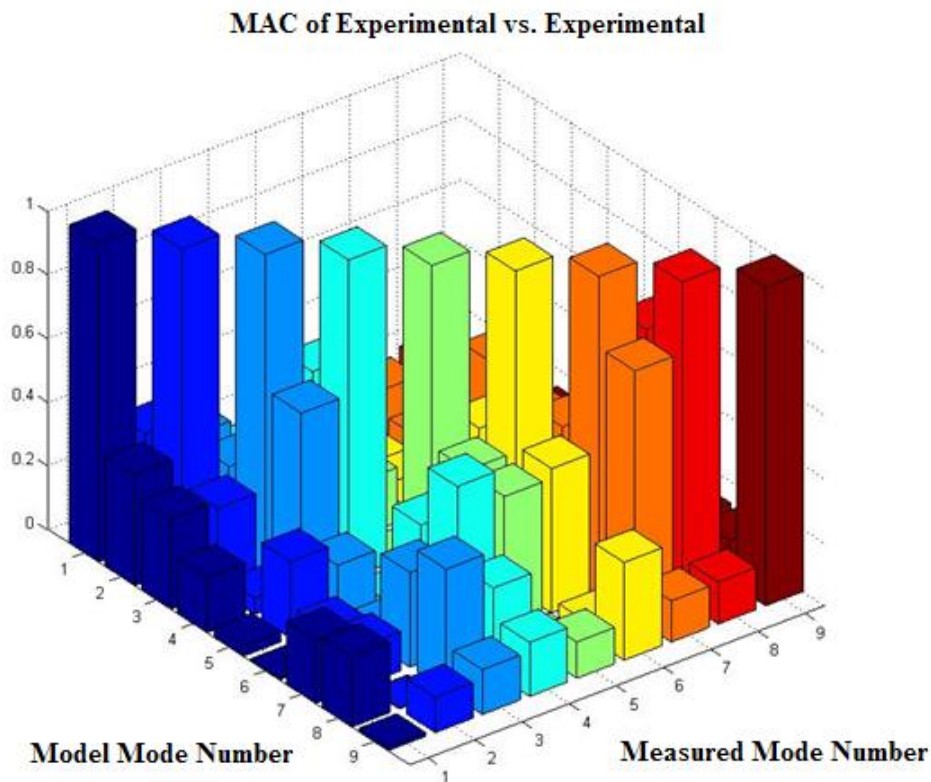

Figure 64. MAC of Experimental vs. Experimental

In this case, where the measured data is truncated, it is necessary to develop a

model with more modes than what were measured to account for "missing" modes and to

ensure the most closely matched mode shapes are indeed those that are being compared.

In Table 4 the MAC values are calculated for each frequency while a corresponding value

of unity indicates perfect correlation between the mode shapes of the theoretical to the experimental.

Table 4. Mode Number and Frequency Correlations

		Measured Mode Number									
		1	2	3	4	5	6	7	8	9	10
Modeled Mode Number	1	0.986	0.417	0.31	0.256	0.035	0.044	0.293	0.316	0.028	0
	2	0.689	0.859	0.056	0.237	0.015	0.13	0.167	0.217	0.002	0
	3	0.69	0.863	0.037	0.236	0.027	0.134	0.167	0.214	0.005	0
	4	0.424	0.126	0.752	0.15	0.392	0.124	0.092	0.255	0.206	0
	5	0.188	0.259	0.991	0.635	0.139	0.021	0.287	0.352	0.124	0
	6	0.198	0.212	0.298	0.33	0.389	0.649	0.64	0.115	0.286	0
	7	0.184	0.251	0.747	0.316	0.746	0.183	0.447	0.307	0.054	0
	8	0.174	0.002	0.107	0.431	0.469	0.862	0.784	0.448	0.197	0
	9	0.123	0.18	0.441	0.529	0.409	0.308	0.97	0.824	0.157	0
	10	0.182	0.036	0.244	0.072	0.11	0.376	0.229	0.467	0.874	0

Working directly with the measured and modeled data, the MAC chart of Figure 65 was produced to ensure that there were not higher frequency mode shapes in the model that would correspond with lower frequency measured modes.
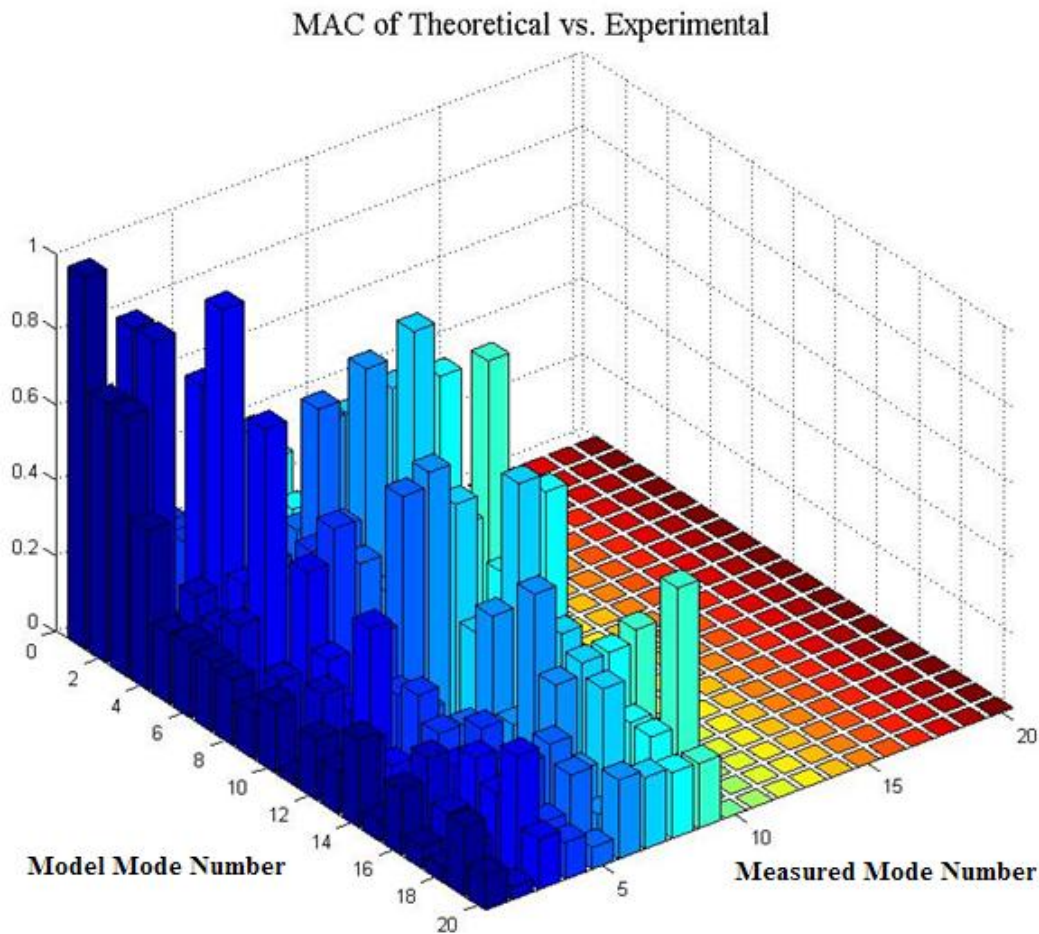
Figure 65. MAC of Theoretical and Experimental Modes

As can be seen, there are clearly no correlated modes beyond the 10th theoretical

mode. As such the MAC could be reduced to that of Figure 66 which clearly indicates

the correspondence of Modes 1 through 9 of the measured data to that of Modes 1

through 10 of the theoretical data. However, the largest correlation values do not, as of

yet, lie along the diagonals due to the "missing" modes in the measured data. Notably,

there are theoretical modes which are not depicted with the current one dimensional laser

vibrometer measurements. Hence, the third measured mode, for example, corresponds

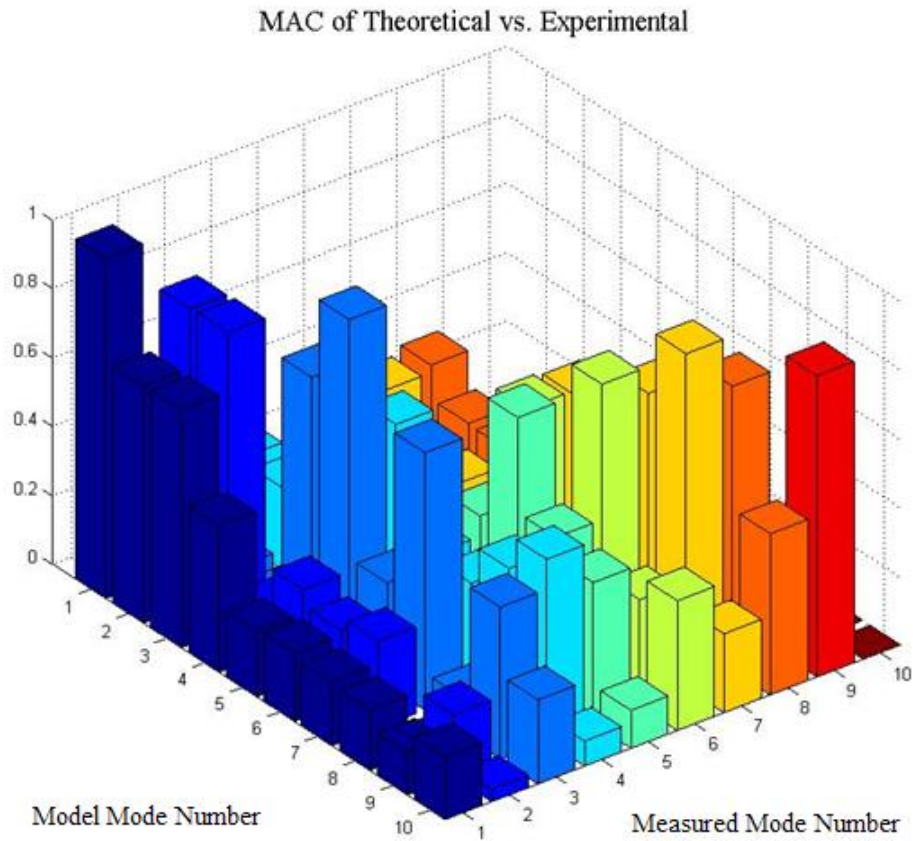most closely to the fifth mode of the theoretical model.

Figure 66. Reduced MAC

Figure 67 below is the complete representation of the mode shapes with the missing modes removed in an attempt to resolve the closest modal correlations along the diagonal; however, there are still modal ambiguities. Comparing with Table 4, it appears the modeled Modes 4 and 6 are not captured at all, and the Measured Mode 4 does not correlate with any modeled modes. The ambiguities and missing modes cannot hope to be resolved conclusively without more data along alternate axes of the beam. The individual mode shapes, however, can still be determined with evidence to support the case of sufficient modeling, as will be seen in the following section.
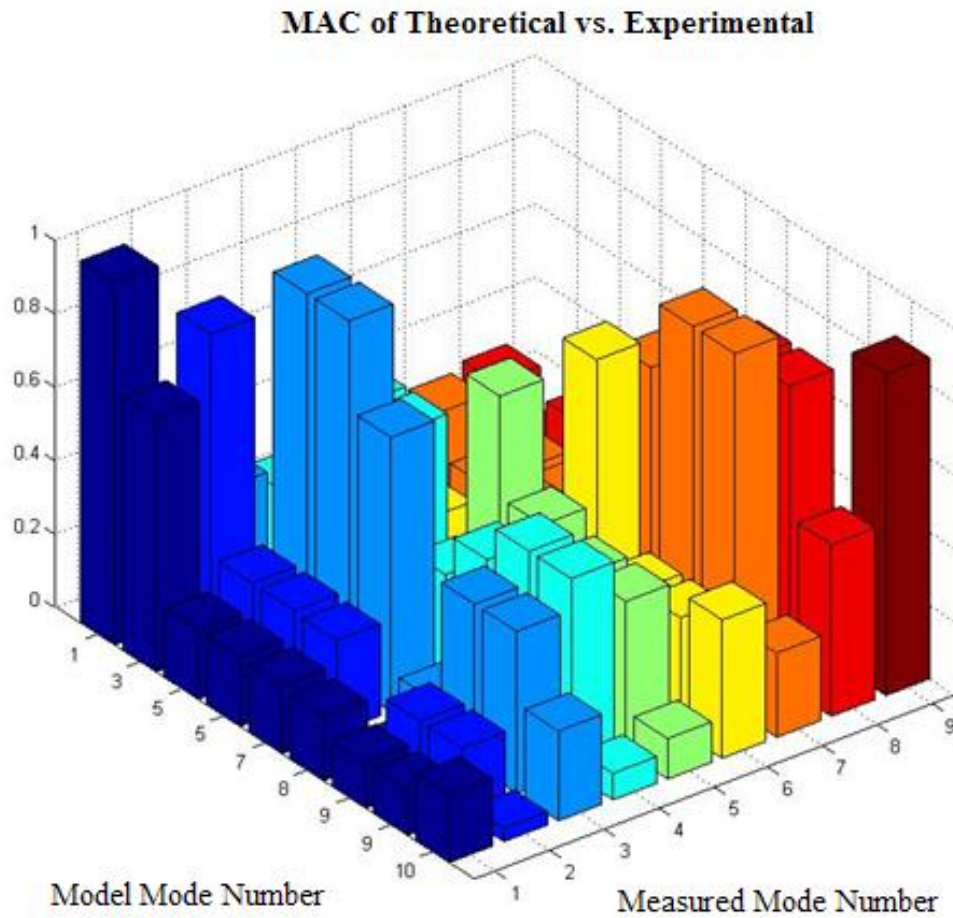
MAC of Theoretical vs. Experimental

Figure 67. Adjusted MAC

4.5 Mode Shape Comparisons

The resulting mode shapes of the measured and modeled data are depicted in

Figure 69 through Figure 90. Each mode shape is the result of stepping the eigenvector

through a full oscillation through the use of a cosine function. The Matlab program

routine developed to accomplish this task is included in the Appendix. The measured

mode shapes are depicted with the closest correlated mode shape from the finite element

analysis in hopes of displaying the similarities between the experimental and theoretical

mode shapes. There are some mode shape redundancies where a single modeled mode is

correlated as the closest modal match for two distinct modeled modes; an artifact of the truncated eigenvector data and the particular testing position and orientation selected. With quality three-dimensional measurement data, these redundancies should cease to exist. Note that the red asterisk points indicate the actual points scanned by the laser vibrometer; while the blue spheres represent the nearest nodal locations to those scanned points in the model. The grid along the beam is presented for purely aesthetic reasons and is not representative of actual measured data. In addition, it is helpful to recall that only a single tapespring is depicted, and the beam itself was attached to the hub at the origin. To extend the grid points to incorporate the remaining physical dimensions of the beam would require complex interpolations for each mode that would have no method of verification. For this reason, merely the scanned portion of the beam was depicted for both the experimentally and theoretically derived data.
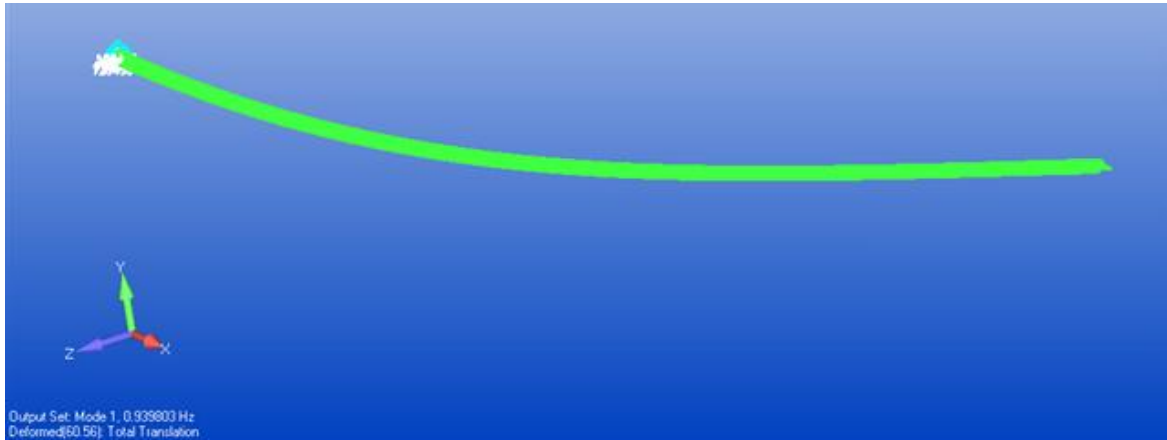
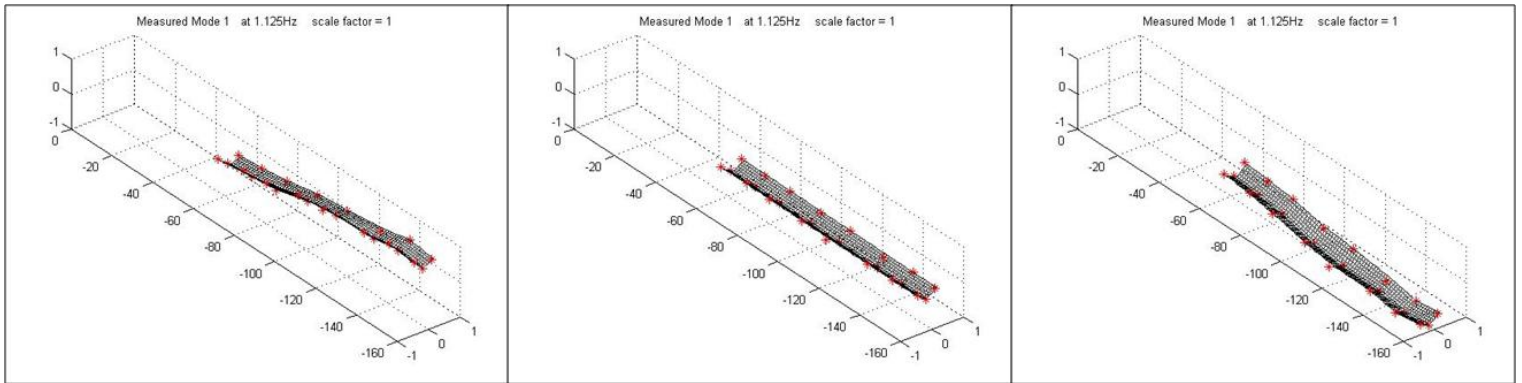**Figure 68. First Bending about Z-axis**

Figure 69. Measured Mode 1 Shape (First Bending about z-axis)
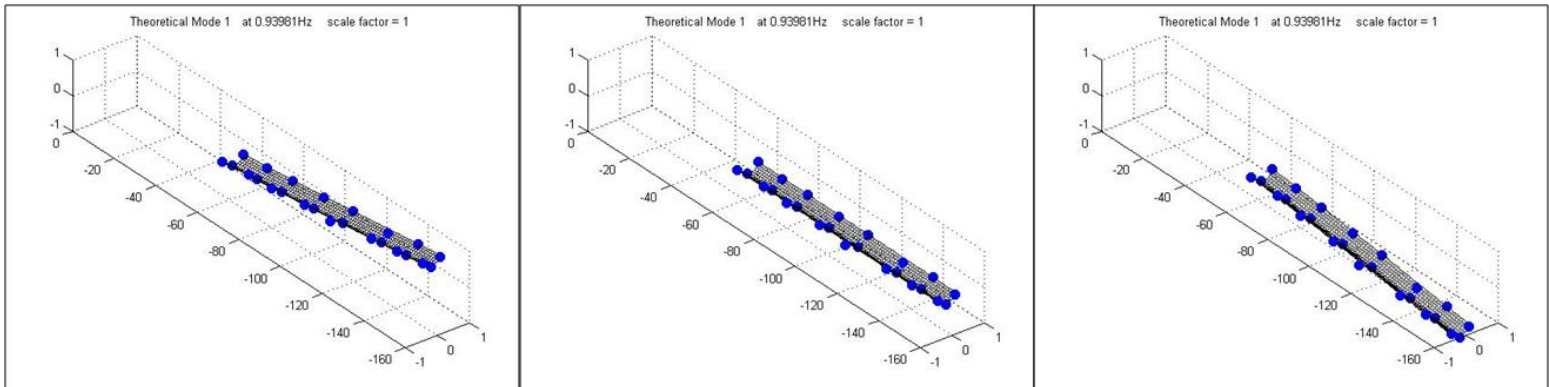
Figure 70. Modeled Mode 1 Shape (First Bending about z-axis)
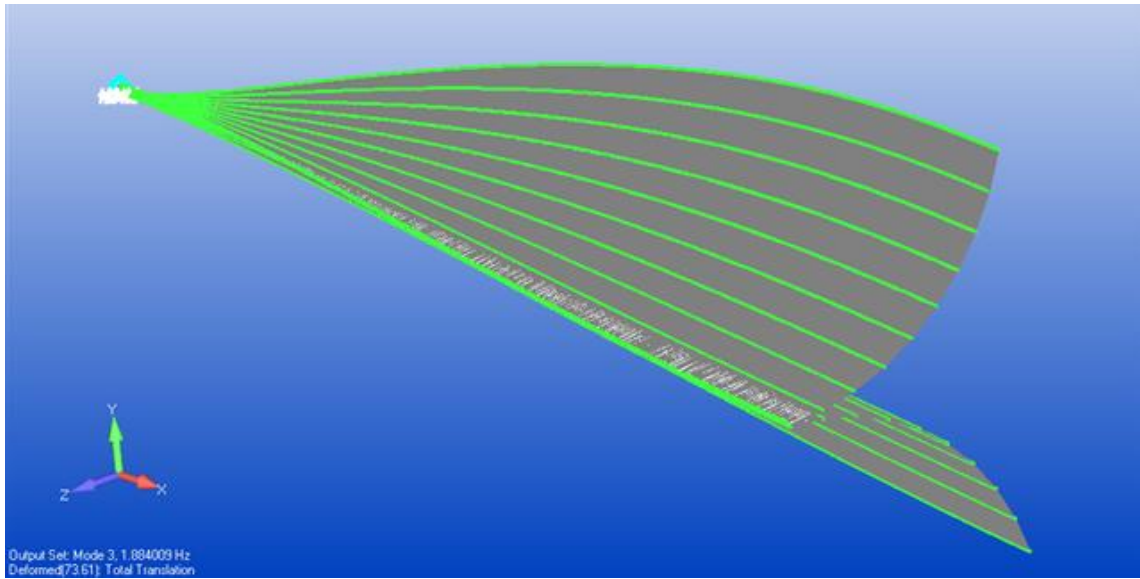
Figure 71. First Torsion
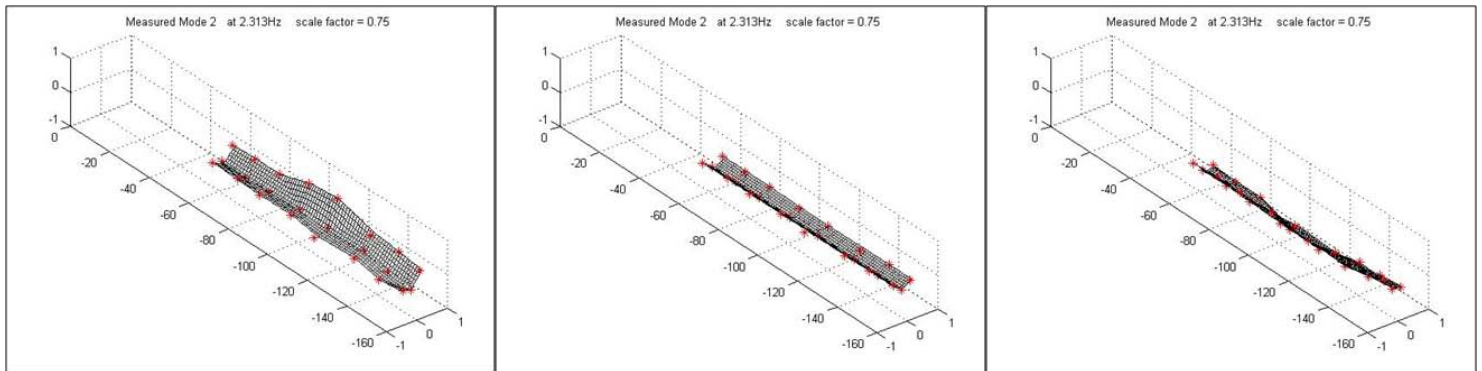
Figure 72. Measured Mode 2 Shape (First Torsion)
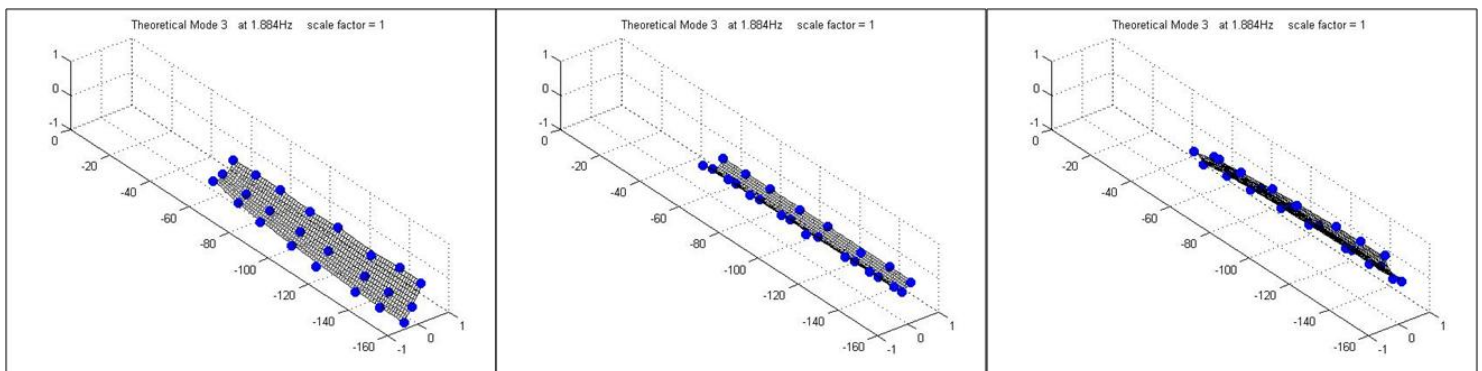
Figure 73. Modeled Mode 3 Shape (First Torsion)

110
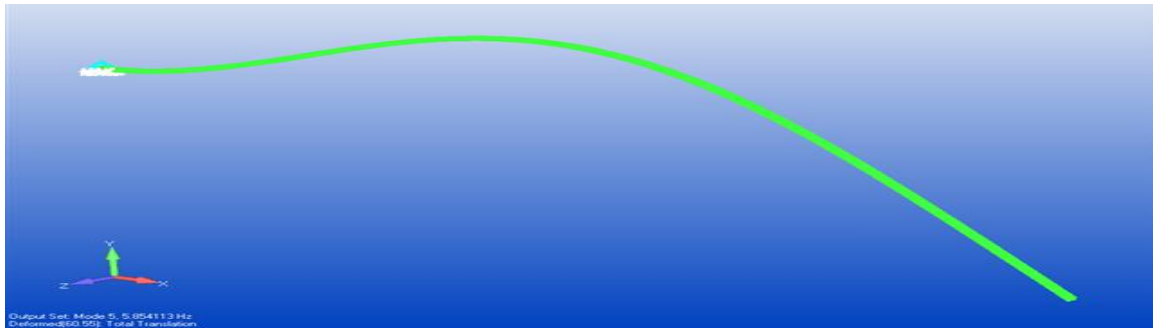
Figure 74. Second Bending about Z-axis

Figure 75. Measured Mode 3 Shape (Second Bending about Z-axis)
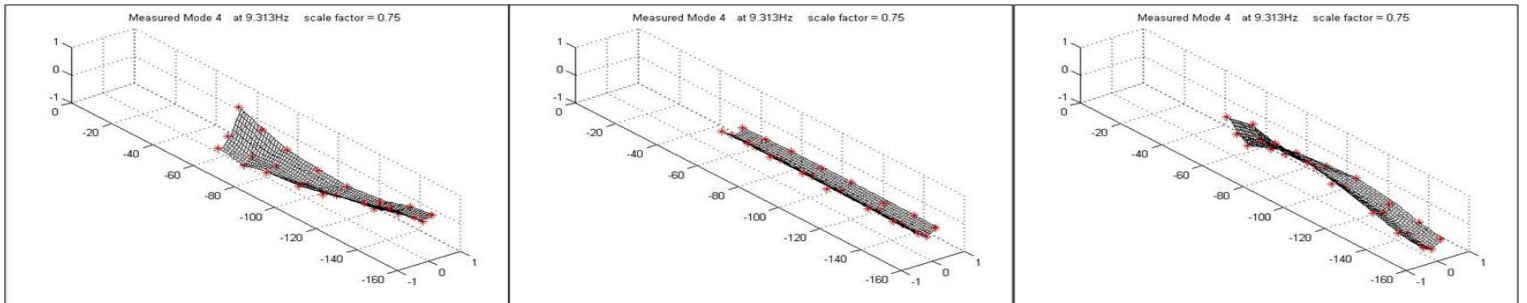
Figure 76. Measured Mode 4 Shape (Second Bending about Z-axis with Twisting)

Figure 77. Modeled Mode 5 Shape (Second Bending about Z-axis)

111
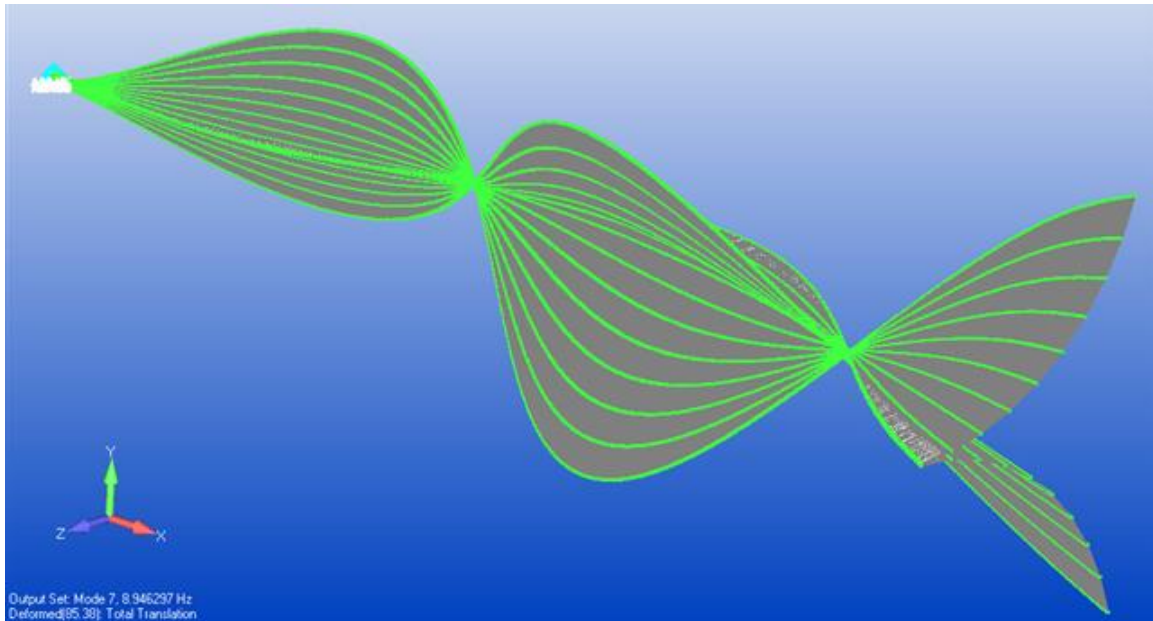
Figure 78. Third Torsion
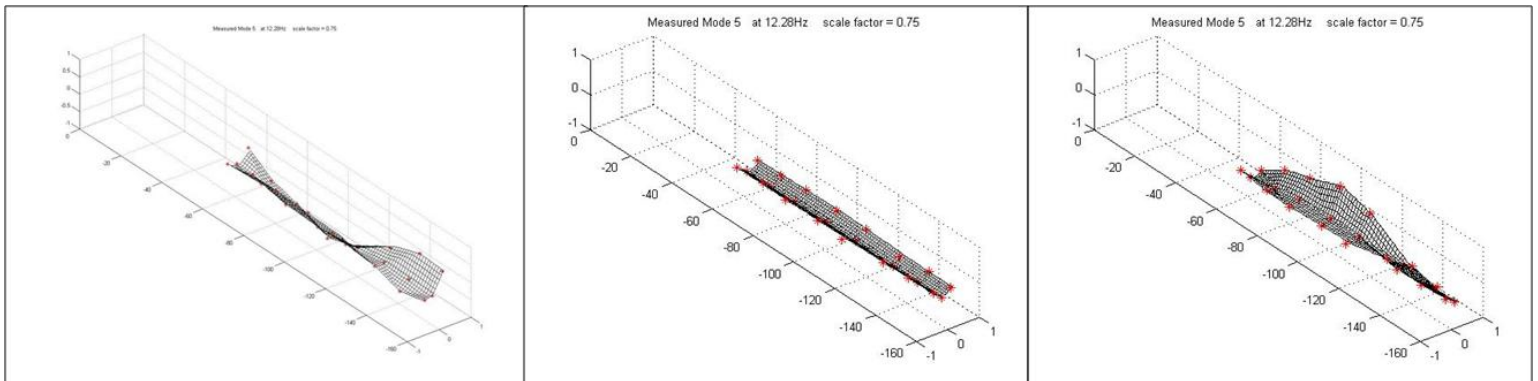
Figure 79. Measured Mode 5 Shape (Third Torsion)
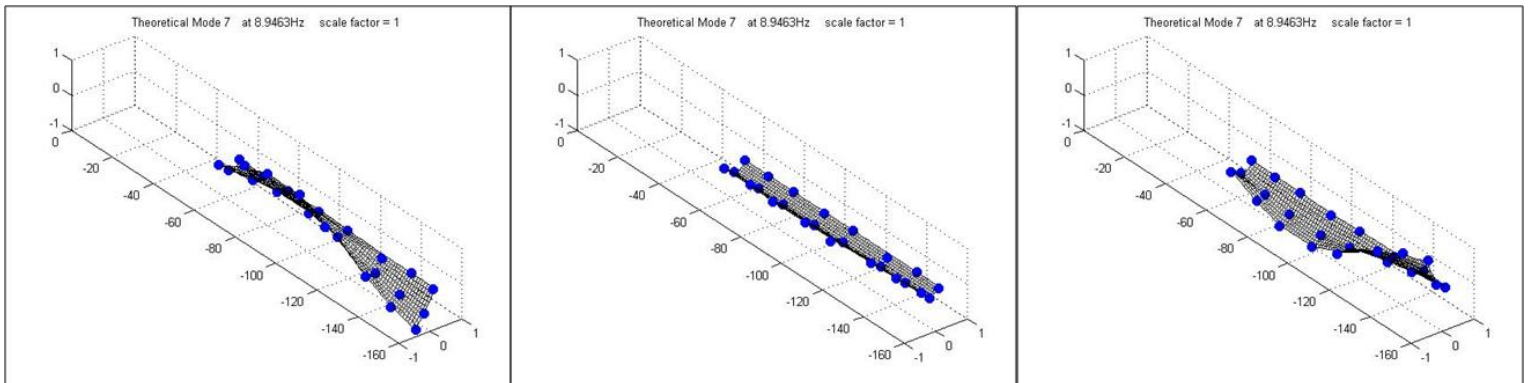
Figure 80. Modeled Mode 7 Shape (Third Torsion)

112
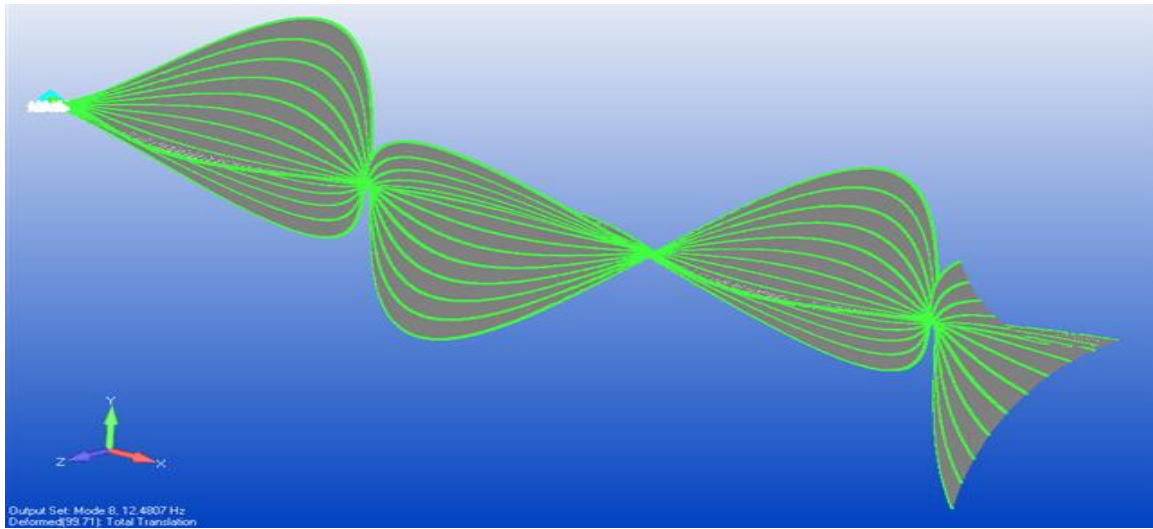
Figure 81. Fourth Torsion
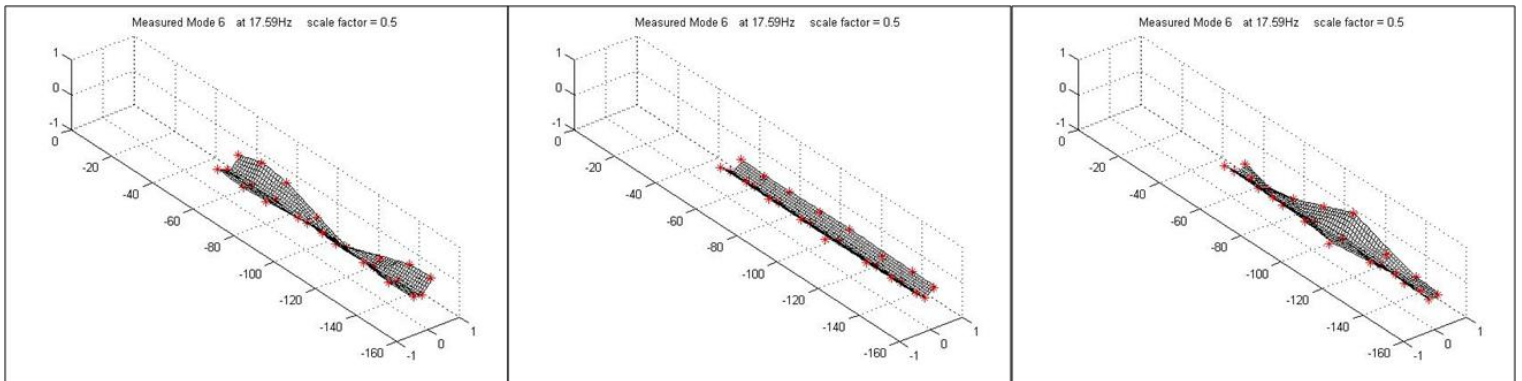
Figure 82. Measured Mode 6 Shape (Fourth Torsion)
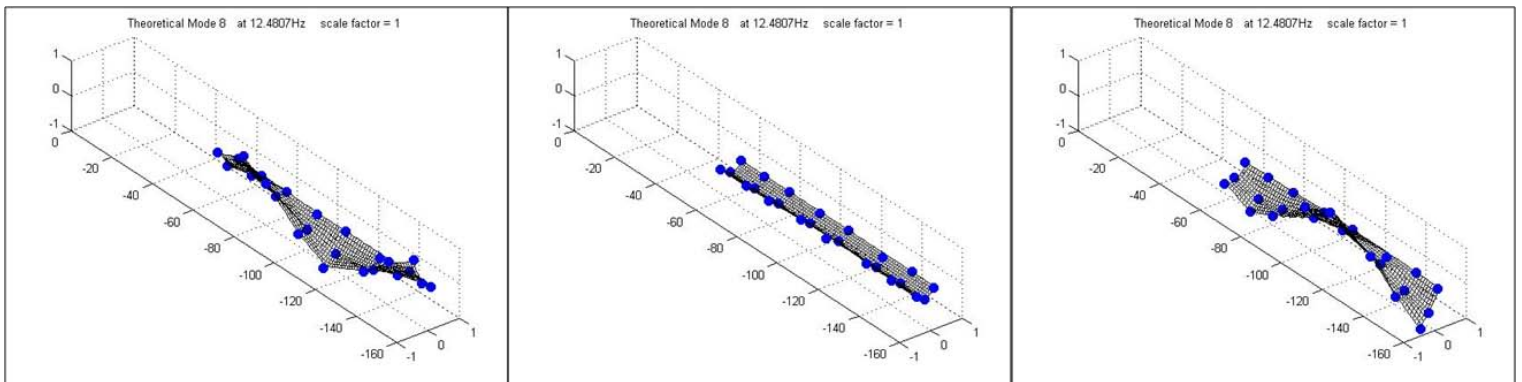
Figure 83. Modeled Mode 8 Shape (Fourth Torsion)
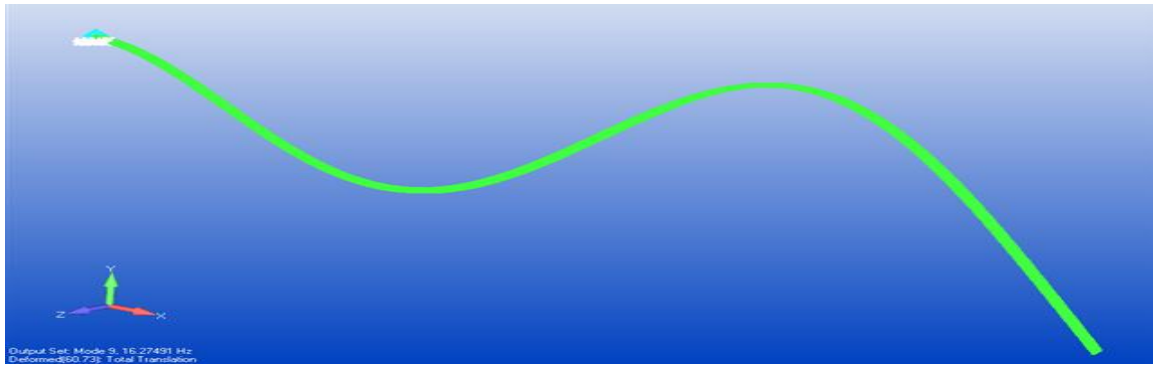
Figure 84. Third Bending about Z-axis
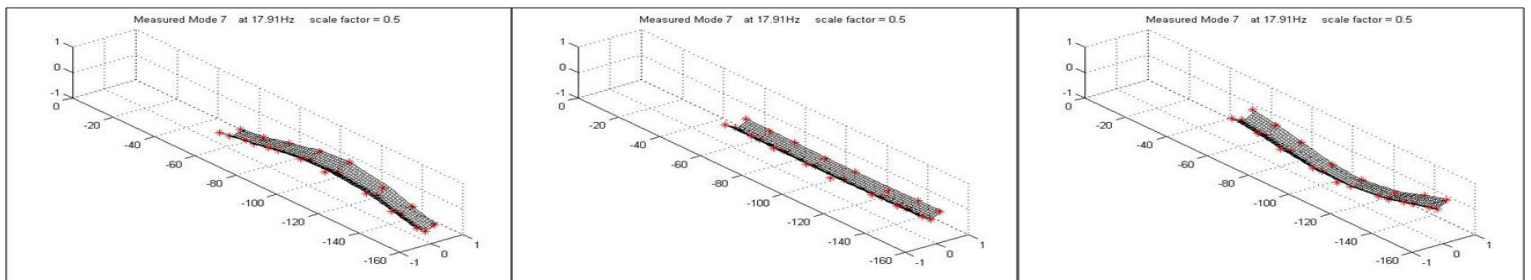
Figure 85. Measured Mode 7 Shape (Third Bending about Z-axis)
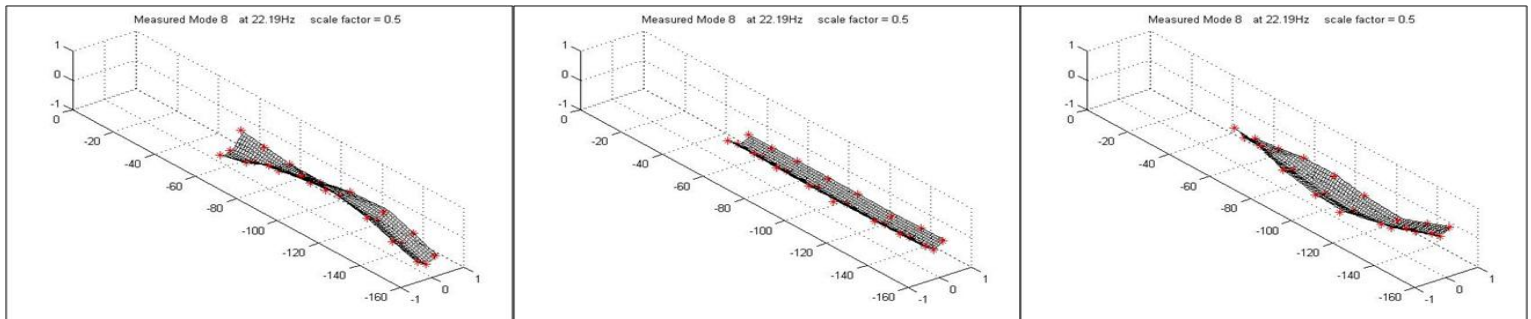
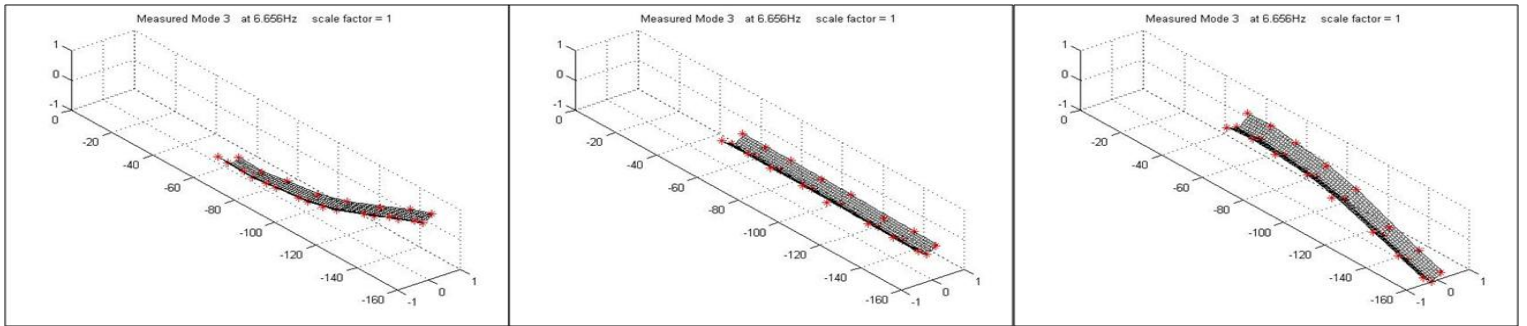**Figure 86. Measured Mode 8 Shape (Third Bending about Z-axis with Twisting)**
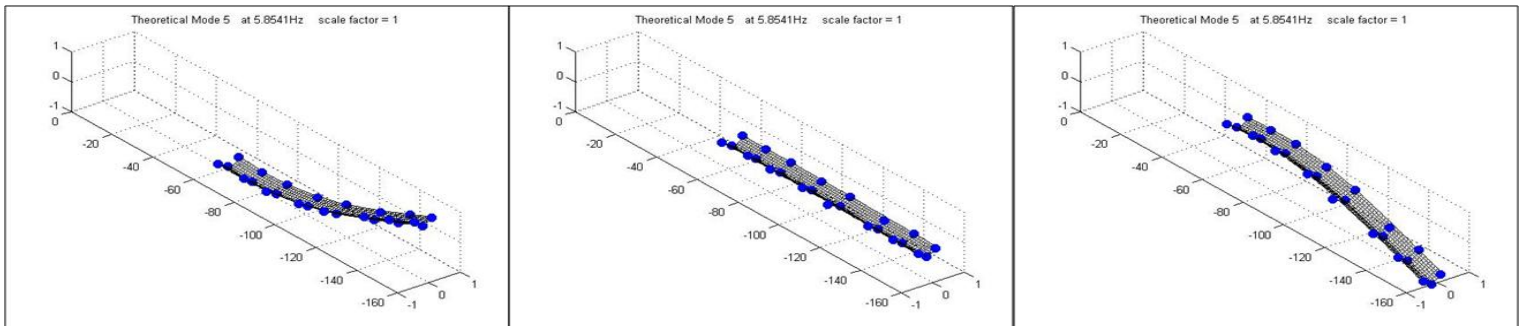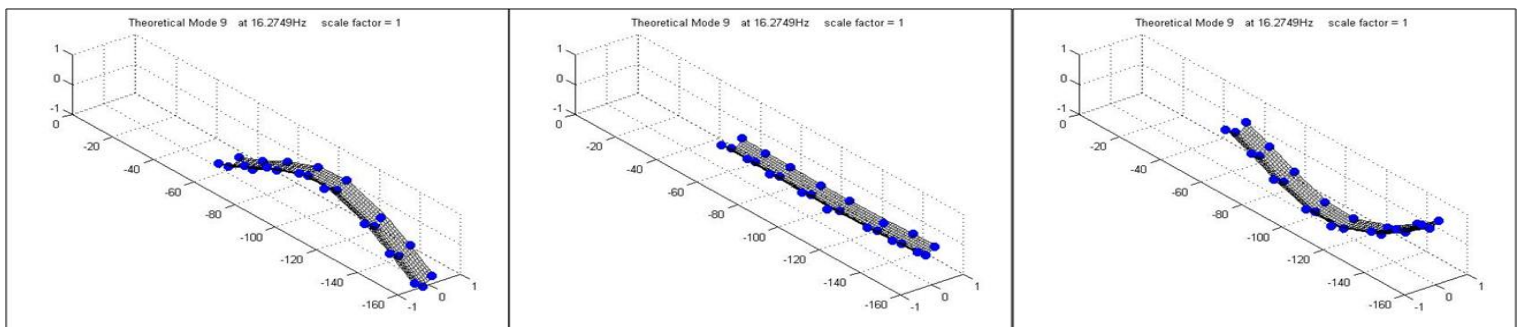

Figure 87. Measured Mode 9 Shape (Third Bending about Z-axis)

114
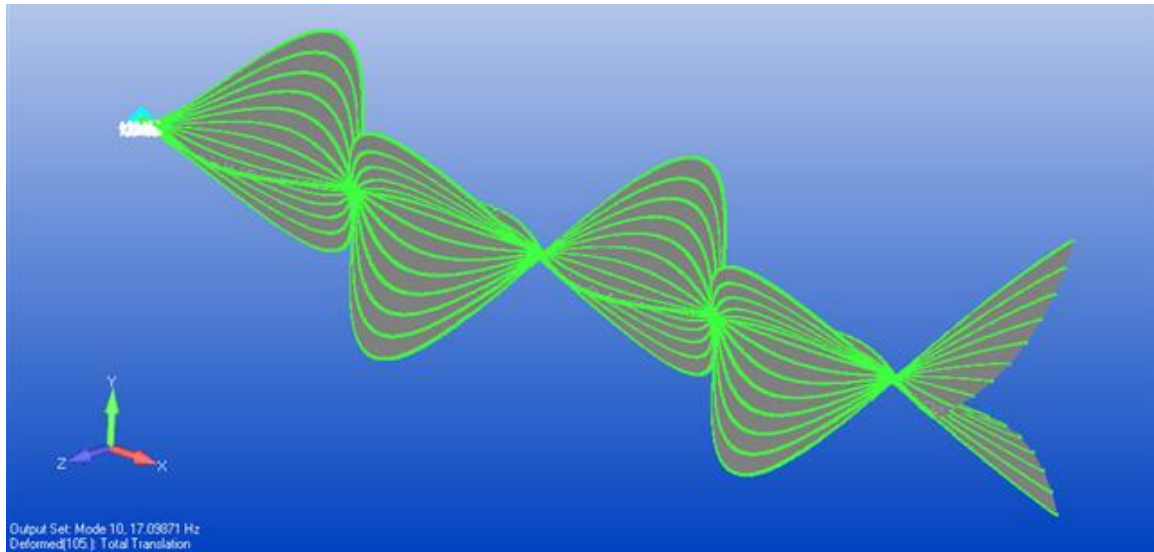
Figure 88. Fifth Torsion
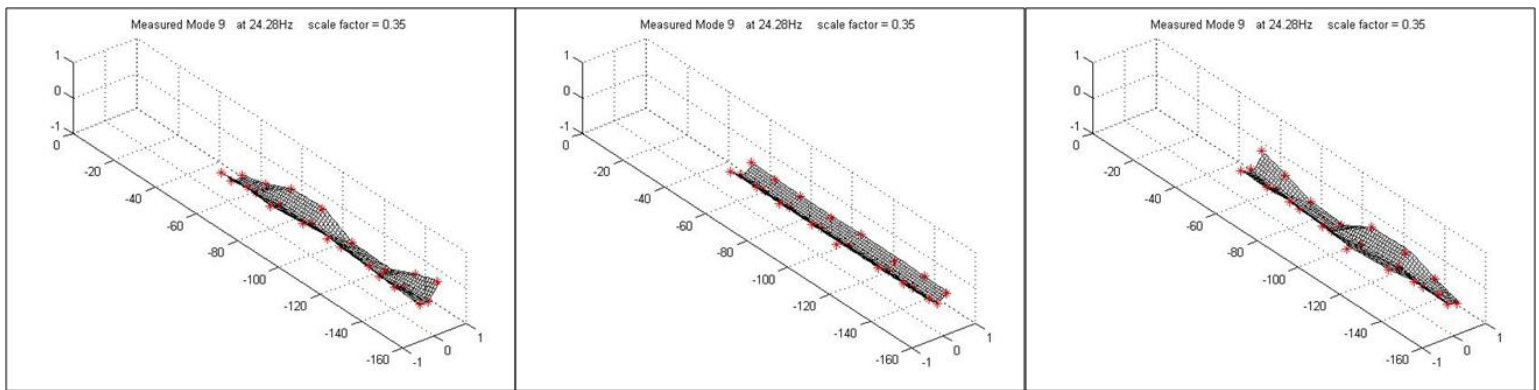
Figure 89. Measured Mode 9 Shape (Fifth Torsion)
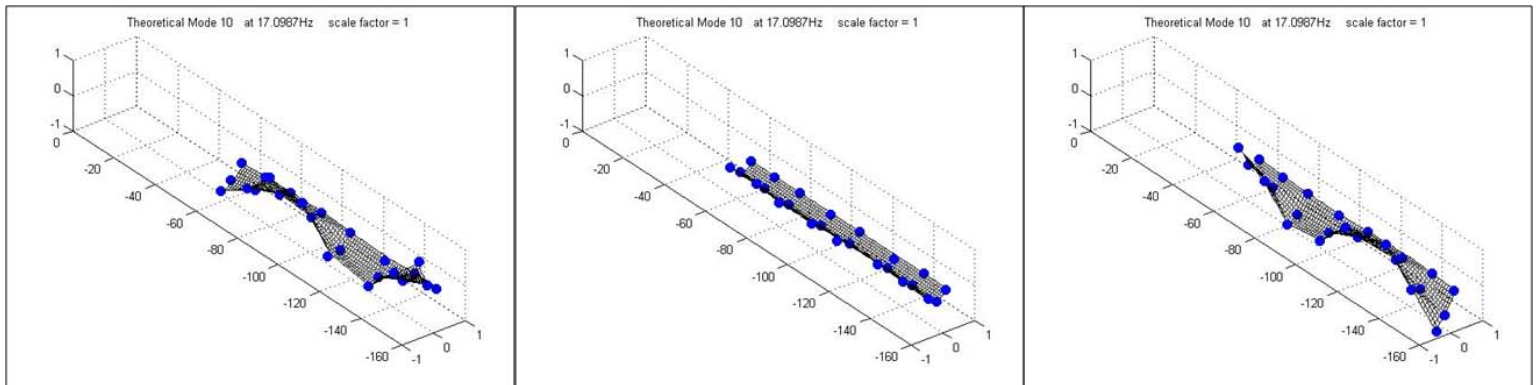
Figure 90. Modeled Mode 10 Shape (Fifth Torsion)

At this stage in the model development, more testing is required to outline the behavior of the entire beam in multiple dimensions and thereby resolve all modal ambiguities before any substantive tuning can be undertaken. The plate element thickness was adjusted so that the mass of the modeled beam matched that of the measured. However, even with such crude tuning methods as merely adjusting the plate element thickness, the correlated mode shapes in most cases clearly resembled one another indicating a fair correspondence between the model and measured data.

4.6 Finite Element Model of Entire Satellite

Once the dynamic behavior of a simple TRAC boom was verified, a finite element model of the boom geometry used on SLiMSat was created using the same plate elements as shown in Figure 91.
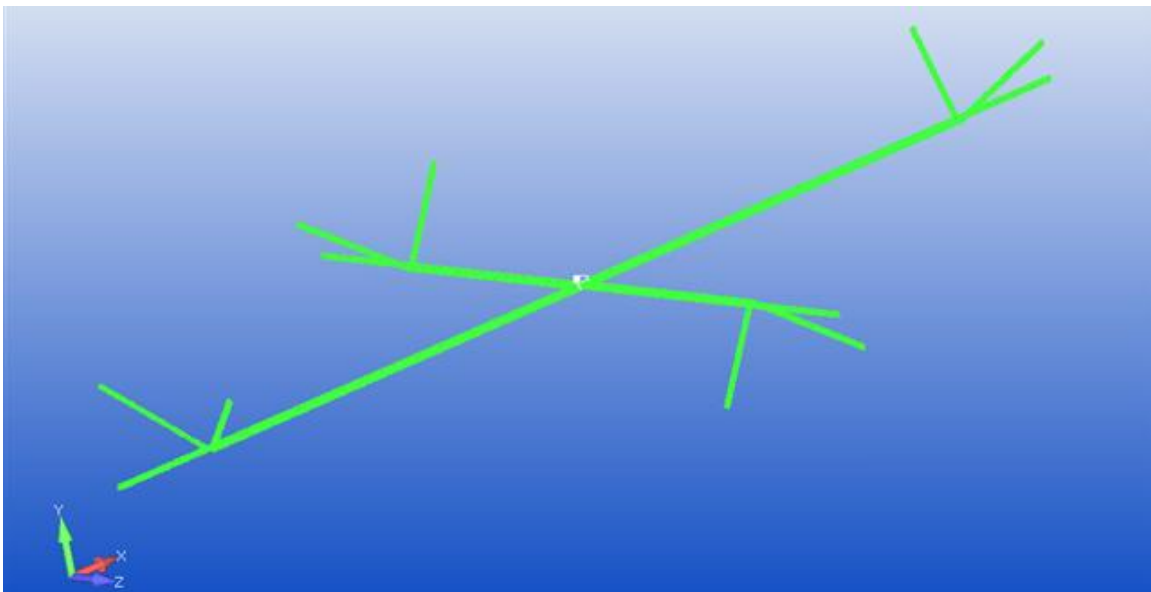
Figure 91. Finite Element Model of SLiMSat Booms

The purpose of this model is to provide an initial deployed configuration prediction of the on-orbit frequencies detected from motion of the reflective surfaces at the extent of each boom. The reflective membranes connected between the arms of boom function as a deployable reflective surface that would be optically detectable by ground based telescopes.

In the model, however, the reflective membranes were not modeled as they were neither under tension nor compression when deployed; and as such, neither contributed nor detracted from the overall satellite dynamics. For simplicity, the booms were rigidly linked to a single central node as shown in Figure 92. The central node, assigned an arbitrary mass of 3kg, was representative of a 3U CubeSat with the exclusion of four 'Frogleg' Booms.
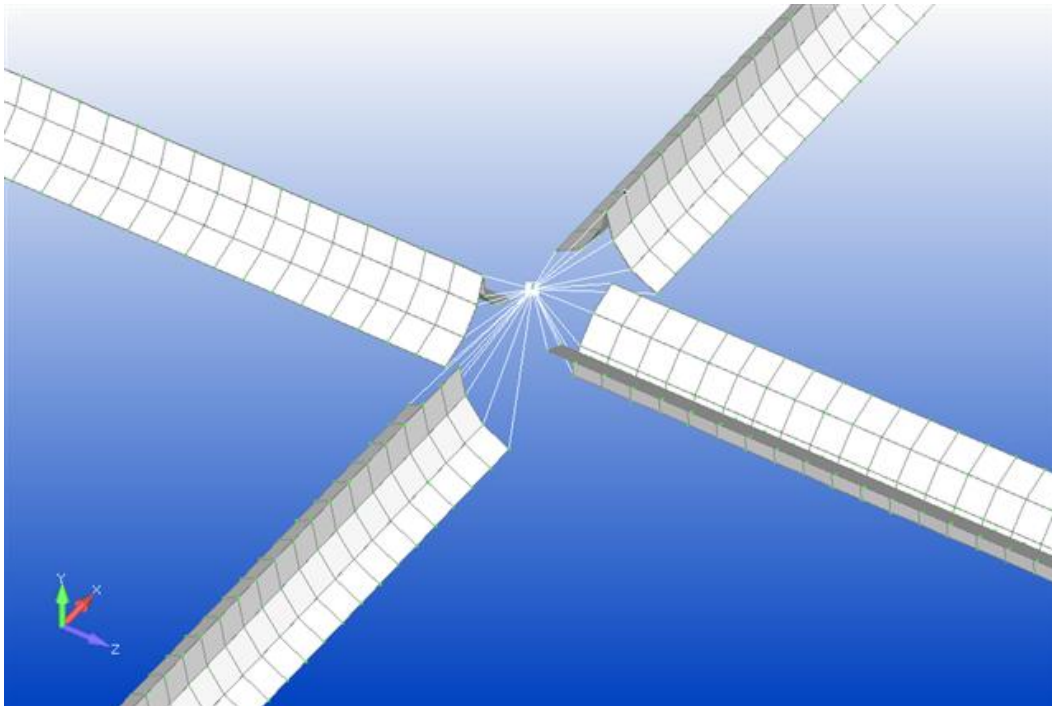
Figure 92. Central Node of SLiMSat FE Model

The modal frequencies along with a brief mode shape description are listed below in Table 5, noting that matching pairs are denoted with asterisks.

Table 5. SLiMSat FE Model Mode Shape Frequencies and Descriptions

Mode	Frequency (Hz)	Mode Shape Description
1	0.19961	Long Beam In-Phase Torsion*
2	0.202339	Long Beam Out-of-Phase Torsion*
3	0.30595	Short Beam In-Phase Torsion*
4	0.307895	Short Beam Out-of-Phase Torsion*
5	1.424615	Long Beam In-Phase 'Frogleg' Flapping
6	1.453691	Short Beam Out-of-Phase 'Frogleg' Flapping
7	1.493382	Long Beam Single-Arm Out-of-Phase 'Frogleg' Flapping
8	1.518472	Short Beam Single-Arm Out-of-Phase 'Frogleg' Flapping
9	1.532907	Long Beam Alternate Single-Arm Out-of-Phase 'Frogleg' Flapping
10	1.53354	Quad-beam Out-of-Phase Alternating 'Frogleg' Waving*
11	1.55414	Short Beam Alternate Single-Arm Out-of-Phase 'Frogleg' Flapping
12	1.556733	Quad-beam In-Phase Alternating 'Frogleg' Waving*
13	1.970393	Long Beam In-Phase 'Frogleg' Arm Crossing*
14	2.036452	Short Beam Out-of-Phase 'Frogleg' Arm Crossing*
15	2.102564	Long Beam Out-of-Phase 'Frogleg' Arm Crossing*
16	2.126307	Short Beam In-Phase 'Frogleg' Arm Crossing*
17	2.889249	Long Beam Bending with In-Phase Arm Crossing
18	3.123666	Long Beam Torsion
19	5.845071	Quad-Beam Torsion
20	6.846362	Single Long Beam Torsion
21	6.991067	Alternate Single Long Beam Torsion
22	8.432473	Short Beam Bending
23	8.737261	Short Beam Torsion
24	11.03144	Out-of-Phase Long Beam Bending

The mode shapes of the SLiMSat model are indicative of the predicted performance of the 'Frogleg' booms on orbit. Notionally, the light reflected off the deployed vibrating boom would have some flashing frequencyas observed from the ground. By resolving this frequency and knowing the reflectivity characteristics of the booms at each modal frequency, the dominant mode shapes of the orbiting satellite booms could be determined passively. Some of the more intriguing mode shapes are depicted below in Figure 93.

Mode 5: Long Beam In-Phase Frogleg Flapping at 1.4246 Hz

Mode 10: Quad-beam Out-of-Phase Alternating Frogleg Waving at 1.53354 Hz

Mode 17: Long Beam Bending with In-Phase Arm Crossing at 2.889 Hz

Mode 24: Out-of-Phase Second Long Beam Bending at 11.0314 Hz
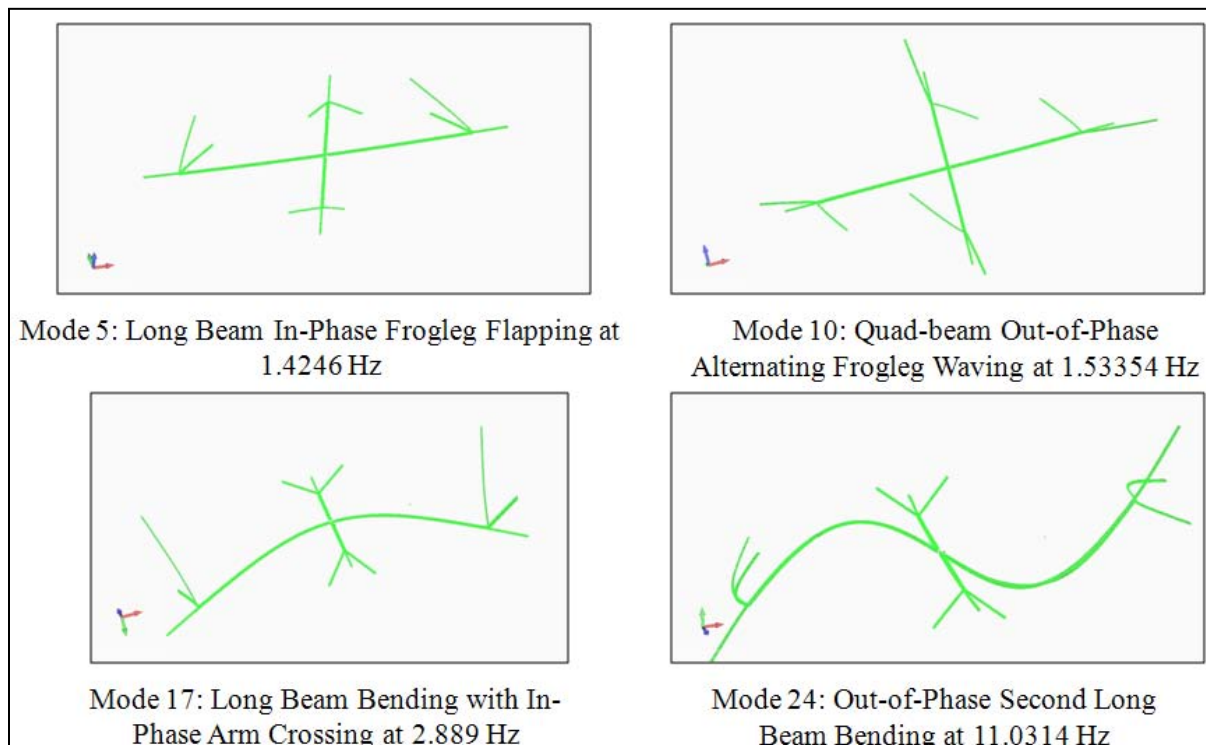
Figure 93. Sampled SLiMSat Theoretical Mode Shapes

With the SLiMSat model, the mode shapes of the deployed satellite are known; however, the appearance of the satellite from the ground is still in question. Future groups will need to determine the reflectivity of the satellite in multiple attitudes across a

large bandwidth of frequencies in order to predict how on-orbit behavior would appear from the ground.

4.7 Boom Prototype Deployment

The goal of this deployment testing is to verify the viability of 'Frogleg' boom end design concept. Future tests will characterize the specific parameters of the deployment and possible on-orbit detection methods. Deployment testing was conducted in the Dynamic Inflight Test and Measurement laboratory here at AFIT.

Unfortunately, after attempting to wind the Stanley tapespring onto the SLiMSat hub, we determined conclusively that laser-welded commercial off the shelf tape measure, while seemingly well suited for space applications, lacks the necessary structural constitution to provide repeatable boom deployments. The constructed beams behaved flawlessly in their deployed configuration, but successive wraps along the hub induced fissures along the welds in every boom constructed. Audible creaking and cracking was apparent from every attempt to wind the booms in their stored configuration; with noticeable weld disintegration, in some cases, from the first wrap. Upon further investigation, extensive oxidation was present along the weld which could have potentially exacerbated the failing integrity of the boom. Arguably, booms in space will deploy a single time and remain in that position such that a degree of diminished structural integrity is acceptable; however, it is clear that welding conventional tapespring does not provide satisfactory results. Further research is required to determine the exact material properties desired for future booms, but by postponing and controlling the heat treatment process numerous materials could be adapted with satisfactory results.

120

Nanosail-D employed the use of Elgiloy steel, as well as rolling the steel from flat stock themselves (Banik J. , 2008). This is, perhaps, the best option for future booms should time and budgetary constraints become less of an issue.

The deployment testing required the coordination of two distinct deployment phases: the membrane unfurlment phase, and the main boom extension phase. Unfortunately these tests were not able to be accomplished in a complete satellite configuration as in Figure 94 as the booms themselves degraded enough to preclude any actual deployment. However, the design proof of concept was successfully demonstrated by hand-feeding a full boom structure through a single SLiMSat panel.
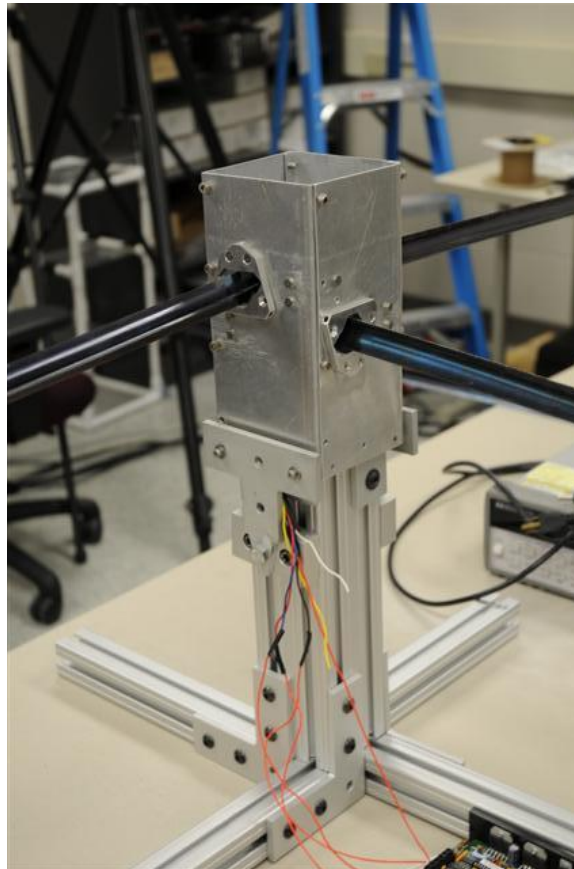
Figure 94. Desired SLiMSat Deployment Testing Configuration

The 'Frogleg' boom was designed to deploy a reflective membrane by extruding a longitudinally cut TRAC boom through a specially-shaped 'slider' component that would be released from a spring loaded catch. The 'Frogleg' boom in its fully deployed configuration, as shown in Figure 95, was created by water-jetting a TRAC boom with the cuts shown in Figure 96. The longitudinal cut allows the half the upper half of the boom to project out of the 'slider', while the relief cuts prevent the boom from splitting further than what was intended. The 'slider' lock-tab cut allows a small section of beam to be bent out of the plane of the beam creating a tab that locks the 'slider' in place once it is released from the wall of the satellite; preventing the deployed membrane from collapsing the deployed arms of the 'Frogleg' boom.
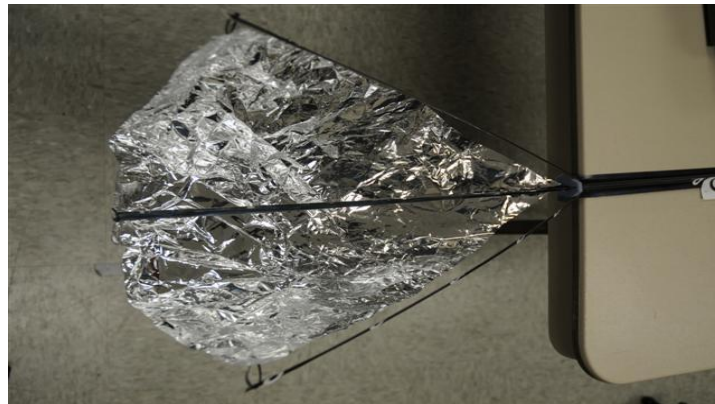
Figure 95. Fully Deployed 'Frogleg' Boom
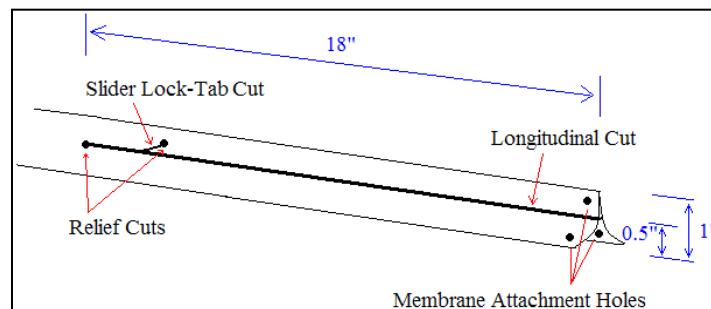
Figure 96. 'Frogleg' Boom Cuts

122

The geometry of the 'slider' is shown in Figure 97. The 'slider' allows the central arm of the cut 'Frogleg' boom to extend through a central gap, while the 'Frogleg' arms extend along either side of the ramped surfaces. The 'slider' has three half-domed detents along its sides to interface with the spring-loaded ball bearings of the 'catch' assembly of Figure 98. In addition, the 'slider' has two centrally located holes for reflective membrane attachment.
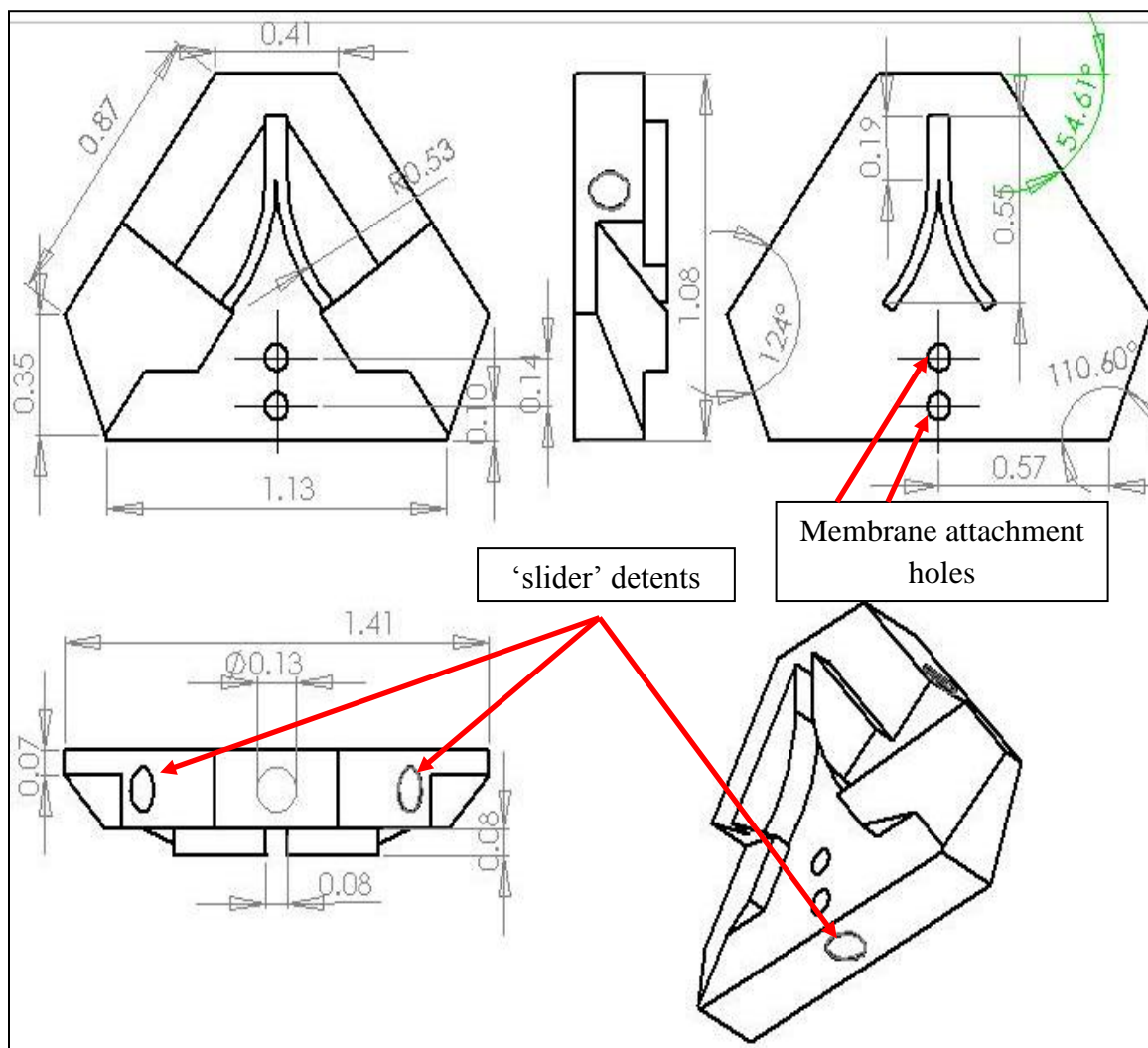
Figure 97. SLiMSat 'slider' Geometry

Figure 98. SLiMSat 'catch' Assembly Drawing

The 'catch' assembly shown in Figure 98 positions three ball bearings in the 'slider' detents with springs that are adjusted with set-screws. However, in order to reduce drawing clutter, only one ball-bearing is shown in Figure 98. Each SLiMSat side panel uses a single 'catch' Assembly, with a total of four 'catch' Assemblies per satellite. A single prototyped 'catch' and 'slider' assembly is shown in Figure 99.

124

Figure 99. Prototyped 'catch' and 'slider' assemblies with membrane attachment

Figure 100, Figure 101, and Figure 102 depict the stepped deployment of the 'Frogleg' Boom and membrane as they move from the initial stowed position through the main boom extension. The membrane itself would be folded beneath the body mounted solar panel as described in the companion document, prior to deployment (Swenson, 2010).
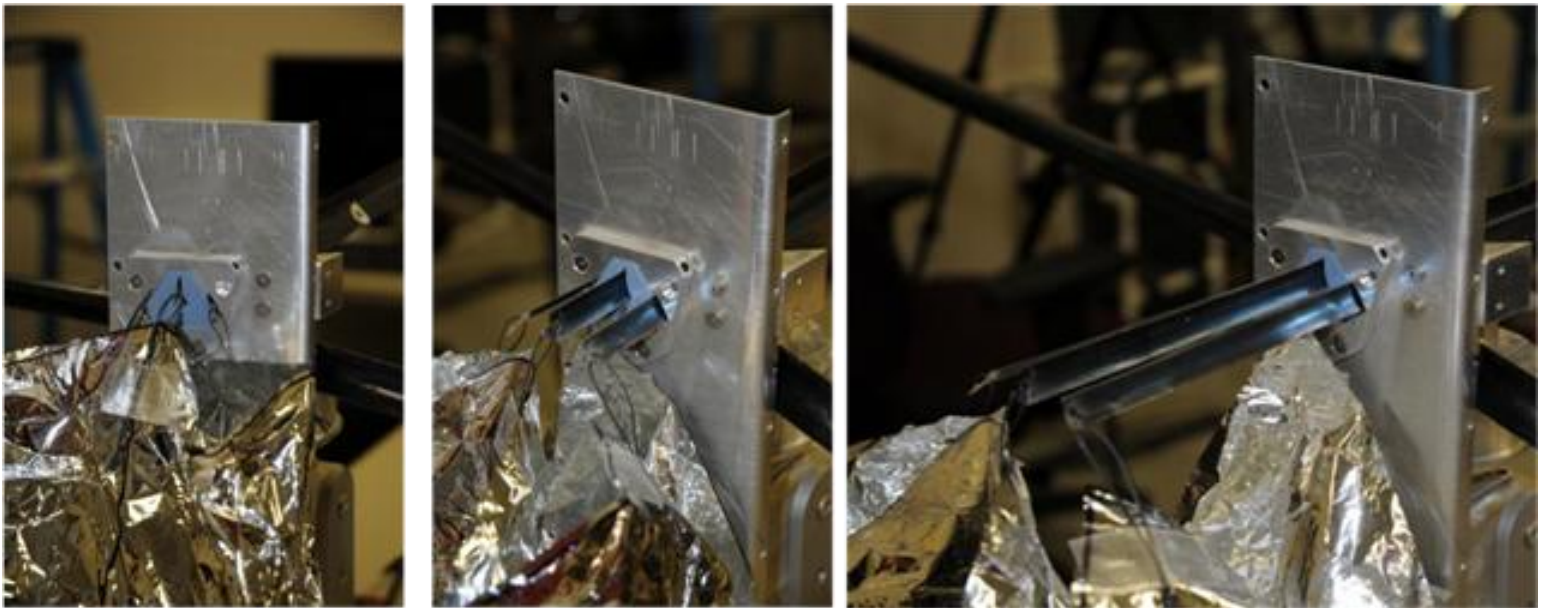
Figure 100. Initial 'Frogleg' Boom Deployment from Stowed Configuration (Far Left) to Pre-Arm Flair (Far Right)
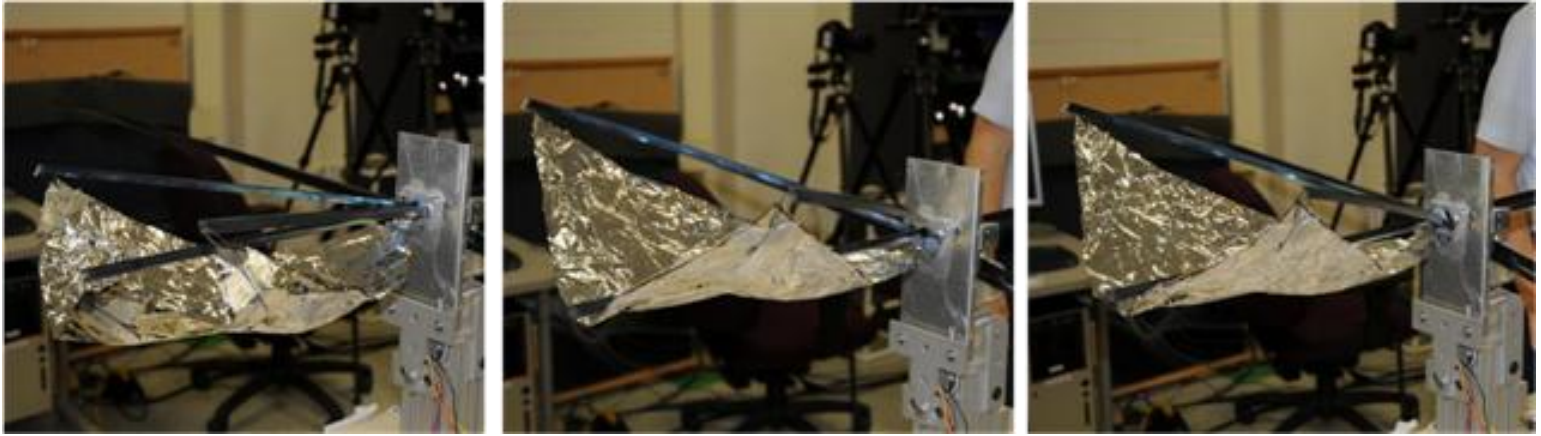
Figure 101. 'Frogleg' Boom Deployment from Initial Arm Flair (Far left) to 'slider' Release (Far Right)
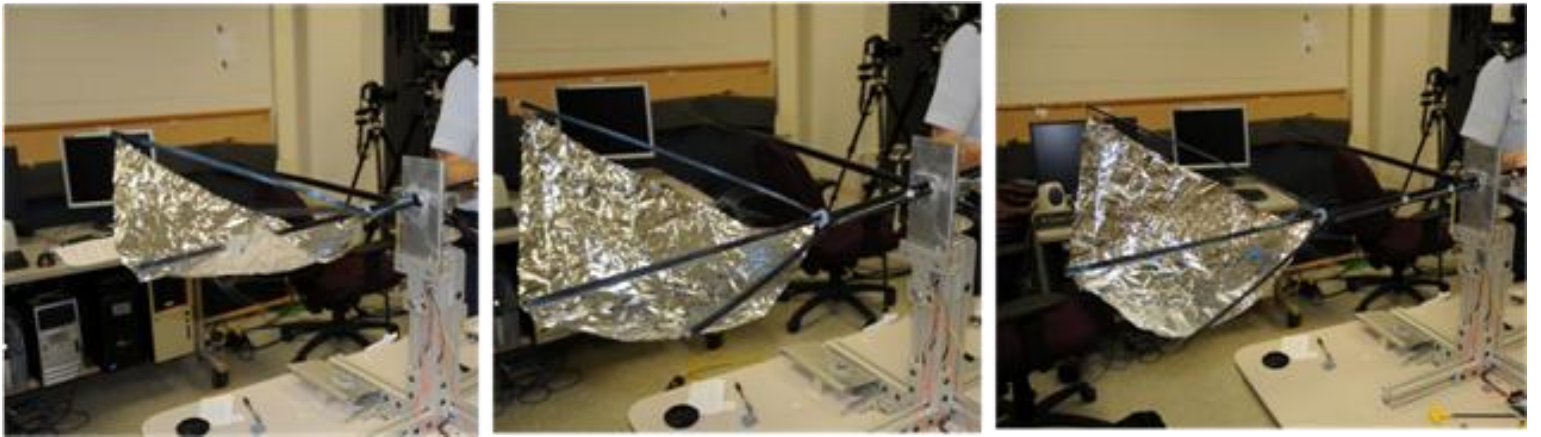
Figure 102. Main Boom Extension Phase of 'Frogleg' Boom Deployment from 'Post-slider' Release (Far Left)

4.8 Summary

The dynamic characterization of the booms provides a wealth of insight into the behavior of the booms. The finite element model of the single boom with TRAC boom geometry provided reasonable modal correlation with that the measured boom. The Finite Element Model of SLiMSat with four 'Frogleg' booms will provide valuable insight for future on-orbit reflectivity determination. Fortunately, the notional proof-of-concept deployment tests were still possible even with booms that were unable to be

126

stowed and deployed from within SLiMSat. However, had the booms themselves been

made from some other less brittle material, successful deployment seems not only

possible, but probable.

V. Conclusions and Recommendations

5.1 Chapter Overview

Contemplating the success of this research, it is necessary to determine which questions were answered and to what degree, as well as which still remain. Perhaps the most fundamental inquiry in this work involves the maximization of deployable surface area from the central hub of the CubeSat.

Thorough this body of research we can draw four primary conclusions, namely: that booms of various lengths can be incorporated around the same diameter hub; that TRAC boom laser welding techniques and hub fixture methods produce booms of predictable dynamic behavior; that FE models of TRAC boom behavior were validated by test results; and finally that the 'Frogleg' boom-end design is a viable method to deploy a reflector on the end of a TRAC boom. In consideration of this research success, it is important to note that the TRAC booms constructed for SLiMSat from conventional tapespring were not expected to perform as fully functional spaceflight hardware; they were merely a template for SLiMSat mission development. And, as a design tool, SLiMSat's booms were indispensible

5.2 Research Conclusions

Aside from the material incompatibility, the TRAC boom geometry holds enormous potential for future deployable structures. This research demonstrated that 5 m and 3m sections of boom geometry could be wrapped around a center hub successfully. Furthermore, with a judicious choice in hub diameters, the various-sized booms can reach their full deployment state at the same time; requiring the use of a single deployment

128

motor, and advantageously reducing the anticipated deployment shock to the satellite. By implication, future single booms of up to 10 m in deployed length could be wrapped around a similar hub design with favorable results. Additionally, the booms themselves, aside from oxidation issues which could be avoided in future booms with a thin protective coating, were constructed in a remarkably uniform manner. Laser welding the two halves of spring was an effective method of constructing the TRAC boom cross section. Furthermore, by using slightly thinner material for the booms, many of the buckling issues present in the current SLiMSat booms could potentially be avoided. Thus, the boom geometry and construction methods appear repeatable and significant value to future groups.

Another result of SLiMSat Research was the production of a credible FE Model developed for a single TRAC boom and verified by positive correlation with experimental data. The highly flexible booms were difficult to analyze, but not impossible. The successful experimental setup using an electromagnet and a single head laser vibrometer provided satisfactory coherence for dynamic characterization and modal analysis. The experimental method was not trivial; involving a great deal of trial and error to obtain data of a merely marginal level of acceptability. However, the time invested in testing process will pay dividends toward the essential understanding of the performance characteristics of future beams. Furthermore, the FE Models will play a crucial role in the future determination of the on-orbit behavior of SLiMSat based on its ground based visibility.

In tandem with the knowledge of beam performance characteristics, the development of a satellite prototype presented another incomparable learning tool. Potential issues such as component clearance, deployment binding as well as several design innovations were all resolved by the production and examination of a functioning prototype; demonstrating once again the exceptional difference between paper and actual design development. The development of a SLiMSat satellite prototype resolved numerous unknowns such as the need for motorized boom deployment definitively. More ideas were formulated and discredited in a single hour by handling a physical structure, than in many days of paper design and theoretical postulation. However, even with the working prototype there were still limiting factors within our design.

5.3 Lessons Learned

As previously mentioned, commercial off-the-shelf tape measure steel readily adapts to TRAC boom geometry and deployed behavior, but ultimately fails to wrap on hub repeatedly. The root cause of the tapespring weld failure is due to the over-engineered (for TRAC boom application) thickness of the tape measure steel causing the weld to shear along dissimilar radii of curvature. In addition, the heat treatment process, needed to maintain the tapespring geometry, leaves the steel too brittle to work without cracking; unnecessarily increasing the difficultly in fabricating the prototyped 'Frogleg' boom-ends, and making them unduly prone to failure. It was also discovered, that future laser welds will needs protection from oxidation.

In addition to the lessons learned about the TRAC booms themselves and the fabrication process it is clear that future SLiMSat designs will require the use of a

deployment motor to extend the booms on orbit; the strain energy contained in the stowed booms is not enough to overcome frictional forces for successful deployment. Furthermore, a retaining method, such as spring loaded rollers, will be required to hold booms in place around the hub during deployment. It was initially thought that phenolic blocks could retain the booms on the hub during deployment as shown in Figure 103.
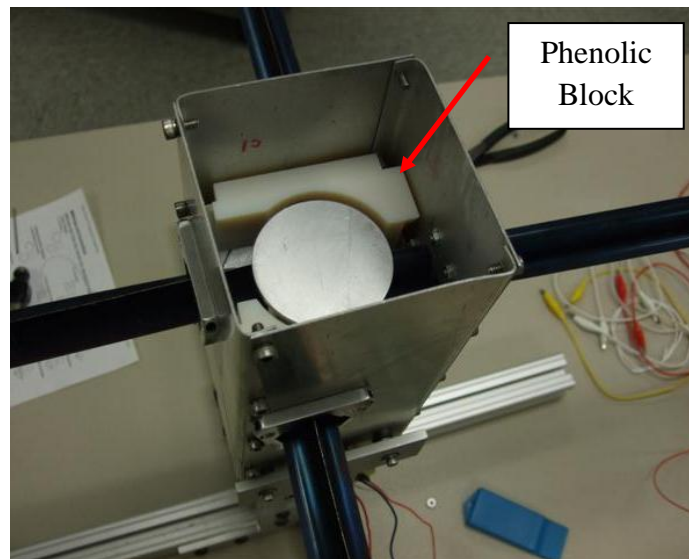
Phenolic Block

Figure 103. SLiMSat Hub with Phenolic Block Guides

However, through the course of prototype development, it was clear that the use of phenolic blocks would increase the frictional resistance to deployment to such a degree as to prevent motor deployment. Alternatively, static rollers were employed as in Figure 104 to effectively reduce the resistance to deployment; however, for increased performance, future SLiMSat designs should incorporate dynamic rollers moving transversely to apply a constant force to the beam, retaining the stowed portion on the hub throughout deployment.
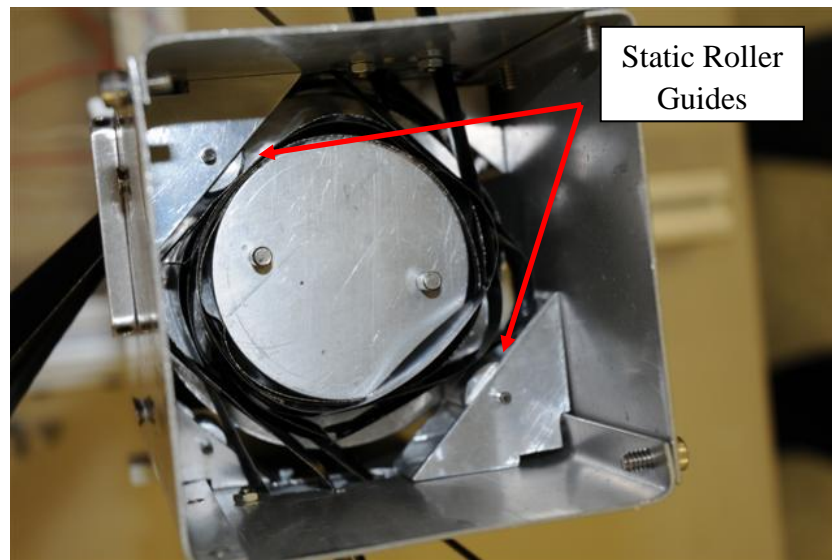
Figure 104. SLiMSat Hub with Static Roller Guides

5.4 Future Work and Recommendations

Each limiting factor can be categorized as an obstacle in the path of a particular objective, namely: obstacles to effective testing, obstacles to accurate modeling, and obstacles to functional boom deployment. The obstacles to successful testing involve the ambitious selection of the 4m boom size for testing, the excitation source scalloping and the difficulty in obtaining adequate coherence values for much of the analyzed frequency spectrum. The extremely large boom was exceptionally susceptible to ambient vibrations, and made full beam modal motion impossible to detect within the laboratory for even a single dimension. Future groups should consider using a smaller section of beam less than a meter in length to decrease the sensitivity of the beam to ambient vibrations as well as facilitating the capture of the entire beam mode shape. Using two alternating electromagnets, data scalloping of the frequency response could be potentially eliminated or at least better characterized. In addition, constructing smaller boom test sections would be less expensive allowing the testing of multiple boom fixation methods.

In response to the encountered testing challenges and in order to facilitate future tests, a comprehensive list of testing recommendations was developed.

- Construct booms from 0.004" thick 17-7 Stainless Steel as recommended by Banik at AFRL(Banik J. , 2008).
- Make all cuts and modifications to the booms prior to heat treatment if possible (with the exception of the laser welding which should occur last).
- Test short section of TRAC boom before moving to larger sections.
- Use a Single Head Laser Vibrometer in multiple orientations rather than the Triple-Head Laser Vibrometer in a fixed location.
- Excite the beam with an electromagnet or possibly multiple magnets.
- Have multiple booms test sections to allow simultaneous vibration, reflectivity, and deployment testing.
- Construct dynamic rollers that apply a constant force to the stowed beams within the satellite for increased deployment performance.

By following the aforementioned guidelines, future analyst will rapidly develop sufficient test results governing the dynamic behavior of the TRAC booms themselves, and whatever boom-end design they decide to employ.

The current obstacles to successful modeling are identified as lack of a finalized prototype design. The design process is inherently iterative, and SLiMSat, with its multiple deployed booms, membrane and rotating parts, was no exception. Design development continues until the present as unforeseen issues are resolved as they occur. Models of SLiMSat, however, are only instructive as long as they approximate the actual

133

structure of the satellite. Therefore, only the TRAC booms themselves were modeled as iterative prototype development of the entire satellite prohibited timely model creation and analysis. However, now that a functioning prototype has been developed, the work of finite element analysis can truly begin.

In order to conduct future deployments several key parameters still warrant investigation. The boom material selection itself once again merits attention. Laser-welded commercial unpainted tapespring is clearly unsuited for multiple deployments. Degradation of the booms is instigated as the booms transition into their stowed configuration with boom fractures occurring in and around the third test deployment. Booms constructed from known materials and heat treated to a lower hardness or stress relieved, should provide better performance. In addition, significant difficulty was incurred in the decision to deploy large reflective structures at the extents of these deployable booms. The determined optical resolution required for ground-based observation required that the reflective surfaces themselves be placed as far away from one another as possible. Based on the design of NASA's Nanosail-D, reflective surfaces, located at the ends of four booms, deployed from a central hub seemed logical. However there are, perhaps, easier methods to obtain an optical baseline displacement. One suggestion of particular merit is that of a central 1U CubeSat hub connected via TRAC booms to two other 1U hubs forming a barbell-like structure. The farthest CubeSats could then deploy reflective membranes from a solid 1U chassis rather than at the end of an extremely flexible beam. In addition, by incorporating a thin wire into the TRAC beam structure, power loads and sensor requirements could be shared by all three

CubeSat units. The deployed reflective surfaces would also be easier to manipulate and control providing a more natural precursor to augmenting CubeSats with parabolic dishes where knowledge of the exact geometry parameters are required.

Optical tests and optimization studies of the membranes still remain in order to determine the optical imaging of the satellite on the ground. The SLiMSat FE model will be a valuable resource in predicting dynamic optical behavior, as well as the adherence to the general guideline of prototyping as early and often as practicable.

5.5 Summary

In this thesis, the TRAC boom natural frequencies and deflection shapes were identified for later reference. The specific testing difficulties regarding the dynamic testing of TRAC boom was uncovered, and recommendations were developed to speed future tests. Additionally, the novel 'Frogleg' boom-end design to deploy membranes on booms away from the central body of the satellite was explored as a viable design concept.

Ultimately, the body of research represented in the development of SLiMSat simultaneously promotes and elucidates the fundamental aspects of small satellite innovation. Irrefutably, SLiMSat stands alone among CubeSats; a novel deployable boom concept which provides the critical first step in the integration of deployable boom technology into the CubeSats form factor here at AFIT.

Appendix

Figure 105 and Figure 106 are one-dimensional FRFs of all scanned points along the beam excited using the electromagnet using a chirp input from 0 to 25 Hz, 10 complex averages, Hanning window and 50% overlap.
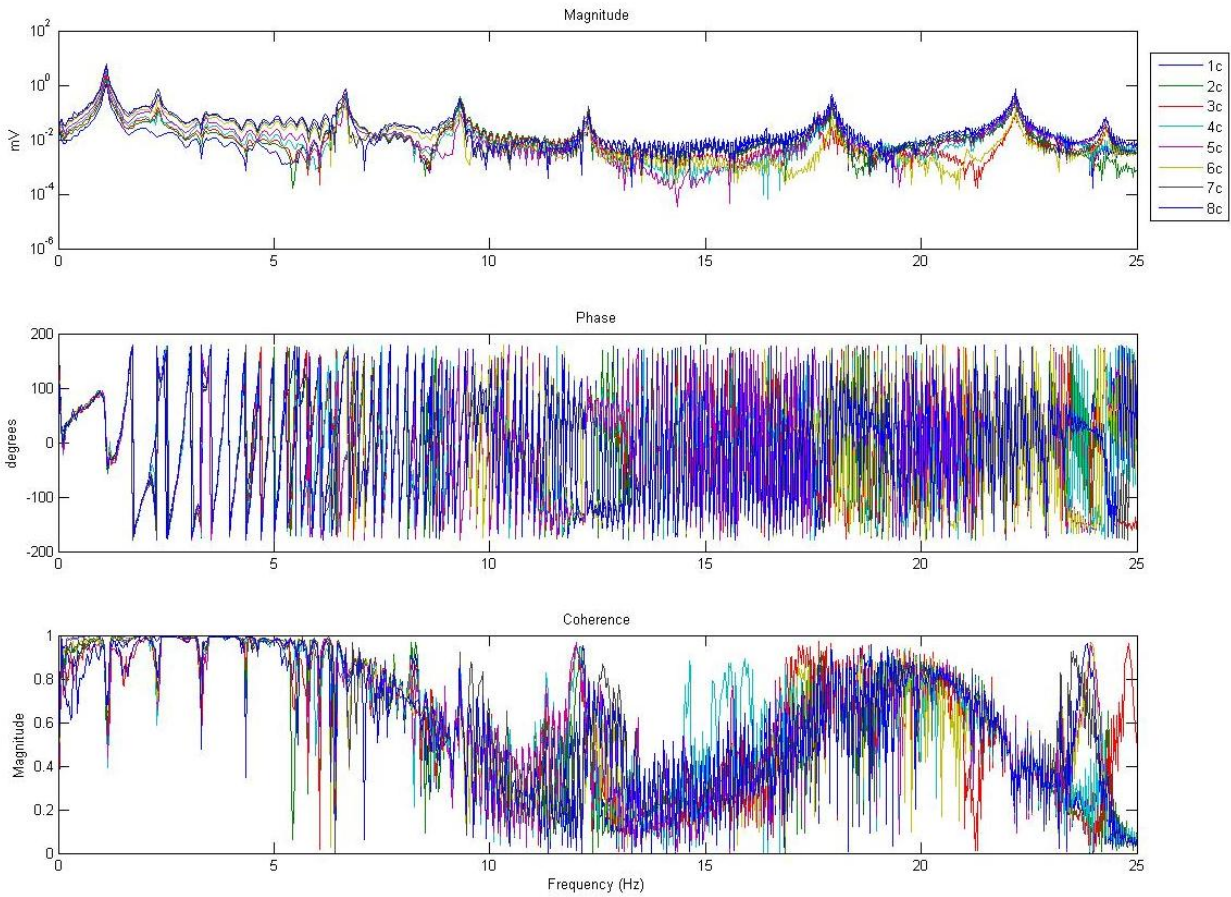
Figure 105. FRF of points along Right side of Beam
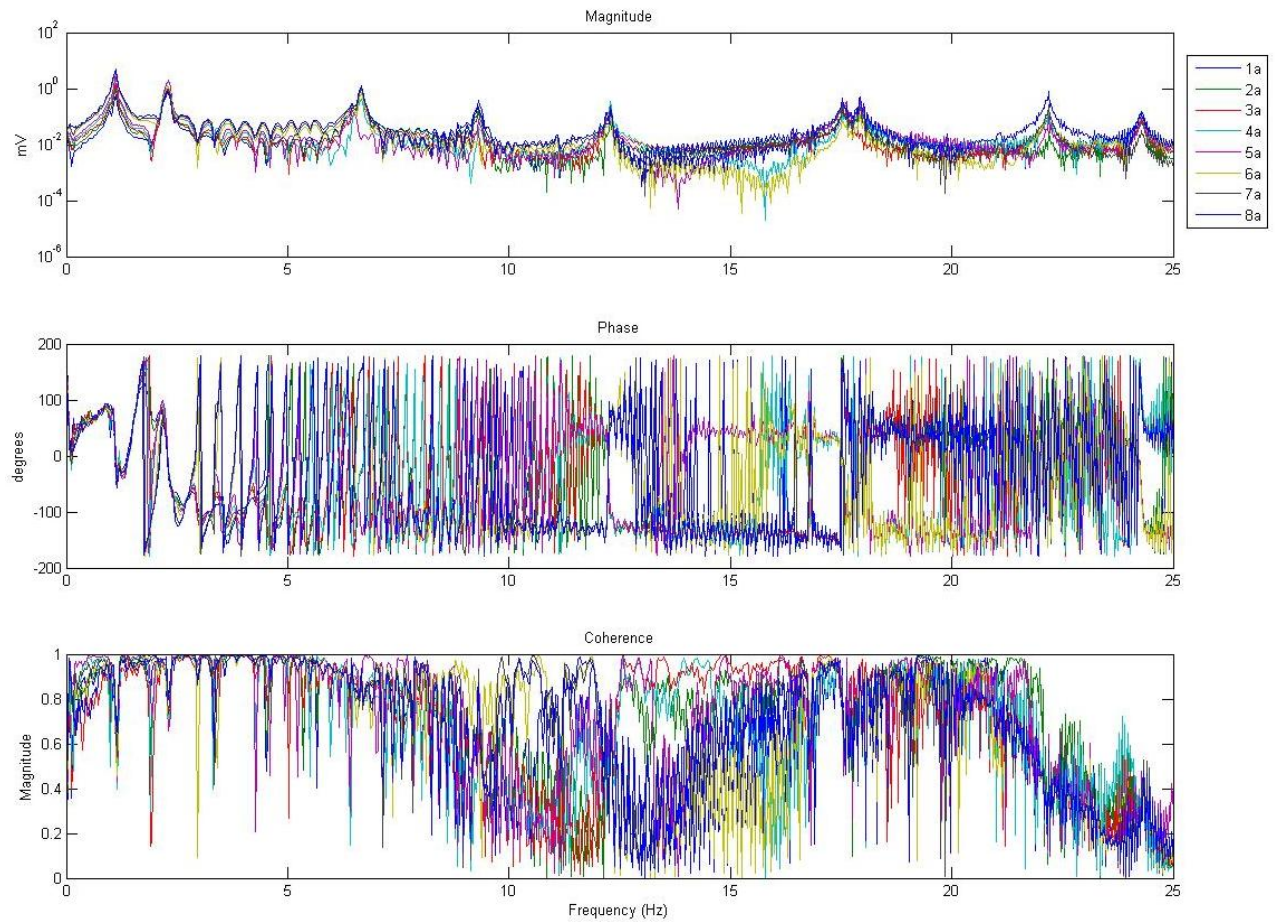
Figure 106. FRF of points along Left side of Beam

Figure 107 through Figure 112 are complex plots of the Eigenvectors calculated from the FRF magnitude and phase values at each natural frequency of the scanned data points along the vertically hung beam. The central black line in each plot is the idealized Eigenvector plot line while the red lines represent one standard deviation, in phase, away in either direction from that trendline. Presumably, the points farthest away from the origin are those with the highest signal to noise ratio and are therefore, weigh heaviest into the calculation of the average phase trendline.
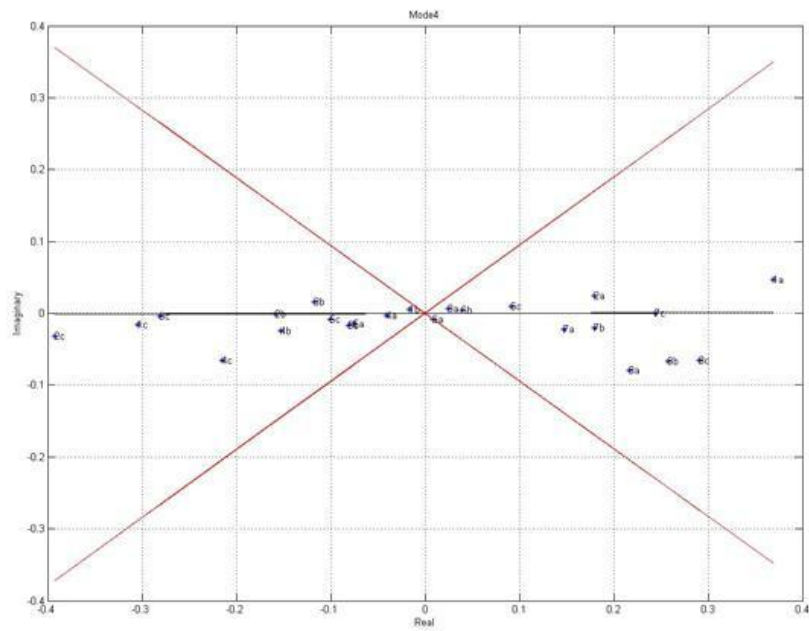
Figure 107. Mode 4 Complex Plot of Eigenvector

Figure 108. Mode 5 Complex Plot of Eigenvector

138

Figure 109. Mode 6Complex Plot of Eigenvector
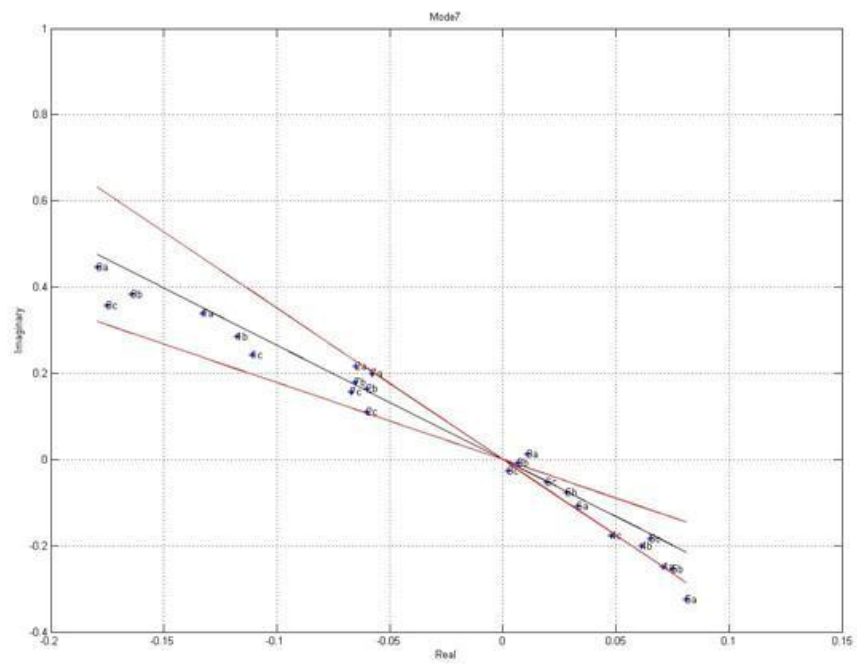
Figure 110. Mode 7 Complex Plot of Eigenvector

139
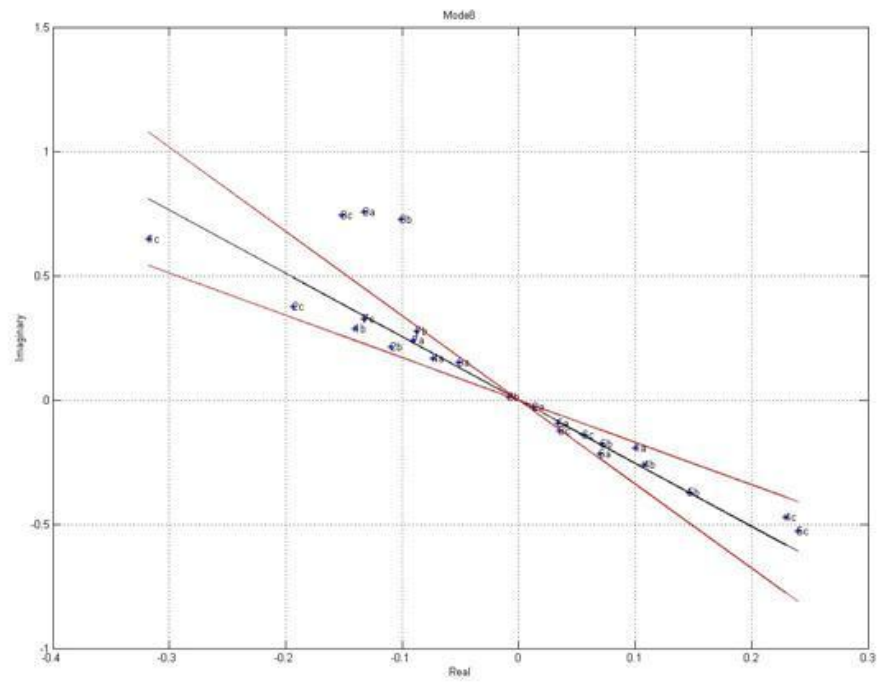
Figure 111. Mode 8 Complex Plot of Eigenvector
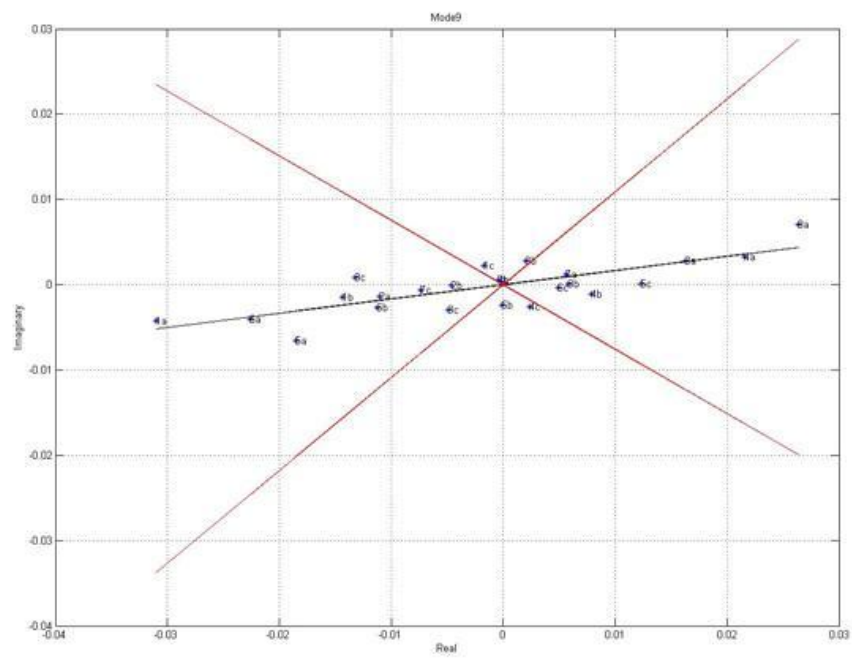
Figure 112. Mode 9 Complex Plot of Eigenvector

140

The Matlab code used to develop and process the mode shape movies and various plots found in this document is included below for reference.

```
% Experimental Mode Shape Movie Generator
close all;
clear all;
clc;

%% Load frf, frequency, coherence and meas point postions along beam
load 'frf.mat' %801x24 matrix (rows:complex mag&phase at each freq bin,
col:points from 1a,b,c...8,a,b,c)pulled from single head laser data
load 'FreqV.mat'%801x1 distinct frequency bins
load 'coher.mat'%801x24 coherence values for each entry in frf


b = 0.15
data in .dat file has the following implicit headings
L    h    r    x    y    theta (degrees) cos(theta)   z
 L = vert. height of laser from the ground
 r = horiz. distance from laser to the beam
 h = vert. distance of meas point from ground
 x = horiz. distance of meas point from left side of the beam
 y = horiz. distance of meas point from right side of the beam
 b = vert. distance from tip of beam to ground
 theta = angle(deg)that laser head makes with horiz (calculated from
geometry in excel)
 z = vert distance of meas point from the fixed end of the beam
*all distances are in inches and angles are in degrees*

data = load('boom_indices.dat'); %load data from text file
%% Arrange 2D meas point positions into a more sensical format
%2D Positions(in) of each meas point along beam considering the center
of fixed end of the beam to be (0,0)
width = 1;      %horiz. chordal width of beam
x = data(:,4);  %horiz. distances of meas points from left side of the
beam
y = data(:,5);  %horiz. distances of meas points from right side of the
beam
z = data(:,8);  %vert distances of meas points from the fixed end of
the beam

%Each meas point has EITHER an x or a y value not both
%Give "a" and "c" points a location rel. to the center of the beam
rather than the edge
for ctr=1:3:24
    x(ctr,1)=(width/2)-x(ctr,1);
end
for ctr=3:3:24
    y(ctr,1)=-(width/2)+y(ctr,1);
end
pos = x + y;
%24x2 matrix of 2D meas. point locations with origin at the center of
the fixed end
TWO_Dpoints = [pos z];
```
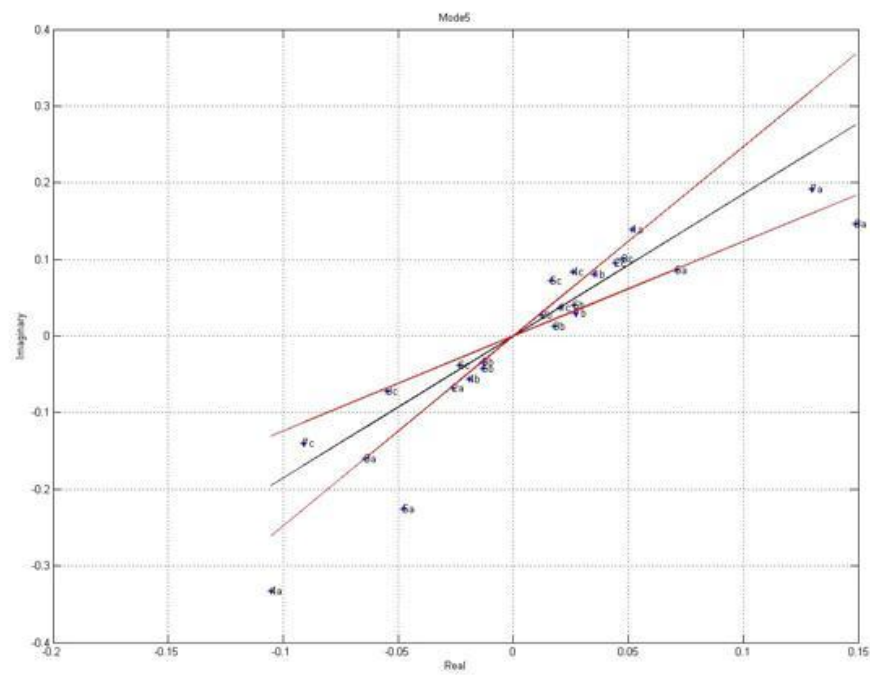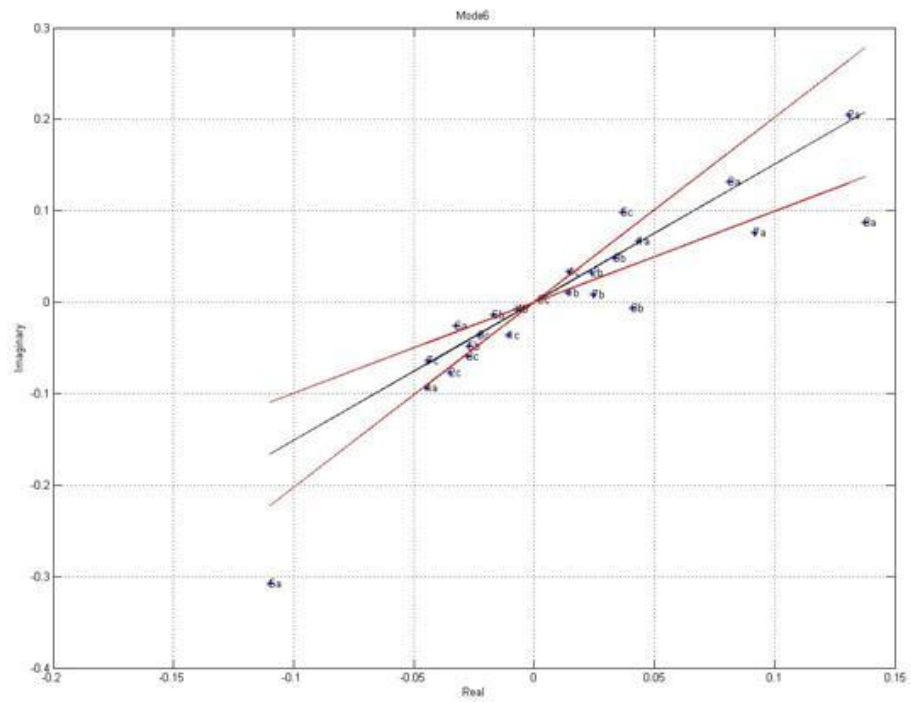
```matlab
%% Plot FRFs
R = abs(frf);                   %R = mag of entire frf (all points, all
freqs)
theta = rad2deg(angle(frf));    %theta = phase(deg) of entire frf (all
points, all freqs)

%Correct for laser head angle
% scales mag of response by a cos factor calculated from geometry
for ctr=1:24
Rscaled(:,ctr) = R(:,ctr).*data(ctr,7);
end
%
Plot frf's(mag,phase) & coherence for all points along the beam based
on position
ctr=1;
for ctr=1:3:24
    figure
    subplot(3,1,1);

semilogy(FreqV(:,1),Rscaled(:,ctr),FreqV(:,1),Rscaled(:,ctr+1),FreqV(:,
1),Rscaled(:,ctr+2));
    title(['Points ',num2str(ctr),'a,b,&c','    Magnitude'])
    %title({'Points ';'Magnitude'})
    legend('a','b','c')
    subplot(3,1,2);

plot(FreqV(:,1),theta(:,ctr),FreqV(:,1),theta(:,ctr+1),FreqV(:,1),theta
(:,ctr+2));
    title('Phase')
    legend('a','b','c')
    subplot(3,1,3);

plot(FreqV(:,1),coher(:,ctr),FreqV(:,1),coher(:,ctr+1),FreqV(:,1),coher
(:,ctr+2));
    title('Coherence')
    legend('a','b','c')
    ctr=ctr+1;
end

%Plot frf's(mag,phase) & coherence for all "b" points along the center
of
%the beam
figure('Color',[1 1 1]);
 subplot(3,1,1);
 %subplot(2,1,1);

semilogy(FreqV(:,1),Rscaled(:,2),FreqV(:,1),Rscaled(:,5),FreqV(:,1),Rsc
aled(:,8),FreqV(:,1),Rscaled(:,11),FreqV(:,1),Rscaled(:,14),FreqV(:,1),
Rscaled(:,17),FreqV(:,1),Rscaled(:,20),FreqV(:,1),Rscaled(:,23));
 legend1 = legend('1b','2b','3b','4b','5b','6b','7b','8b');
 set(legend1,'Position',[0.9168 0.7247 0.05 0.192]);
 title({'Points along the center of the beam';'Magnitude'})
 ylabel('mV')
 subplot(3,1,2);
```

```matlab
%subplot(2,1,2);

plot(FreqV(:,1),theta(:,2),FreqV(:,1),theta(:,5),FreqV(:,1),theta(:,8),
FreqV(:,1),theta(:,11),FreqV(:,1),theta(:,14),FreqV(:,1),theta(:,17),Fr
eqV(:,1),theta(:,20),FreqV(:,1),theta(:,23));
 title('Phase')
 ylabel('degrees')
 subplot(3,1,3);
%subplot(2,1,2);

plot(FreqV(:,1),coher(:,2),FreqV(:,1),coher(:,5),FreqV(:,1),coher(:,8),
FreqV(:,1),coher(:,11),FreqV(:,1),coher(:,14),FreqV(:,1),coher(:,17),Fr
eqV(:,1),coher(:,20),FreqV(:,1),coher(:,23));
 title('Coherence')
 ylabel('Magnitude')
 xlabel('Frequency (Hz)')

%Plot frf's(mag,phase) & coherence for all "a" points along the left
side of
%the beam
figure('Color',[1 1 1]);
 subplot(3,1,1);

semilogy(FreqV(:,1),Rscaled(:,1),FreqV(:,1),Rscaled(:,4),FreqV(:,1),Rsc
aled(:,7),FreqV(:,1),Rscaled(:,10),FreqV(:,1),Rscaled(:,13),FreqV(:,1),
Rscaled(:,16),FreqV(:,1),Rscaled(:,19),FreqV(:,1),Rscaled(:,22));
 legend1 = legend('1a','2a','3a','4a','5a','6a','7a','8a');
 set(legend1,'Position',[0.9168 0.7247 0.05 0.192]);
 title('Magnitude')
 ylabel('mV')
 subplot(3,1,2);

plot(FreqV(:,1),theta(:,1),FreqV(:,1),theta(:,4),FreqV(:,1),theta(:,7),
FreqV(:,1),theta(:,10),FreqV(:,1),theta(:,13),FreqV(:,1),theta(:,16),Fr
eqV(:,1),theta(:,19),FreqV(:,1),theta(:,22));
 title('Phase')
 ylabel('degrees')
 subplot(3,1,3);

plot(FreqV(:,1),coher(:,1),FreqV(:,1),coher(:,4),FreqV(:,1),coher(:,7),
FreqV(:,1),coher(:,10),FreqV(:,1),coher(:,13),FreqV(:,1),coher(:,16),Fr
eqV(:,1),coher(:,19),FreqV(:,1),coher(:,22));
 title('Coherence')
 ylabel('Magnitude')
 xlabel('Frequency (Hz)')
%Plot frf's(mag,phase) & coherence for all "b" points along the right
side of
%the beam
figure('Color',[1 1 1]);
 subplot(3,1,1);

semilogy(FreqV(:,1),Rscaled(:,3),FreqV(:,1),Rscaled(:,6),FreqV(:,1),Rsc
aled(:,9),FreqV(:,1),Rscaled(:,12),FreqV(:,1),Rscaled(:,15),FreqV(:,1),
Rscaled(:,18),FreqV(:,1),Rscaled(:,21),FreqV(:,1),Rscaled(:,24));
 legend1 = legend('1c','2c','3c','4c','5c','6c','7c','8c');
```

143

```
 set(legend1,'Position',[0.9168 0.7247 0.05 0.192]);
 title('Magnitude')
 ylabel('mV')
 subplot(3,1,2);

plot(FreqV(:,1),theta(:,3),FreqV(:,1),theta(:,6),FreqV(:,1),theta(:,9),
FreqV(:,1),theta(:,12),FreqV(:,1),theta(:,15),FreqV(:,1),theta(:,18),Fr
eqV(:,1),theta(:,21),FreqV(:,1),theta(:,24));
 title('Phase')
 ylabel('degrees')
 subplot(3,1,3);

plot(FreqV(:,1),coher(:,3),FreqV(:,1),coher(:,6),FreqV(:,1),coher(:,9),
FreqV(:,1),coher(:,12),FreqV(:,1),coher(:,15),FreqV(:,1),coher(:,18),Fr
eqV(:,1),coher(:,21),FreqV(:,1),coher(:,24));
 title('Coherence')
 ylabel('Magnitude')
 xlabel('Frequency (Hz)')


% Plot head-on look at meas points
for ctr=1:160
    q(ctr,1)=-ctr;
    q(ctr,2)=width/2;
    q(ctr,3)=-width/2;
end
b = [TWO_Dpoints(:,1) -TWO_Dpoints(:,2)];
%
figure('Color',[1 1 1]);
plot(b(:,1),b(:,2),'*r','MarkerSize',10)
    text(b(1,1),b(1,2),'1c','Position',[0.2692 -58.34 17.32]);
    text(b(2,1),b(2,2),'1b','Position',[-0.1 -58.6 17.32]);
    text(b(3,1),b(3,2),'1a','Position',[-0.4538 -58.34 17.32]);
    text(b(4,1),b(4,2),'2c','Position',[0.2538 -70.83 17.32]);
    text(b(5,1),b(5,2),'2b','Position',[-0.08462 -70.56 17.32]);
    text(b(6,1),b(6,2),'2a','Position',[-0.3923 -70.3 17.32]);
    text(b(7,1),b(7,2),'3c','Position',[0.2538 -83.06 17.32]);
    text(b(8,1),b(8,2),'3b','Position',[-0.08462 -83.06 17.32]);
    text(b(9,1),b(9,2),'3a','Position',[-0.4231 -82.79 17.32]);
    text(b(10,1),b(10,2),'4c','Position',[0.2385 -98.21 17.32]);
    text(b(11,1),b(11,2),'4b','Position',[-0.1 -98.21 17.32]);
    text(b(12,1),b(12,2),'4a','Position',[-0.4231 -97.67 17.32]);
    text(b(13,1),b(13,2),'5c','Position',[0.2538 -112.3 17.32]);
    text(b(14,1),b(14,2),'5b','Position',[-0.1154 -112 17.32]);
    text(b(15,1),b(15,2),'5a','Position',[-0.4538 -111.8 17.32]);
    text(b(16,1),b(16,2),'6c','Position',[0.2231 -130.6 17.32]);
    text(b(17,1),b(17,2),'6b','Position',[-0.08462 -130.6 17.32]);
    text(b(18,1),b(18,2),'6a','Position',[-0.4231 -130.6 17.32]);
    text(b(19,1),b(19,2),'7c','Position',[0.2231 -143.4 17.32]);
    text(b(20,1),b(20,2),'7b','Position',[-0.08462 -143.1 17.32]);
    text(b(21,1),b(21,2),'7a','Position',[-0.4538 -143.1 17.32]);
    text(b(22,1),b(22,2),'8c','Position',[0.2231 -154.6 17.32]);
    text(b(23,1),b(23,2),'8b','Position',[-0.1154 -154.6 17.32]);
    text(b(24,1),b(24,2),'8a','Position',[-0.4538 -154.6 17.32]);
axis([-2 2 -160 0])
```

```matlab
hold on
plot(q(:,2),q(:,1),'b',q(:,3),q(:,1),'b')

%% Derive Mode shapes
% Derive nat freqs manually by looking at plots and determining what
the
% freqs are at each peak.  Then look at frf.mat and find the index that
% corresponds to the determined nat freqs.
Eigenvalues = [1.125 2.313 6.656 9.313 12.28 17.59 17.91 22.19 24.28]';

% Create 2 matrices of mag&phase at each point for the specified
natural freqs by picking
% off only the rows that correspond to the index of where eigenvalues
are
% found
mags = [Rscaled(37,:); Rscaled(75,:); Rscaled(211,:); Rscaled(299,:);
Rscaled(394,:); Rscaled(564,:); Rscaled(574,:); Rscaled(711,:);
Rscaled(788,:)];
phase = [theta(37,:); theta(75,:); theta(211,:); theta(299,:);
theta(394,:); theta(564,:); theta(574,:); theta(711,:); theta(788,:)];
F = [frf(37,:); frf(75,:); frf(211,:); frf(299,:); frf(394,:);
frf(564,:); frf(574,:); frf(711,:); frf(788,:)];
rpart = real(F);
ipart = imag(F);

%Assume points with largest magnitude displacement also have largest
signal
%to noise ratio

%find max values of F
mx = max(abs(F'));
G = abs(F');
%Normalize F to those values to create Fn
for c=1:9
    Fn(:,c) = G(:,c)/mx(1,c);
end

%avg phase angle is p(1) of best fit
for c=1:9
    po(c,:)=polyfit(rpart(c,:),ipart(c,:),1);
end

%convert phase matrix from deg to rads
radPhase = phase*pi/180;
radPhase = radPhase';


for c=1:9
    nphase(:,c) = radPhase(:,c).*Fn(:,c);
end

%calc std dev for each eigenvector line
std_dev = std(nphase)';
```

```matlab
maximum = po(:,1) + std_dev(:,1);
minimum = po(:,1) - std_dev(:,1);

radPhase = radPhase';

%% Plot frf points on complex plane
%
v = linspace(0,2*pi,50);
for c=3:3
    figure('Color',[1 1 1]);
    plot(rpart(c,:),ipart(c,:),'*b')
    text(rpart(c,1),ipart(c,1),'1a');
    text(rpart(c,2),ipart(c,2),'1b');
    text(rpart(c,3),ipart(c,3),'1c');
    text(rpart(c,4),ipart(c,4),'2a');
    text(rpart(c,5),ipart(c,5),'2b');
    text(rpart(c,6),ipart(c,6),'2c');
    text(rpart(c,7),ipart(c,7),'3a');
    text(rpart(c,8),ipart(c,8),'3b');
    text(rpart(c,9),ipart(c,9),'3c');
    text(rpart(c,10),ipart(c,10),'4a');
    text(rpart(c,11),ipart(c,11),'4b');
    text(rpart(c,12),ipart(c,12),'4c');
    text(rpart(c,13),ipart(c,13),'5a');
    text(rpart(c,14),ipart(c,14),'5b');
    text(rpart(c,15),ipart(c,15),'5c');
    text(rpart(c,16),ipart(c,16),'6a');
    text(rpart(c,17),ipart(c,17),'6b');
    text(rpart(c,18),ipart(c,18),'6c');
    text(rpart(c,19),ipart(c,19),'7a');
    text(rpart(c,20),ipart(c,20),'7b');
    text(rpart(c,21),ipart(c,21),'7c');
    text(rpart(c,22),ipart(c,22),'8a');
    text(rpart(c,23),ipart(c,23),'8b');
    text(rpart(c,24),ipart(c,24),'8c');
    xlabel('Real')
    ylabel('Imaginary')
    title(['Mode', num2str(c)])
    hold on
    grid on
    %axis square;
    plot(rpart(c,:),po(c,1)*rpart(c,:),'k');
    hold on;
    plot(rpart(c,:),maximum(c,1)*rpart(c,:),'r');
    hold on;
    plot(rpart(c,:),minimum(c,1)*rpart(c,:),'r');
    hold on;
end

%% Factor graphs

%Adjust mag at natural freq to correct for phase
```

```
% The "factor" is the phase magnitude we will add to each phase point
to
% rotate the arcs of the phases (of unit magnitude) to be centered on
+1
% and -1 on a polar plot.
%
%Factor is calculated in two parts:
%   The "1st part" will calculate the magnitude of the factor, and the
% "2nd part" will calculate whether the factor needs to added or
%   subtracted in order to center the arcs
%
%1st part
%   abs(radphase)=> make all angles(of a particular row) positive (flips
angles up over x-axis)
%   cos(above)   => takes projection along x-axis
%   abs(above)   => moves all points to positions along x-axis in RHP
%   mean(above)  => takes average of all those points
%   acos(above)  => finds angle required for that given average cos
ratio
%
%2nd part
%   tan(radPhase) => collapses angles onto 45deg line which will be
either
%    in the upper-right(+) or lower-left(-) quadrants
%   mean(above)   => takes average value
%   sign(above)   => gives 1 if >0, or -1 if <0
%
% Multiplying the first part times the second gives "factor" the
% appropriate sign so that its application will always rotate the
center of
% the arcs to +1 and -1 respectively
%
%   radPhase-factor  => rotates center of arcs to +1 and -1
%   cos(above)       => takes projection along x-axis
%   sign(above)      => gives +1 or -1 for values >0 or <0
%   mags *(above)     => makes magnitudes that are 180 out of phase
negative
%
% using "factor" ensures that no matter how spread out the phase arcs
are,
% the proper sign will applied to the mag data

close all
for a=1:size(phase,1)
    factor =
acos(mean(abs(cos(abs(radPhase(a,:))))))*sign(mean(tan(radPhase(a,:))))
;
    figure('Color',[1 1 1]);
    rlim = max(mags(a,:));
    for b=1:size(phase,2)
        mags(a,b) = mags(a,b)*sign(cos(radPhase(a,b) - factor));
        checkVar = radPhase(a,b) - factor;
%       polar(checkVar,mags(a,b),'*b')
        polar(checkVar,1,'*b')
%       axis([-1 1 -1 1]*rlim);
```

147

```matlab
        hold on
%       polar(radPhase(a,b),mags(a,b),'or')
        polar(radPhase(a,b),1,'or')
        %text(cos(radPhase(a,b)),sin(radPhase(a,b)),num2str(b))
        title(['Mode',num2str(a),'       Factor = ',
num2str(factor*180/pi)])
        hold on
%       legend('After','Before',-1)
    end
end

%Create matrix of magnitudes for later comparision
meas_mags = mags';
meas_maximum = max(abs(meas_mags));
%meas_maximum = [22,22,22,22,22,1,22,22,22,22;];
for ctr=1:9
    meas_normalized(:,ctr) = meas_mags(:,ctr)./meas_maximum(:,ctr);
end
measured = meas_normalized;
mags = measured';


%% Build "A" matrix
t = linspace(0,2*pi,24);
%scale =[1 .75 1 .75 .75 .5 .5 .5 .35 1]';
scale = [1 1 1 1 1 1 1 1 1 1]';
A = zeros(216,24);
ctr = 0;
for b=1:9
    for j=1:24;
        ctr = ctr + 1;
        A(ctr,:) = (mags(b,j)*cos(t)).*scale(b,1);
    end
end

Opp = -1.*A;

%% Mode Shape movies

zTrof = -0.2;

for j=0:24:(216-24)
    for i=1:24
      Vec(j+i,1:2) = TWO_Dpoints(i,1:2);
    end
end
Vec(:,2)= -Vec(:,2);
A = [Vec A];
Opp = [Vec Opp];

A([2:3:215],3:end) = A([2:3:215],3:end) + zTrof;
Opp([2:3:215],3:end) = Opp([2:3:215],3:end) + zTrof;
```

148

```matlab
screen_size = get(0, 'ScreenSize');

%close all
for modeNum = 1:1
    clear z
    f1 = figure('Color',[1 1 1]);
    set(f1, 'Position', [0 0 screen_size(3) screen_size(4) ] );
    for i=3:26
        zCtr = (modeNum-1)*24+1;
        for y = 1:8
            for x = 1:3
                z(y,x) = A(zCtr,i);
                zCtr = zCtr + 1;
            end
        end
        x = A(1:3,1)';
        y = A(1:3:24,2);
        rangeX=linspace(-.6,.6,20);
        rangeY=linspace(-170,-50,100);
        [X,Y]=meshgrid(rangeX,rangeY);
%         Z = interp2(x,y,z,X,Y,'cubic');
%
mesh(X,Y,Z,'FaceLighting','phong','LineStyle','none','FaceColor',[0 0
0]);
        Z=griddata(x,y,z,X,Y);
        hold off;

%surf(X,Y,Z,'FaceLighting','phong','LineStyle','none','FaceColor',[0 0
1]);
        surf(X,Y,Z,'FaceLighting','phong','FaceColor','none');
        hold on;
        r = TWO_Dpoints(:,1);
        p = -TWO_Dpoints(:,2);
        q = reshape(z',24,1);
        plot3(r,p,q,'*r','MarkerSize',8)
        light('Position',[-0.5015 0.01989 0.8649]);
        axis([-1 1 -160 0 -1 1])
        title(['Measured Mode ' num2str(modeNum),'   at '
num2str(Eigenvalues(modeNum,1)) 'Hz','   scale factor = '
num2str(scale(modeNum,1))])
        daspect([1 12 1])
        mode(i-2) = getframe;
    end
    movie(mode,1,24)
    movie2avi(mode, ['Mode' num2str(modeNum) '.avi'],
'compression','Cinepak');
end

save 'A';
save 'measured';
save 'I';


% Theoretical Mode Shape Movie Generator
```

```matlab
close all;
clear all;
clc;

%single_6.pch
[modes eigenvalues GRIDID] = pchread_all('slims002.pch');

nat_freq = sqrt(eigenvalues(1,:))/(2*pi);

num_modes = size(modes,2);

for ctr=1:24
    Xo(ctr,:) = modes(((ctr-1)*3)+1,:);
end

for ctr=1:24
    Yo(ctr,:) = modes(((ctr-1)*3)+2,:);
end

for ctr=1:24
    Zo(ctr,:) = modes(((ctr-1)*3)+3,:);
end

theta = 25;%degrees
theta = deg2rad(theta);

Xt = Xo.*cos(theta);
Yt = Yo.*sin(theta);

M = Xt + Yt;
Mpre_normal = M;

figure
plot(M(1:3:end,1))
hold on
plot(M(2:3:end,1))
hold on
plot(M(3:3:end,1))

figure
plot(M(1:3:end,2))
hold on
plot(M(2:3:end,2))
hold on
plot(M(3:3:end,2))

figure
plot(M(1:3:end,3))
hold on
plot(M(2:3:end,3))
hold on
plot(M(3:3:end,3))
```

```matlab
figure
plot(M(1:3:end,4))
hold on
plot(M(2:3:end,4))
hold on
plot(M(3:3:end,4))

figure
plot(M(1:3:end,5))
hold on
plot(M(2:3:end,5))
hold on
plot(M(3:3:end,5))
%% Normalized to measured data points

%col indices of maximums from meaured data

%J = [21,13,22,7,10,13,22,22,1,1];
[J,I] = max(abs(M));
% for ctr=1:10
%     maximum(1,ctr)=abs(M(J(1,ctr),ctr));
% end
for ctr=1:num_modes
    %Theo_normalized(:,ctr) = M(:,ctr)./maximum(:,ctr);
    Theo_normalized(:,ctr) = M(:,ctr)./J(:,ctr);
end


% Correct for possible 180 shift of eigenvector from measured data
%Theo_normalized(:,3) = -Theo_normalized(:,3)

Theo_normalized = Theo_normalized';


figure
plot(Normalized(1:3:end,1))
hold on
plot(Normalized(2:3:end,1))
hold on
plot(Normalized(3:3:end,1))

figure
plot(Normalized(1:3:end,2))
hold on
plot(Normalized(2:3:end,2))
hold on
plot(Normalized(3:3:end,2))
%% Build B matrix

t = linspace(0,2*pi,24);
scale = ones(24,1);
B = zeros(24*num_modes,24);
ctr = 0;
```

```matlab
for b=1:num_modes
    for j=1:24
        ctr = ctr + 1;
        B(ctr,:) = (Theo_normalized(b,j)*cos(t)).*scale(b,1);
    end
end
model = Theo_normalized';
zTrof = -0.2;
positions = load('positions.dat');

for j=0:24:((num_modes*24)+4-24)
    for i=1:24
      V(j+i,1:2) = positions(i,1:2);
    end
end
V(:,2)= -V(:,2);
B = [V B];

B([2:3:end],3:end) = B([2:3:end],3:end) + zTrof;

screen_size = get(0, 'ScreenSize');

%close all
for modeNum = 1:1
    clear x y z
    f1 = figure;
    set(f1, 'Position', [0 0 screen_size(3) screen_size(4) ] );
    for i=3:26
        zCtr = (modeNum-1)*24+1;
        for y = 1:8
            for x = 1:3
                z(y,x) = B(zCtr,i);
                zCtr = zCtr + 1;
            end
        end
        x = B(1:3,1)';
        y = B(1:3:24,2);
        rangeX=linspace(-.6,.6,20);
        rangeY=linspace(-170,-50,100);
        [X,Y]=meshgrid(rangeX,rangeY);
%       Z = interp2(x,y,z,X,Y,'cubic');
%
mesh(X,Y,Z,'FaceLighting','phong','LineStyle','none','FaceColor',[0 0
0]);
        Z=griddata(x,y,z,X,Y);
        hold off;

%surf(X,Y,Z,'FaceLighting','phong','LineStyle','none','FaceColor',[0 0
1]);
        surf(X,Y,Z,'FaceLighting','phong','FaceColor','none');
        hold on;
        s = positions(:,1);
        t = -positions(:,2);
        u = reshape(z',24,1);
```

152

```matlab
        plot3(s,t,u,'MarkerFaceColor',[0 0
1],'MarkerSize',8,'Marker','o',...
            'LineStyle','none','Color',[0 0 1]);
        axis([-1 1 -160 0 -1 1])
        title(['Theoretical Mode ' num2str(modeNum),'   at '
num2str(nat_freq(1,modeNum)) 'Hz','   scale factor = '
num2str(scale(modeNum,1))])
        daspect([1 12 1])
        mode(i-2) = getframe;
    end
    movie(mode,3,24)
    %movie2avi(mode, ['Mode' num2str(modeNum) '.avi'],
'compression','Cinepak');
end


save 'B';
save 'positions';
save 'model';

_____
%% Merged Theoretical and Measured data Movie Generator
clc;
clear all;
close all;

screen_size = get(0, 'ScreenSize');
load 'A.mat';
load 'B.mat';

model_mode =[1 3 4 5 6 7 8 9 10];

for modeNum = 1:1
    modelNum = model_mode(1,modeNum);
    clear z
    f1 = figure;
    set(f1, 'Position', [0 0 screen_size(3) screen_size(4) ] );
    for i=3:26
        zCtr = (modeNum-1)*24+1;
        zzCtr = (modelNum-1)*24+1;
        for y = 1:8
            for x = 1:3
                z(y,x) = A(zCtr,i);
                zz(y,x) = B(zzCtr,i);
                zCtr = zCtr + 1;
                zzCtr = zzCtr + 1;
            end
        end
        x = A(1:3,1)';
        y = A(1:3:24,2);
        rangeX=linspace(-.6,.6,20);
        rangeY=linspace(-170,-50,100);
        [X,Y]=meshgrid(rangeX,rangeY);
%       Z = interp2(x,y,z,X,Y,'cubic');
```

153

```matlab
%
mesh(X,Y,Z,'FaceLighting','phong','LineStyle','none','FaceColor',[0 0
0]);
        Z=griddata(x,y,z,X,Y);
        hold off;

%surf(X,Y,Z,'FaceLighting','phong','LineStyle','none','FaceColor',[0 0
1]);
        surf(X,Y,Z,'FaceLighting','phong','FaceColor','none');
        hold on;
        s = positions(:,1);
        t = -positions(:,2);
        u = reshape(zz',24,1);
        plot3(s,t,u,'MarkerFaceColor',[0 0
1],'MarkerSize',8,'Marker','o',...
                'LineStyle','none','Color',[0 0 1]);
        light('Position',[-0.5015 0.01989 0.8649]);
        axis([-1 1 -160 0 -1 1])
        title(['Measured Mode ' num2str(modeNum),'   at '
num2str(Eigenvalues(modeNum,1)) 'Hz','    scale factor = '
num2str(scale(modeNum,1))])
        daspect([1 12 1])
        mode(i-2) = getframe;
    end
    %movie(mode,6,24)
    %movie2avi(mode, ['Mode' num2str(modeNum) '.avi']);
end
%% MAC
clear all;
load 'model.mat';
modes_desired = 10;
model = model(:,1:modes_desired);
%model = [model(:,1) model(:,3) model(:,5) model(:,5) model(:,7)
model(:,8) model(:,9) model(:,9) model(:,10)];

m = zeros(24,modes_desired);
load 'measured.mat';

for ctr=1:9
    m(:,ctr) = measured(:,ctr) + m(:,ctr);
end
measured = m;
for row_ctr = 1 : size(measured,2)
    for col_ctr = 1 : size(measured,2)

        MAC(row_ctr,col_ctr) =
abs(model(:,row_ctr)'*measured(:,col_ctr))/...
        (norm(measured(:,col_ctr))*norm(model(:,row_ctr)));
    end
end

figure('Color',[1 1 1]);
bar3(MAC)
ylabel('Model')
```

```matlab
xlabel('Measured')
title('MAC of Theoretical vs. Experimental')

for row_ctr = 1 : size(measured,2)
    for col_ctr = 1 : size(measured,2)

        MAC(row_ctr,col_ctr) =
abs(measured(:,row_ctr)'*measured(:,col_ctr))/...
        (norm(measured(:,col_ctr))*norm(measured(:,row_ctr)));
    end
end

figure('Color',[1 1 1]);
bar3(MAC)
ylabel('Measured')
xlabel('Measured')
title('MAC of Experimental vs. Experimental')

for row_ctr = 1 : size(measured,2)
    for col_ctr = 1 : size(measured,2)

        MAC(row_ctr,col_ctr) =
abs(model(:,row_ctr)'*model(:,col_ctr))/...
        (norm(model(:,col_ctr))*norm(model(:,row_ctr)));
    end
end

figure('Color',[1 1 1]);
bar3(MAC)
ylabel('Model')
xlabel('Model')
title('MAC of Theoretical vs. Theoretical')

T = linspace(1,modes_desired,modes_desired);
[C,I] = max(MAC);
disp('Best Mode fits between measured and model')
disp('  Measured  Model')
disp([T'         I'])
```

Bibliography

Banik, J. A. (2007). Synchronous Deployed Solar Sail Subsystem Design Concept. *48th AIAA/ASME/ASCE/AHS/ASCStructures, Structural Dynamics, and Materials Conference.* Honolulu, Hawaii: AIAA.

Banik, J. (2008, Jan 10). Baseline TRAC boom Design SRS/NASA NanoSail-D. Albuquerque, NM: Air Force Research Lab.

Bleier, T., Clarke, P., Cutler, J., DeMartini, L., Dunson, C., Flagg, S., et al. (2004). QuakeSat Lessons Learned: Notes from the Development of a Triple CubeSat.

Boeing Completes CubeSat Mission to Advance Nano-Satellite Technology. (2007, August 17). Retrieved December 15, 2009, from Space Daily: http://www.spacedaily.com/reports/Boeing_Completes_CubeSat_Mission_To_Advance_ Nano_Satellite_Technology_999.html

Caday-Eames, E. (2006, October). Small box, big potential. *Boeing Frontiers* , p. 20.

Chin, A., Coelho, R., Brooks, L., Nugent, R., & Suari, J. (2008). Standardization Promotes Flexibility: A Review of CubeSats' Success. *AIAA/6th Responsive Space Conference* . Los Angeles, CA.

Cobb, R. G. (Fall 2009). Mechanics of Vibrations Course Notes . Air Force Institute of Technology, WPAFB, OH.

Cook, R., Malkus, D., Plesha, M., & Witt, R. (2002). *Concepts and Applications of Finite Element Analysis, 4th Edition.* Hoboken, NJ: John Wiley & Sons Inc.

Flagg, S., Bleier, T., Dunson, C., Doering, J., Louis, D., Clarke, P., et al. (2004). Using NanoSats as a Proof of Concept for Space Science Missions: QuakeSat as an Operational Example. *18th Annual AIAA/USU Conference on Small Satellites.*

Friedman, L. (2009, November 30). *Projects: LightSail- The Future of Solar Sailing.* Retrieved December 15, 2009, from The Planetary Society: http://www.planetary.org/programs/projects/solar_sailing/tpr_lightsail.html

Groom, R. S., & Hinkley, D. A. (2007). Potential Uses of CubeSat Technology and Standards in DoD Applications: Part I, Community Survey. Albuquerque, NM.

Harold, P. (2005, December 2). *BBC News.* Retrieved December 14, 2009, from UK stargazers enjoy a 'Lucky' break: http://news.bbc.co.uk/2/hi/science/nature/4456988.stm

Heidt, H. P., Puig-Suari, J., Moore, A. S., Nakasuka, S., & Twiggs, R. J. (August 2001). CubeSat: A New Generation of Picosatellite for Education and Industry Low-Cost Space Experiemntation. *Utah State University Small Satellite Conference*, (pp. 1-2,6). Logan, UT.

Lan, W. (2007). Poly Picosatellite Orbital Deployer Mk III ICD. *The CubeSat Program* . San Luis Obispo, CA : California Polytechnic State University.

Mierovitch, L. (2001). *Fundamentals of Vibration.* New York, NY: McGraw-Hill Book Co.

Mobrem, M., & Adams, D. S. (2006). Analysis of the Lenticular Jointed MARSIS Antenna Deployment. *47th AIAA/ASME/ASCE/AHS/ASC Structures, Structural Dynamics, and Materials Conference.* Newport, RI: AIAA.

Moore, G. E. (1965). Cramming more components onto integrated circuits . *Electronics Magazine* , p. 4.

Munakata, R., Lan, W., Toorian, A., Hutputanasin, A., & Lee, S. (2008). CubeSat Design Specification (Rev. 11). CalPoly SLO.

NASA Engineering Design Challenge. (n.d.). Retrieved December 28, 2009, from www.NASA.gov: http://www.nasa.gov/audience/foreducators/plantgrowth/reference/Eng_Design_5-12.html

NASA to Attempt Solar Sail Deployment. (2008, June 26). Retrieved December 15, 2009, from www.NASA.gov: http://science.nasa.gov/headlines/y2008/26jun_nanosaild.htm

Nugent, R., Munakata, R., Chin, A., Coelho, R., & Puig-Suari, J. (2008). The CubeSat: The Picosatellite Standard for Education and Research. *AIAA SPACE 2008 Conference & Exposition.* San Diego, CA: AIAA Inc.

Pellegrino, S. (n.d.). Deployable Membrane Reflectors. Cambridge, U.K.: University of Cambridge.

Pellegrino, S. (1994). Large retractable Appendages in Spacecraft. *Journal of Spacecraft and Rockets* .

Polytec. (2007). User Manual: Vibrometer Single Point Sensor Head OFV-505/-503.

Rees, W. (2001). *Principles in Remote Sensing.* University Press, Cambridge.

Rimrott, F. J. (September 1966). Stroable Tubular Extendible Members. *Engineering Digest* .

Roybal, F. A., Banik, J. A., & Murphey, T. W. (2007). Development of an Elastically Deployable Boom for Tesioned Planar Structures. *AIAA-2007-1838* .

Seffen, K. A., & Pellegrino, S. (1999). Deployment Dynamics of Tape Springs. *The Royal Society* .

Swartout, M. A. (May 2009). Student-Built Gossamer Spacecraft: Why Aren't There More (Yet)? *50th AIAA/ASME/ASCE/AHS/ASC Structures, Structural Dynamics, and Materials Conference.* Palm Springs, CA.

Swenson, P. (2010, March). Development and Design of an AFIT CubeSat Demonstrating Deployable Technology. *Master's Thesis* . Dayton , OH: Air Force Institute of Technology.

Vandawaker, R. M., Palazotto, A. N., & Cobb, R. G. (April 2007). Damage Detection through Analysis of Modes in a Partially Constrained Plate. *Journal of Aerospace Engineering* , 90-96.

Villaneuva, R. (2007, April). *Boeing Pico-Satellite Mission to Advance Miniature Satellite Technology.* Retrieved from Boeing Pico-Satellite Mission to Advance Miniature Satellite Technology: http://www.globalsecurity.org/space/library/news/2007/space-070419-boeing01.htm

Whorton, M., Heaton, A., Pinson, R., Laue, G., & Adams, C. L. (2008). NanoSail-D: The First Flight Demonstration of Solar Sails for Nanosatellites. *22nd Annual AIAA/USU Conference on Small Satellites.* Logan, UT: AIAA.

 You, Z., & Pellegrino, S. (1994). Dynamic Deployment of the CRTS Reflector. UK: AIAA.

REPORT DOCUMENTATION PAGE

Form Approved
OMB No. 0704–0188

1. REPORT DATE (DD–MM–YYYY) 25-03-2010	2. REPORT TYPE Master's Thesis	3. DATES COVERED (From — To) SEP09 – MAR10

4. TITLE AND SUBTITLE

Prototype Development and Dynamic Characterization of Deployable CubeSat Booms

5a. CONTRACT NUMBER

5b. GRANT NUMBER

5c. PROGRAM ELEMENT NUMBER

6. AUTHOR(S)

Thomas, Grant M.

5d. PROJECT NUMBER

5e. TASK NUMBER

5f. WORK UNIT NUMBER

7. PERFORMING ORGANIZATION NAME(S) AND ADDRESS(ES)
Air Force Institute of Technology
Graduate School of Engineering and Management (AFIT/ENY)
2950 Hobson Way
WPAFB OH 45433-7765

8. PERFORMING ORGANIZATION REPORT NUMBER

AFIT/GA/ENY/10-M10

9. SPONSORING / MONITORING AGENCY NAME(S) AND ADDRESS(ES)

Intentionally Left Blank

10. SPONSOR/MONITOR'S ACRONYM(S)

11. SPONSOR/MONITOR'S REPORT NUMBER(S)

12. DISTRIBUTION / AVAILABILITY STATEMENT
APPROVED FOR PUBLIC RELEASE; DISTRIBUTION UNLIMITED

13. SUPPLEMENTARY NOTES

14. ABSTRACT

The current barrier to CubeSat proliferation is their lack of utility depth. These small satellites are exceptionally well suited for specific space missions such as space weather observation and other scientific data gathering exploits, however, they are not suited for every mission. The 10cm-cube form factor that gives the CubeSat its unique advantage is also its greatest hindrance. A potential bridge over this gap is the successful integration of deployable booms onto the CubeSat structure. With this research, the Air Force Institute of Technology (AFIT) explored the parameters of deployable tapespring booms using the triangular retractable and collapsible (TRAC) cross-sectional geometry developed by Air Force Research Labs (AFRL) and used on NASA's CubeSat, Nanosail-D These booms were augmented with reflective membranes and specifically designed to deploy on orbit for the purpose of ground observation, observations that could later be used to determine the deployed dynamics of the booms from optical data gained passively by solar illumination.

15. SUBJECT TERMS
CubeSat deployable structures and flexible membranes in satellite applications

16. SECURITY CLASSIFICATION OF:			17. LIMITATION OF ABSTRACT	18. NUMBER OF PAGES	19a. NAME OF RESPONSIBLE PERSON Black, Jonathan T.
a. REPORT U	b. ABSTRACT U	c. THIS PAGE U	UU	176	19b. TELEPHONE NUMBER (Include Area Code) (937)255-3636, ext 4578 Email: jonathan.black@afit.edu

Standard Form 298 (Rev. 8–98)
Prescribed by ANSI Std. Z39.18